Abdelhamid Abdelrehim Mahmoud Elshaer

Molecular Beam Epitaxy Growth and Characterization of ZnO-based layers and Heterostructures

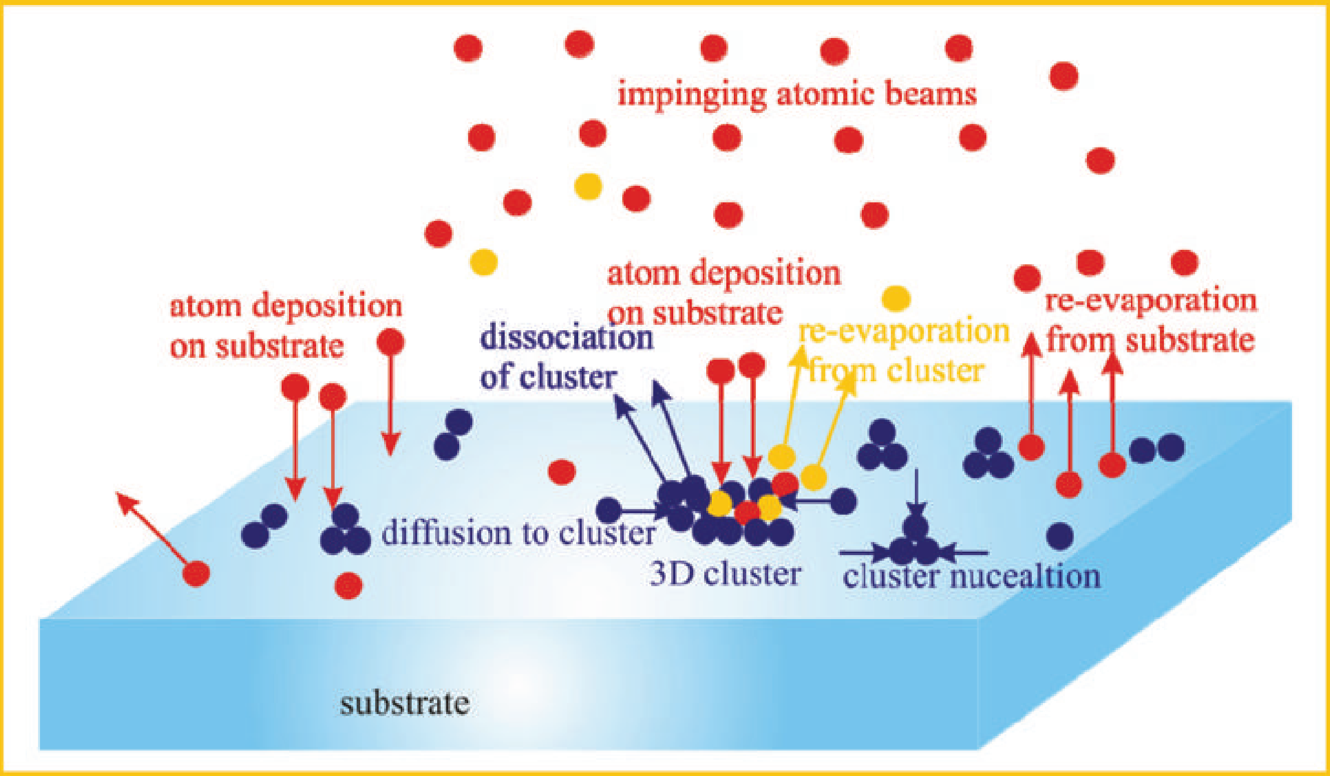

Cuvillier Verlag Göttingen

Molecular Beam Epitaxy Growth and Characterization of ZnO-based layers and Heterostructures

Von der Fakultät für Elektrotechnik, Informationstechnik, Physik
Universität Carolo-Wilhelmina zu Braunschweig
zur Erlangung der Würde eines
Doktor-Ingenieurs (Dr.-Ing)
genehmigte Dissertation

von: Abdelhamid Abdelrehim Mahmoud Elshaer, M.Sc.

aus (Geburtsort): Gharpiya

eingereicht am: 23.06.2008
mündliche Prüfung am: 10.07.2008

Referenten: Prof. Dr. rer. nat. habil. Andreas Waag
Prof. Dr.-Ing. habil. Wolfgang Kowalsky

2008

Bibliografische Information der Deutschen Nationalbibliothek
Die Deutsche Nationalbibliothek verzeichnet diese Publikation in der Deutschen Nationalbibliografie; detaillierte bibliografische Daten sind im Internet über http://dnb.ddb.de abrufbar.
1. Aufl. - Göttingen : Cuvillier, 2008
Zugl.: (TU) Braunschweig, Univ., Diss., 2008

978-3-86727-701-3

Nonnenstieg 8, 37075 Göttingen
Telefon: 0551-54724-0
Telefax: 0551-54724-21
www.cuvillier.de

1. Auflage, 2008
Gedruckt auf säurefreiem Papier

978-3-86727-701-3

Dedicated to

My wife and daughters

Table of contents

Introduction

Group IV elements like Si and Ge are well established semiconductor materials, but none of them is suitable for optoelectonic applications since they all have an indirect band gap, which does not lead to efficient light emission. Direct wide band gap semiconductors are needed for optoelectronic devices. Such semiconductors are formed mostly from III-V or II-VI compounds. In the last few years, most material developments on wide band gap semiconductors have focused on GaN, ZnSe, and SiC. SiC is an indirect band gap semiconductor. ZnSe based LEDs and laser diodes have a short lifetime due to the formation of defect clusters in the active region. GaN technology is very mature, and high quality devices can be fabricated. However, research on GaN has met many difficulties, for example, in developing high quality films and heterostructures by epitaxial growth. One reason for this is the absence of single crystal GaN wafer for homoepitaxy or small lattice mismatched substrate for heteroepitaxy. Another reason is that high quality films can only be obtained at high growth temperatures, which make GaN more expinsive. II-VI materials, on the other hand, have some interesting properties that do not only enable them to substitute or compliment GaN in several applications, but to also facilitate other applications, for which GaN is not suitable. Due to the large effective mass of electrons in the conduction band and holes in the valence band, as well as the small dielectric coefficient, the excitons in II-VI materials are generally much more stable than their neighboring III-V semiconductors. Therefore, they are more prospective candidate materials in the research on special excitonic properties for both scientific understanding and applications.

Recently, another wide band gap II-VI semiconductor, ZnO has reentered the scientific spotlight, this time as a prospective candidate for optoelectronic and photonic applications at short wavelength. ZnO is a transparent direct band gap (Eg = 3.37 eV) material with the wurtzite lattice structure. It has attracted much attention in recent years due to its fascinating properties which were discovered in 1970s, but cannot be employed at that time for opts-electronics due to luck of the suitable epitaxial technology. ZnO is often compared to GaN because of their nearly the same band gap needed for ultra-violet or blue light emission. Besides this major similarity, ZnO has a number of advantages that include extremely stable excitons. From the viewpoint of productive application, ZnO holds a few superiorities compared with GaN. Unlike GaN, ZnO can be grown in bulk and can be used as its own substrate. One of the main raw materials like: A few types of efficient, clean and low-cost oxygen sources are available for ZnO epitaxial growth, such as H_2O vapor, H_2O_2, ozone, alcohol and oxygen radical. The growth temperature for ZnO (typical 500°C) is much lower than that of GaN (usually 1000°C). A low growth temperature is advantageous to the fabrication of quantum structures (needed for efficient light emission) as it suppresses inter-diffusion at hetero-interfaces and non-uniform nucleation in alloy region. A low growth temperature also facilitates the incorporation of dopant and alloy constituents by suppressing the segregation effect. Since ZnO itself is a nontoxic material, no toxic materials are needed for its growth. In addition to these technological advantages, ZnO is highly radiation resistant making possible ZnO-based devices interesting for space applications. Due to its high melting point and large cohesive energy amongst the II-VI semiconductors, it is expected that a degradation of the material due to the generation of dislocations during device operation will be reduced. The most interesting property of ZnO is the large exciton binding energy of 60 meV, which is almost two times larger than either GaN or ZnSe. This is one of the key parameters that enable UV laser diodes and other exciton-related light emitting devices to be operated even above room temperature. By incorporating transition metals such as vanadium, manganese, cobalt in ZnO, a diluted magnetic semiconductor (DMS) could be obtained. Alloying ZnO films with MgO or CdO potentially permits the band gap to be controlled between 2.8 and 4 eV and even higher, which facilitates band gap engineering [1], while the lattice constant does not deviate much from that of ZnO, which smaller in-plane lattice mismatch than the (Al, Ga, In)N system in the same range of bandgap and lattice constant. The strong point of ZnO is, somehow, a combination of the good features of both GaN and ZnSe, which make ZnO an ideal candidate for a variety of devices including blue and ultra-violet laser diodes and light emitting diodes.

During the pereceding years, thin film growth techniques, such as sputtering and chemical vapor deposition, have been developed for ZnO growth. However, at that time, ZnO was thought to be used as a piezoelectric material, or transparent conductive material, for the applications to such as SAWDs, transparent electrode for solar cells, rather than a semiconductor. For these applications, the high crystal quality has never been a critical issue, so that, ZnO is still far from the stage for optoelectronic application. Molecular beam epitaxy (MBE) needs to be investigated as a reliable tool for the growth of highly crystalline ZnO. MBE has some substantial advantages over previous vacuum deposition techniques, such as hotwall epitaxy, which are the ultra-high vacuum (UHV) environment and significantly more precise control of the beam flux and growth conditions. In contrast to other epitaxial growth techniques, such as liquid phase epitaxy and vapor phase epitaxy, which proceed at nearly thermodynamic equilibrium conditions and are controlled by diffusion processes at the solid and liquid (gaseous) phase boundaries, in MBE, epitaxial growth is governed mainly by the kinetics of the surface processes occurring when impinging beams react with the outermost atomic layers of the substrate crystal. This is far from the thermodynamic equilibrium conditions, although a thermodynamic approach can be applied to MBE growth description. In comparison to all other epitaxial growth techniques, MBE has a unique advantage. Being realized in UHV environment, it may be analized and controlled in situ by surface diagnostic methods, such as reflection high-energy electron diffraction, Auger electron Spectroscopy. These powerful facilities for analysis and control eliminate much of the guesswork in MBE, and enable the fabrication of sophisticated device structures using this growth technique. These advantages make MBE a state-of-art epitaxial growth technique with excellent flexibility.

The aim of this work is thus to develop an epitaxial growth technique, which should be able to fabricate device-quality ZnO thin films. Nitrogen-doped ZnO will investigate. The ZnMgO based quantum structures with well controlled Mg content are also to be studied.Therefore, MBE as an epitaxial growth technique and a widely used low-cost sapphire substrate are chosen as the technical basis for this research. Furthermore, the possibility of device fabrication on the basis of ZnO and ZnO-based heterostructures is to be analyzed by fabricating and characterising device structures.

In this thesis, the research background and the fundamental material properties will be presented in chapter 1. In chapter 2, attention will be given to MBE growth facilities and the characterization methods involved in this work. Chapter 3 treats experimental processes of the growth of ZnO and ZnMgO epilayers on different substrates (GaN template, c-sapphire and ZnO), using different oxygen precursors (oxygen plasma and hydrogen peroxide), and the subsequent structural, optical and electrical characterisation of the obtained layers. P-type doping and devices based on ZnO will be a subject of chapter 4. ZnO-based Heterostructures for Opto- & Magneto-electronics will be considered in chapter 5. Finally, conclusions and critical analysis of the obtained results are presented in chapter 6.

1. ZnO: Material properties and epitaxy

Zinc oxide is an inorganic compound with formula ZnO formed from a Zn^{2+} cation and O^{2-} anion. Thus, it is often referred to as an II-VI compound, since Zn is a Group II element and oxygen is a Group VI element on the periodic table. Pure ZnO is colorless and crystallizes in the hexagonal wurtzite structure. In this chapter, attention will be given to the main material-specific properties of ZnO. Also an overview of thin films growth *kinetics,* and surface processes are presented.

1.1. Physical properties of ZnO

1.1.1. Crystal structure and lattice parameters of ZnO

Crystal structure: ZnO crystallizes in either cubic zinc-blende or hexagonal wurtzite structure where each anion is surrounded by four cations at the corners of a tetrahedron, and vice versa. This tetrahedral coordination is typical of sp^3 covalent bonding, but these materials also have a substantial ionic character. The ionicity of ZnO is at borderline between covalent and ionic semiconductor.

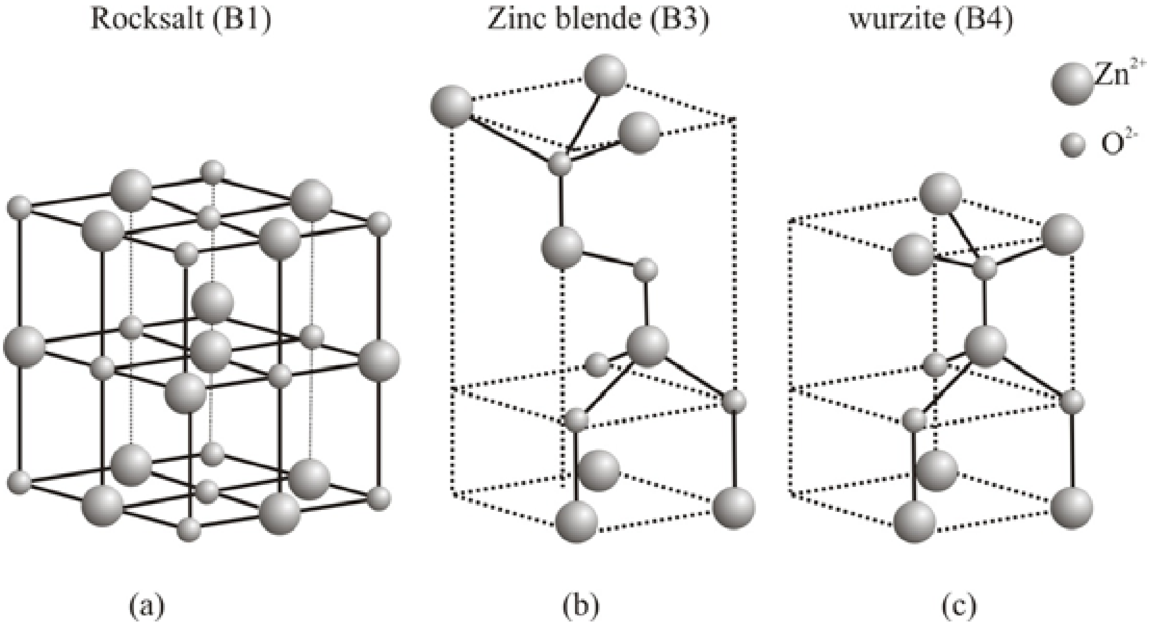

Figure 1.1: *possible of ZnO crystal structures:*
(a) cubic rocksalt (B1), (b) cubic zinc blende (B3), and (c) hexagonal wurtzite (B4).

The crystal structures shared by ZnO are wurtzite (B4), zincblende (B3), and rocksalt (B1) are schematically shown in Figure 1.1. At ambient conditions, the thermodynamically stable phase is wurtzite. The zincblende ZnO structure can be stabilized only by growth on cubic substrates, and the rocksalt (NaCl) structure may be obtained at relatively high pressures. Wurtzite structure is one of the most common crystal structures of semiconductors. Other semiconductors that crystallize in wurtzite include nitrides (GaN, AlN), II-VI semiconductors (ZnS, CdS, ZnSe, CdSe, ZnTe, CdTe), SiC, and InAs, etc. ZnO has a hexagonal close-packed (hcp) Bravais lattice as shown in Figure 1.2.

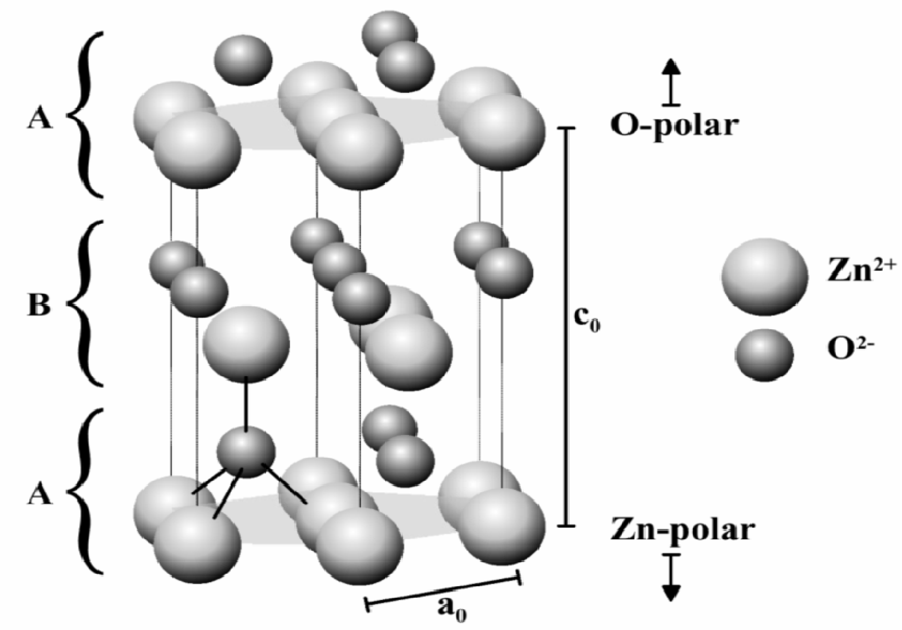

Figure 1.2: *The hexagonal wurtzite structure of ZnO crystal*

The structure of ZnO can be considered to be composed of two interpenetrating hcp sublattices of cation (Zn) and anion (O) displaced by the length of cation-anion bond in the c-direction. The number of the nearest neighbors in wurtzite is four. Each O (or Zn) ion is tetrahedrally surrounded by four Zn (or O) ions. Furthermore each ion also has twelve next-nearest neighbors of the same type of ions. The O-Zn distance of the nearest neighbors is 1.992 Å in the direction parallel to the c-axis of the hexagonal unit cell and 1.973 Å in the other three directions of the tetrahedral arrangement. The tetrahedral arrangement of the nearest neighbors indicates the covalent bond between the Zn and O atoms. The covalent radii of Zn and O were reported to be 1.31 Å and 0.66 Å, respectively. ZnO is an-isotropic crystal with the symmetry of point group of C6v (or 6mm). Group C6v is the point group of the hexagonal wurtzite structure, which includes rotations by ±60°, and ±120° around the hexagonal axis and two sets of three equivalent mirror planes that are parallel to the hexagonal axis.

Lattice parameters**:** Lattice parameters are important to consider when one develops semiconductor devices. Besides the intrinsic material properties, there are four main factors which in addition modify the lattice parameters of the semiconductor. The first factor is free-electron concentration acting via deformation potential of a conduction-band minimum occupied by these electrons. The second factor is the concentration of impurities and defects and the difference in ionic radii between these defects and impurities and the substituted matrix ions. The third factor is the external strain. The last factor is the temperature. The u parameter which describes the relative position of the anion sublattice with respect to the cation sublattice along the c axis in the wurtzite structure (Zn at $(1/3,\ 2/3,\ 0)$ and, $(2/3,\ 1/3, 1/2)$and O at$(1/3,\ 2/3,\ u)$, and$(2/3,\ 1/3, u+1/2)$) is related to the c/a by $uc/a=(3/8)^{1/2}$. It has been assumed that the u parameter is close to 3/8 for all compounds in the wurtzite structure. For ZnO Kisi and Elcombe have in fact shown experimentally that there is a strict correlation between u and c/a, i.e., uc/a is near the ideal value $(3/8)^{1/2}$. The lattice constants, c/a, and u parameter of wurtzite structure ZnO, shown in table 1-1 [1-5]. The deviation from the ideal wurtzite crystal is probably due to lattice stability and ionicity. The point defects such as zinc antisites, oxygen vacancies, and extended defects, such as threading dislocations, also increase the lattice constant in a ZnO crystal, albeit to a lesser extent in the heteroepitaxial layers. Strong correlation exists between the c/a and the u parameter, when c/a ratio decreases, u parameter increases in such a way that those four tetrahedral distances remain nearly constant through a distortion of tetrahedral angles due to long-range polar interactions.

Wurtzite ZnO crystal structure				
a (Å)	c (Å)	c/a	u	Ref.
3.2475	5.2075	1.6035	0.3796	[2]
3.2496	5.2042	1.6015	0.3800	[3]
3.2497	5.206	1.6020	0.3799	[4]
3.2501	5.2071	1.6021	0.3817	[5]
3.286	5.241	1.595	0.383	[6]

Table 1.1*: Measured and calculated lattice parameters, c/a ratio and u parameter, of wurtzite ZnO crystal structure.*

ZnO wurtzite structure has a different crystallographic index indication system from the conventional cubic semiconductors. Because in the case of wurtzite structure, if the Miller indices of three number based on axes *a1*, *a2*, *c* are used to define planes and directions in the structure, it is found that crystallographically equivalent sets can have combinations of different numbers. Hexagonal axes are four in number, viz. a vertical axis coinciding with the principal axis of the crystal, and three horizontal axes inclined to one another at 60° in a plane perpendicular to the principal axis, and hence no longer linearly independent. The indices of planes referred to such a set of axes are four in number; they are written as {hikl}, the first three ($h+i+k=o$) referring to the horizontal axes and the last to the vertical axis. Equivalent planes are obtained by interchanging the position and the sign of the first three indices. Direction indices in hexagonal structures are translations parallel to the four axes that cause the motion in the required direction. The number must be reduced to the smallest integers and chosen so that the third index is negative of the sum of the first two.

1.1.2. Native defects and doping in ZnO

In the applications of ZnO for electronic devices, the control of native defects is essential since the electrical properties are largely affected not only by extrinsic dopants but also by native defects. The formation energies and electronic structure of native point defects in ZnO were calculated by Van de Walle *et* [7],[8]. After neglecting the change in the volume when defects are introduced in the system and the change in the vibrational entropy, the relationship between the concentration of defects (C_D) in a crystal and their formation energies E_f , which determines the likelihood for a defect to form during growth is defined as:

$$C_D = N_{sites} \exp\left(-\frac{\Delta E^f}{K_B T} \right) \tag{1.1}$$

Here N_{sita} is the concentration of available sites in the crystal where the defect can occur per unit volume. K_B is the Boltzmann constant, and T the temperature. The formation energy of a native defect D in charge state q is defined as [9].

$$\Delta E^f (D^q) = E_{tot}(n_{Zn}, n_O) - E_{tot}(ZnO) + n_{Zn}\mu_{Zn} + n_O\mu_O + qE_f \tag{1.2}$$

Where, $E_{tot}(n_{Zn},n_O)$ is the total energy of the supercell containing the defect D in the charge state q containing n_{Zn} zinc and n_O oxygen atoms, and E_{tot}(ZnO) is the total energy of the ZnO perfect crystal in the same supercell. E_F is the Fermi energy. μ_{Zn} and μ_O are the chemical potentials of Zn and O, i.e., the energies of the reservoirs with which Zn and O atoms are exchanged.

The chemical potentials determine the stoichiometry of the system, and depend on different parameters such as partial pressures and growth conditions. ZnO can exist within a range of oxygen and zinc chemical potentials. The boundaries on μ_{Zn} and μ_O in ZnO are determined by the stability limits of ZnO with respect to zinc metallic and molecular oxygen. In zinc-rich case, $\mu_{Zn} = \mu_{Zn}^0$, while, $\mu_O = \mu_O^0$ for oxygen-rich case. Here μ_{Zn}^0 is the energy of Zn in the standard state (pure metal), and μ_O^0 is the energy of pure O_2 gas (per oxygen atom).

ZnO doping: P-type ZnO can be achieved by doping with either group-I elements (Li, Na, and K) or group-V elements (N, P, As, and Sb). Although substitutions by group I elements are shallow acceptors, calculations show that group I elements tend to form interstitials and actually behave as donors. Several reports on ZnO doping with Li, Na, K, [10], [11], [12], Cu and Ag [13] exist. On the other hand, it was observed that doping with group-I elements increases donor concentration instead. This is attributed to tendency of group-I dopants to occupy the interstitial sites, partly due to their small atomic radii. Additionally, doping with Na and K induces lattice strain due to the change of the bond length, which leads to the formation of the vacancies which compensate the dopants [14].

P and As are deep acceptors and calculations show that they can lead to formation stable acceptor centers, which convert acceptors into deep donors. Calculations also show that P and As are amphoteric [14], and that they have a tendency to form P_{Zn} and As_{Zn} antisites, which are also donors. Several papers on p-type ZnO doping by P [15], As [16], and Sb [17] were published, however the results were not reproducible. Among possible dopants, nitrogen appears to be a more promising choice than other impurities since it is a known p-type dopant for ZnSe. Acceptor concentrations as high as 10^{18}cm^{-3} were obtained in ZnSe samples grown with MBE using nitrogen atom beam doping[18].

1.1.3. Band structure and optical properties of ZnO

The band-structure of a material is very useful information in predicting the electrical properties when the material is doped. The electronic band structure of ZnO has been calculated by a number of groups [13];[19];[20];[21];[22]. The results of a band structure calculation using the Local Density Approximation (LDA) and incorporating atomic self-interaction corrected pseudo potentials (SIC-PP) to accurately account for the Zn 3*d* electrons is shown in Figure 1.3 [22]

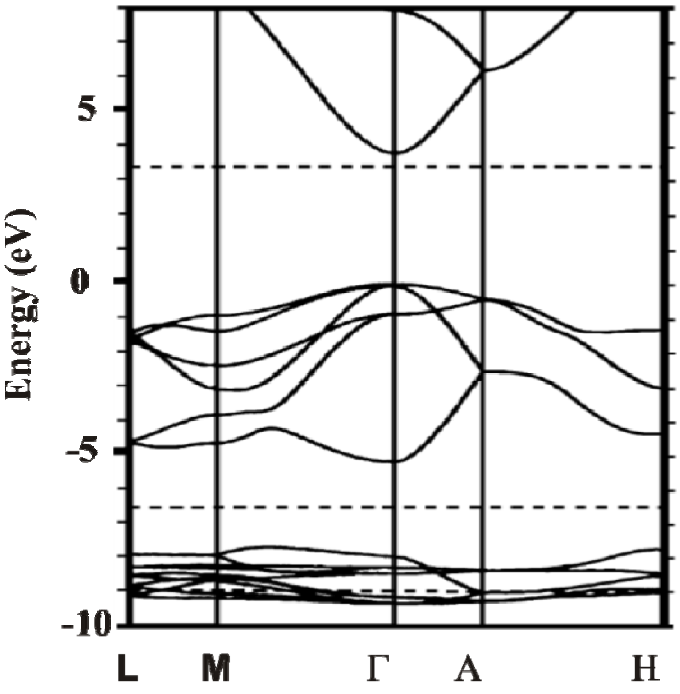

Figure 1.3: T*he LDA band structure of bulk wurtzite ZnO calculated usingdominant atomic self-interaction-correctedpseudopotentials (SIC-PP). ref.[22]*

The band structure is shown along high symmetry lines in the hexagonal Brillouin zone. The most important point to notice is that between the occupied bands and the empty bands there is an optical band gap, E_g, of approximately 3.3 eV. This is the energy difference between the full and empty electron states. These filled states are called the valence band, and the energy at the top of the valence band is conventionally the zero of energy and is called the valenceband edge. The empty states above the gap are called the conduction band. The lowest point in the conduction band is called the conduction band edge.

Both the valence band maxima and the lowest conduction band minima occur at the Γ point k=0 indicating that ZnO is a direct band gap semiconductor. The bottom 10 bands (occurring around -9 eV) correspond to Zn 3*d* levels. The next 6 bands from -5 eV to 0 eV correspond to O 2*p* bonding states. The first two conduction band states are strongly Zn localized and correspond to empty Zn 3*s* levels. The band gap as determined from this calculation is 3.77 eV. This correlates reasonably well with the experimental value of 3.4 eV. Experimentally, the ZnO valence band is split into three band states, A, B and C by spin-orbit and crystal-field splitting. This splitting is schematically illustrated in figure 1.4. The A and C sub-bands are known to possess Γ_7 symmetry, whilst the middle band, B, has Γ_9 symmetry [23].

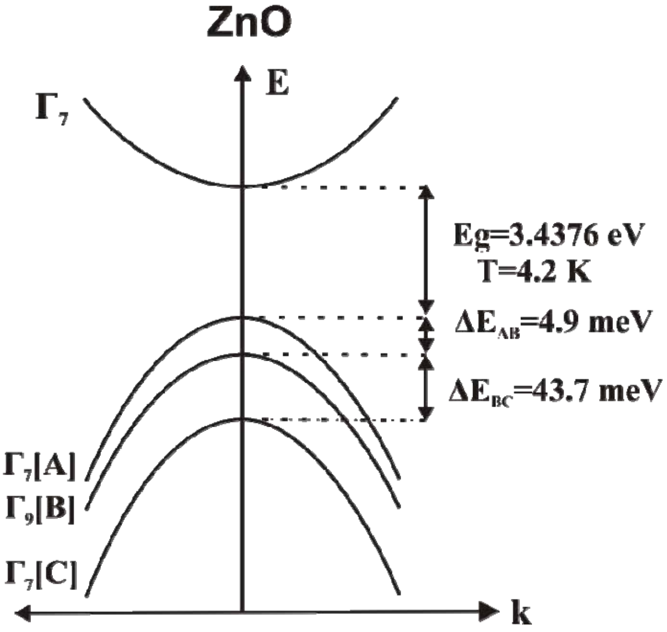

Figure 1.4: *Schematic diagram representing the crystal-field and spin-orbit splitting of the valence band of ZnO into 3 subband states A, B and C at 4.2 K. ref. [23]*

In terms of the more fundamental optical properties of ZnO, there have been a number of comprehensive studies to determine the refractive index and dielectric constants of this material [24];[25];[26]. The measurements were all carried out using spectroscopic ellipsometry. The values determined for the dielectric constants of ZnO are shown in table1.2. The refractive index at room temperature of wurtzite ZnO is commonly given as $n\perp c$ =2.115 and $n\parallel c$= 2.115 at wavelength 4605 Å [27].

ε_0		ε_∞		Ref.
E∥C	E⊥C	E∥C	E⊥C	
8.59	7.46	3.78	3.7	Film[25]
8.91	7.7	3.66	3.6	Bulk[25]
-	-	3.72	3.68	Bulk[24]

Table 1.2: *Static (ε_0) and high frequency dielectric constant (ε_∞) for ZnO*

1.1.4. Luminescence in ZnO

Luminescence refers to all types of light emission appearing as a consequence of some external excitation, except incandescent emission [28]. Depending on the different excitation sources, photoluminescence (PL), which requires optical excitation, electroluminescence (EL), with electric field as excitation source, cathodoluminescence (CL), which results from electron-beam excitation etc. Luminescence (or photon emission) of semiconductors is the direct results of electron transition from upper energy levels to lower energy levels. If the excitation energy is larger than the band gap of the semiconductor, the generated electrons and holes are in excited states. Then, they rapidly lose energy to the lowest level of the lowest excited state in order to gain thermal equilibrium (thermalisation). This process is called relaxation, and many different possible transitions in PL spectrum observed (Figure 1.5):

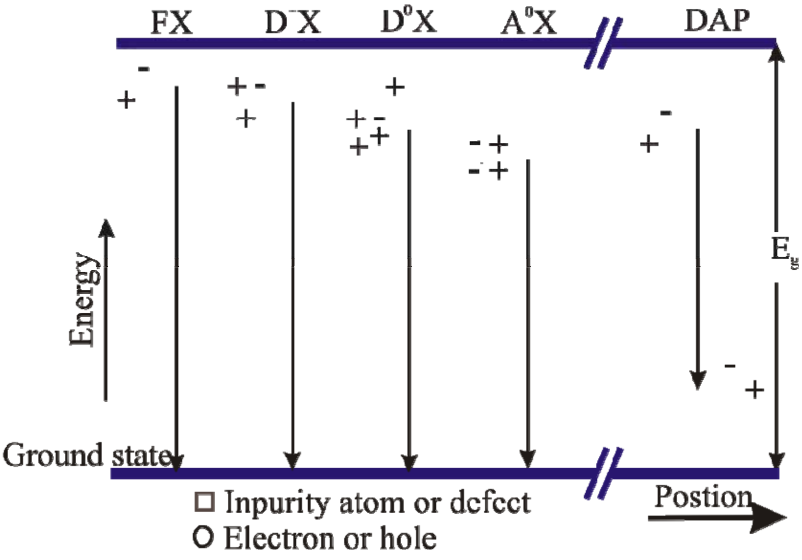

Figure 1.5: *Main radiative recombinations from semiconductor materials in photoluminescence spectroscopy*

Free excitons recombination: The conduction band of ZnO with wurtzite crystal structure is constructed from s-like state (Γ_7^c), which has a symmetric shape. The valance band is a p-like state. It is split into three bands because of crystal field and spin-orbit interaction [29], which dominates the near bandgap intrinsic absorption and emission spectra. The related free-exciton transitions involiving an electron from the conduction band and a hole from these three valance bands are named as A (corresponding to the heavy hole), B (corresponding to the light hole), and C (corresponding to crystal field split band).

Free-carrier recombination (band-to-band recombination): free carrier radiative recombination usually occurs at energies larger than or equal to the bandgap of the semiconductor (can also be at E<Eg, due to band gap renormalization). In a direct band gap semiconductor without defects, there is a high possibility that electrons and holes will directly recombine after the thermalisation process to emit a photon of energy close to the band gap of the material, with its maximum at:

$$\hbar\omega_{bb} = E_g + \frac{K_B T}{2} \tag{1.3}$$

where k_B is the Boltzmann constant and T the absolute temperature. The band-to-band emission line is additionally broadened partly due to thermal distribution of the charge carriers. Excitons that lead to band-to-band transitions are referred to as free-excitons (F_X)

Bound-exciton recombination: This is a radiative recombination of electron (hole) with a hole (electron) bound to an acceptor (donor). Such emission lines appear on PL spectra with their maximum at:

$$\hbar\omega_{\mathrm{be}} = \mathrm{E_g} - \mathrm{E^b_{A/D}} + \frac{\mathrm{K_B T}}{2} \tag{1.4}$$

where $E^b_{A/D}$ is the ionisation energy of the impurity to which the exciton is bound. Neutral donor-bound exciton transitions are denoted D^0X, while neutral acceptor-bound excition transitions are denoted A^0X. Ionised donor- and acceptor-bound transitions are denoted D^+X and A^+X respectively.

Two-electron satellites in PL: Two electron satellite(TES) transition process in high quality ZnO occurs can be observed in low temperature PL spectra in the photon energy, range from 3.30 to 3.34 eV. This transition process is generated by the radiative recombination of an exciton bound to a neutral donor, leaving the donor in the excited state. The energy position of the excited state of shallow donor can be roughly estimated from the energy distance between the the ground-state neutral-donor bound excitons and TES lines. Then the donor binding energy can be calculated because the excited-to-ground levels distance equals to 3/4 of the donor binding energy E_D.

Shallow donor-acceptor pair transition: At thermal equilibrium, some electrons are captured by acceptors, thus creating ionised donors (D^+) and acceptors (A^-), which exert coulomb interactions on each other constituting the energy $E_{Coul} = \frac{e^2}{4\pi\varepsilon_r d_{DA}}$. Here, ε_r, d_{AD} are the relative permittivity of the material and the donor-acceptor separation, respectively. e is the electronic charge. During PL or CL measurements, excited electrons and holes in the semiconductor material are captured by D^+ and A^- forming unstable neutral donors and acceptors. While returning to equilibrium state, the electrons in the unstable donors recombine with the holes in the unstable acceptors resulting in light emission. This recombination is denoted DAP and the resulting emission has its maximum at

$$\hbar\omega_{\mathrm{dap}} = \mathrm{E_g} - \mathrm{E_A^b} - \mathrm{E_D^b} + \mathrm{E_{Coul}} \qquad (1.5)$$

The donor and acceptor impurities are ionised again after recombination. They assume lower states since the Coulomb interaction dominates between them.

In case of partly ionic bonding like in ZnO, the crystal lattice is polarised by charge carriers leading to lattice distortion, which is described by a superposition of longitudinal optical (L_O) phonons. These couple very strongly with photons, causing the emission of L_O-phonons (commonly called phonon replica) accompanying main transitions. The energy distance between the phonon replicas equals the phonon energy. In ZnO, it is 72 meV [30].

1.1.5. Band gap engineering in ZnO

For a semiconductor to be useful, particularly in reference to optoelectronic devices, band gap engineering is an important step in device development. By alloying the starting semiconductor with another material of different band gap, the band gap of the resultant alloy material can be fine tuned, thus affecting the wavelength of exciton emissions. Alloying ZnO with CdO [24]-[34] and MgO [35]-[41]have allowed the generation of red- or blue-shifts of the emission wavelength, respectively. In the alloy system ZnxMg1-xO, the emission wavelength can be precisely tuned by changing the Mg composition [36], [42] or by inducing thermal intermixing in the ZnMgO superlattice by annealing [43],[44]. These techniques result in a uniform wavelength shift throughout the whole material. Figure 1.6 shows the relationship between the in-plane lattice constant and the band gap energy for the family of wide band-gap semiconductors. As the solid line shows, band gap engineering in ZnO can be done within a brouder energy range with reduced lattice misfit than in GaN.

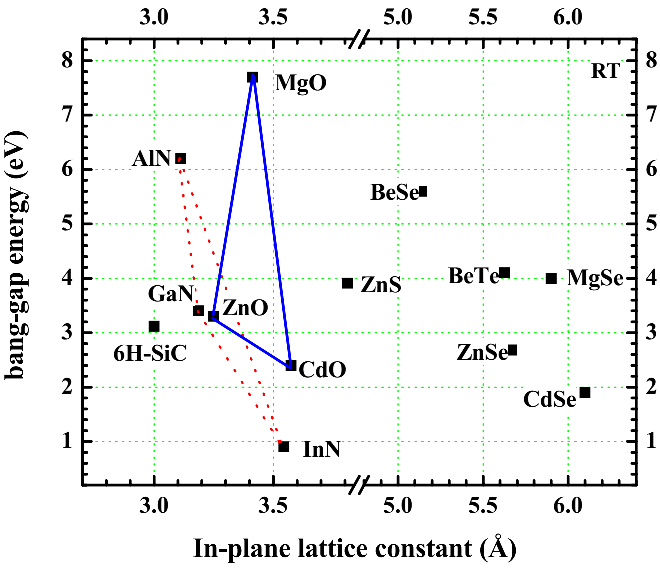

Figure 1.6: *Wide band gap semiconductors; possibilities for band-gap engineering*

However, the hexagonal wurtzite structure of ZnO can be maintained only up to certain Mg content, beyond which a change of phase occurs from wurtzite to rocksalt. There are controversial reports about the limit of Mg content in ZnMgO, within which the wurtzite structure is maintained. The maximum reported value for Mg content so far is 33% [45].

1.1.6. Ferromagnetism in ZnO

The use of carrier spin, in addition to charge, appears promising for another class of devices, such as polarized light emitters, chips that integrate memory and microprocessor functions, magnetic devices exhibiting gain, and ultra low-power transistors [46]-[51]. Most of the initial work in dilute magnetic materials focused on II-VI semiconductors in which a fraction of the group-II sublattice was randomly replaced by Mn atoms [46]. In these materials, the presence of magnetic ions influences the free carrier behavior through the sp-d exchange interaction between the localized magnetic moments and the spins of the itinerant carriers. The control afforded by modern growth techniques, such as molecular-beam epitaxy, also led to the realization of the GaMnAs alloy with Mn contents well in excess of the miscibility limit of Mn. A major breakthrough in the field came with the theoretical prediction of magnetic ordering temperatures in excess of room temperature for at 5 % Mn doping in ZnO [48]. For spintronics, theoretical predictions suggest that room-temperature carrier mediated ferromagnetism should be possible in ZnO, albeit for p-type material. Unfortunately, the realization of p-type ZnO has proven difficult until recently. Ab initio calculations do predict ferromagnetism in n-type ZnO doped with most transition metal ions, including Co and Cr, but predict no ferromagnetism for Mn-doped ZnO [52]. This is consistent with experimental results where ferromagnetism is not observed in Mn-doped in n-type ZnO [53].

1.1.7. Other properties of ZnO

Electrical properties: The electrical properties of ZnO are hard to quantify due to large variance of the quality of samples available. The background carrier concentration varies a lot according to the quality of the layers but is usually within the range 10^{15}-10^{17} cm^{-3}. The largest reported *n*-type doping is ~10^{20} electrons cm^{-3} and largest reported *p*-type doping is ~10^{19} holes cm^{-3}, however such high levels of *p*-conductivity are questionable [54]. The electron effective mass is 0.24 m_0, and the hole effective mass is 0.59 m_0. The corresponding electron Hall mobility at 300K for low *n*-type conductivity is μ = 200 $cm^2V^{-1}s^{-1}$, and for low *p*-type conductivity is 5-50 $cm^2V^{-1}s^{-1}$ [27].

Mechanical properties of ZnO: ZnO is a relatively soft material, with a hardness of ~ 5 GPa at a plastic penetration depth of 300 nm (for c-axis oriented bulk ZnO) [55]. This needs to be taken into consideration when processing and designing ZnO based devices. For loads of up to 50 mN, there has been no observation of phase transformations or cracking in this material. ZnO is believed to have a piezoelectric tensor equal to or even greater than that of GaN and AlN, which means that ZnO is a suitable candidate for device applications requiring a large electromechanical coupling [56]. Many studies, both theoretical and experimental, have been made to determine the three piezoelectric stress coefficients for wurtzite ZnO [57]-[59].

Thermal property of ZnO: The thermal expansion coefficients (TEC), which are defined as the ratio $\Delta a/a$ and $\Delta c/c$, are used to describe the quantitatively temperature dependence of lattice parameters ***a*** and c. The stoichiometry, extended defects and free-carry concentration also affect the TEC. The X-ray power diffraction method by Reeber [59] was used to measure the temperature dependence of the lattice parameters of ZnO.

1.1.8. Applications of ZnO

In this section, a brief overview of the projected applications for ZnO is provided. Existing technologies are also being revolutionised with ZnO nanoparticles, which have led to the development of improved sunscreens, paints and coatings, plastic and rubber manufacturing, electronics and pharmaceuticals. With improvements in growth technology of ZnO nanostructures, epitaxial layers, single crystals and nanoparticles, we are now moving into an era where ZnO devices will become increasingly functional and extraordinary. ZnO-based nanostructures including nanowire arrays hold a host of opportunities for flat screen displays, field emission sources, gas, chemical [38] and biological sensors, and as UV light emitters, detectors and switches [61]-[64]. Epitaxial layers and single crystals will be important for the development of optoelectronic (blue and ultraviolet light emitters and detectors) [54], piezoelectric [65] and spintronic devices [66]. Such devices also have applications within military applictions, ultra high density data storage, blue, UV and white light LED's and laser diodes, secure communications and biodetection. Epitaxial ZnO also holds much promise as a semiconducting transparent thin film [67], which again will be important for solar cells, gas sensors, UV detectors, displays and wavelength selective applications. Additionally, the radiation hardness of ZnO to MeV proton irradiation makes it an ideal candidate for space applications [68]. Thus ZnO whilst already possessing a wide application base, has enormous opportunities for society and industry alike due to its unique properties which are now being explored and applied.

1.2. Basic physical processes in MBE

Understanding kinetics, thermodynamics and how they interact and compete with each other would enable us to know how to control the growth of thin films, which is of great importance to all modern semiconductor technologies as well as to the basic science. In MBE, growth process may be divided into three zones where different physical phenomena take place [69] (see Figure 2.1). The first zone is the generation zone of the molecular beam under UHV conditions from sources, of the effusion-cells, whose temperatures are accurately controlled. The uniformity in thickness as well as in the composition of the films grown by MBE depends on the uniformities of the molecular beams fluxes and also on the geometrical relationship between the configurations of the sources and the substrate. Next is the zone where, the beams from different sources intersect each other and the vaporized element mix together creating a very special gas phase contacting the substrate area. This area, where the crystallization processes take place, can be regarded as the third zone of the MBE physical system. Epitaxial growth in MBE is realized in the third zone (on the substrate surface). A series of surface processes takes place during the growth which is schematically summarized in Figure1.7. Thin film deposition is a dynamic process.

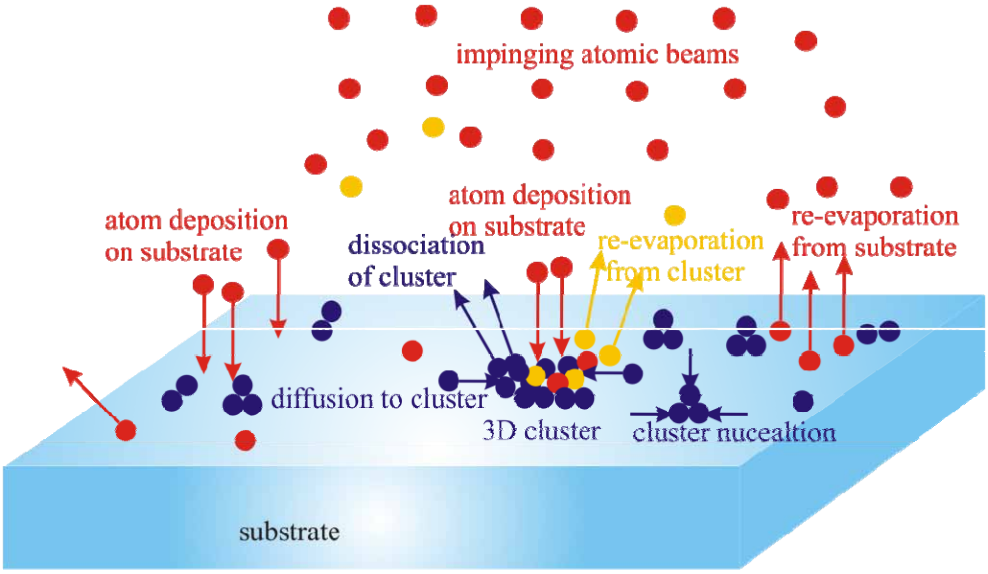

Figure 1.7: *Basic atomic processes during thin film growth.*

The surface processes occurring during MBE growth are characterized by a set of relevant kinetic parameters that describe them quantitatively. The arrival rate is described by the flux of the arriving species and gives the number of atoms impinging on the unit area of the surface per second. Evaporated atoms with temperature T_i impinge onto the substrate surface, which has a temperature T_s, usually lower than T_i at different positions with different kinetic energies. Depending on the atom's energy and the position at which it hits the substrate surface, the impinging atom could reevaporate immediately, carrying with it an energy corresponding to temperature T_e or exchange energy with the atoms of the substrate until they are in thermodynamic equilibrium at T_s. description of this process is possible by defining the thermal accommodation coefficient as:

$$\alpha = \frac{T_i - T_e}{T_i - T_s} \qquad (1.6)$$

When T_e is equal to T_s the accommodation coefficient is unity. Thus, it emerges as a measure of the extent to which the arriving atoms reach thermal equilibrium with the substrate [71]. It is important to differentiate between the accommodation coefficient (α) and the sticking coefficient (S_c). the sticking coefficient is defined as the ratio of the number of atoms adsorb, or "stick", to the substrate surface to the total number of atoms that impinge upon the substrate surface during the same period of time.

$$S_c = \frac{N_{ads}}{N_{tot}} \qquad (1.7)$$

In many cases, S_c is less than unity and it may be a small fraction in cases when the adsorption energy of atoms on the substrate is low, or the substrate temperature is high. S_c is inversely proportional to the exponential of the temperature and also inversely proportional to the square of the distance between atomic steps on the surface of a crystalline material [72]. Assuming that $\alpha=1$, all the arriving atoms are accommodated on the substrate surface and achieve thermodynamic equilibrium. They still have a finite probability related to the substrate temperature of acquiring sufficient energy to overcome the attractive forces and leave the substrate. If aggregation of adatoms, does not occur, all adatoms will eventually be reevaporated. Thus, the S_c can be almost zero even when α is unity.

Adsorption occurs by either forming a van der Waal's bond with a surface atom "physisorption", or by forming a covalent or ionic bond with surface atom "chemisorption". The rate at which adatoms are adsorbed to the surface is roughly proportional to $\nu_a \exp[-\frac{E_a}{kT}]$, where ν_a is the adsorption frequency, E_a is the adsorption energy, k is Boltzmann constant and T is the substrate temperature. However, most substrate surfaces have complicated reconstructions and the bonding is highly directional. Therefore, the probability of adsorption to some sites is higher than others.

Assuming defect-free surfaces, a number of theoretical and experimental works has been carried out to find out the most stable adsorption sites. Adsorbed atoms may diffuse from one site to another via thermally activated hopping, with the diffusion coefficient

$$D \propto a^2 k_s \propto a^2 exp\,[-\frac{E_d}{kT}] \qquad (1.8)$$

Where; k_s is the site-to-site hoping rate, a, is the effective hopping distance between sites, E_d is the diffusion energy and T is the substrate temperature. Because of the complicated nature of most surfaces, diffusion is an anistropic and complicated process. It should be pointed out that diffusion is the process responsible for the degree of smoothness of the grown film for a fixed deposition rate. Diffusing adatoms meet and bond with each other forming clusters that differ in size, depending on the deposit vapor pressure or the deposition rate. Nucleation on smooth surfaces is not energetically favored and requires the number of adatoms to be much larger than that at equilibrium. In fact, flat surfaces with no defects do not exist in nature. Defects, e.g., dislocations, kinks, vacancies and ledges (see Figure 1.8), act as favored nucleation sites that enhance nucleation [73].

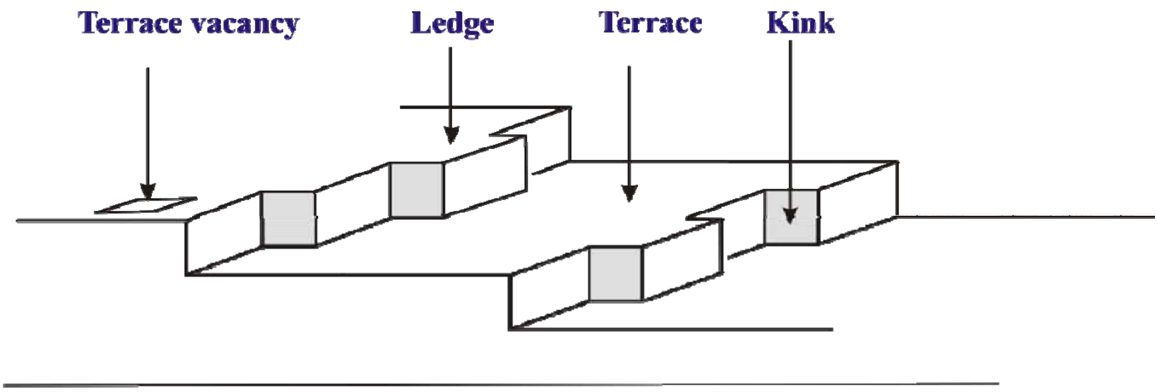

Figure 1.8: *Surface defects are favored nucleation centers.*

Due to the large surface-to-volume ratio, small clusters (smaller than the so-called critical size) are energetically unstable, and the probability of their dissociation is quite high. Balance between the growth and the dissociation of a given cluster depends on its total free energy and the adatom vapor pressure.

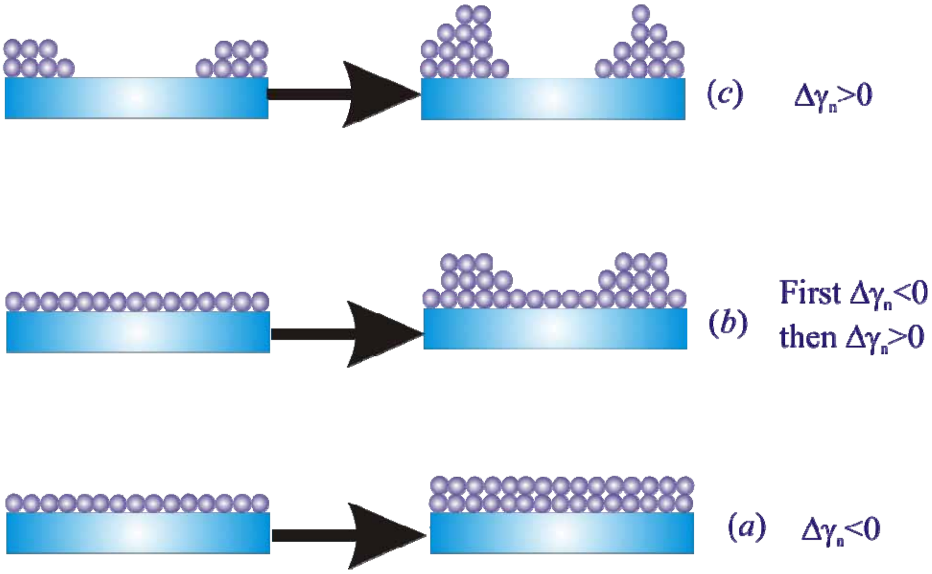

Figure 1.9: *Basic nucleation modes: (a) Frank - van der Merwe, (b) Volmer –Weber, and (c) Stranski-Krastanov.*

The relation between the film surface energy γ_F, the substrate surface energy γ_S, and the interface energy between film and substrate γ_{FS}, the film grows in one of three growth modes (see Figure 1.9):

$$\Delta\gamma_n = \gamma_F + \gamma_S - \gamma_{FS} \quad ,where\ ,n\ refers\ to\ \ n^{th}\ layer\ growth$$

a) Frank-van der Merwe (layer-by-layer): takes place when the deposit atoms are more strongly attracted to the substrate than they are to themselves (i.e. $\Delta\gamma_n < 0$).
b) Stranski-Krastanov (layer-plus-island): in this mode, the most common one, layers form first then for some reasons islands start to grow.
c) Volmer-Weber (3D islands): occurs when deposit atoms are more strongly attracted to themselves than to the substrate (i.e. $\Delta\gamma_n > 0$).

A fourth growth mode, which could be considered as the high-temperature version of layer-by-layer growth, is the so-called "step-flow" growth. In step-flow, all adatoms diffuse and adhere to step edges; therefore, no nucleation takes place on terraces. "If the temperature is reduced, the incoming flux is increased, or the distance between steps increased, not all incoming atoms may reach the step edge, and new islands may nucleate on the terraces"[74]. The difference between Step-flow and 2D-nucleation is shown in Figure 1.10. Steps are formed whenever the surface is cut slightly from a low index plane. In MBE, the transition from layer-by-layer growth in to step-flow diffusion is a well-known phenomenon that has been studied by RHEED [75];[76].

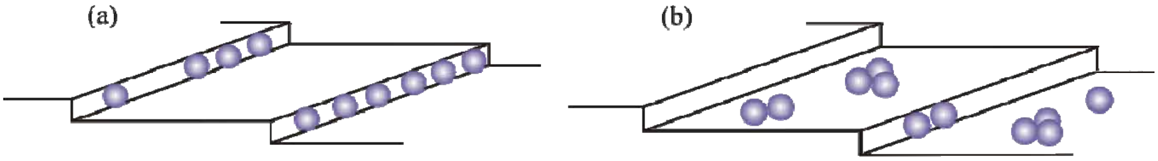

Figure 1.10: *(a) In step-flow growth, step edges act as the major sink for diffusing adatoms and no nucleation takes place on the terraces.*
(b) Layer-by-layer growth, in which nucleation on terraces also takes place.

2. Experimental

In this chapter, the main experimental approaches used for epitaxial growth and characterization are briefly described. The principles of the experimental techniques are introduced with their practical operation conditions. The chapter does not provide a complete description of the experimental details, but to define the physical and technical aspects which are necessary for understanding the experimental results to be presented in the following chapters.

2.1. Molecular Beam Epitaxy

2.1.1. Basics of molecular beam epitaxy

The first fundamentals of MBE growth were established in 1958 by Günther [77] and this technique has been used since the 1970 as an effective tool for the growth of high purity epitaxial layers of compound semiconductors [78]. Nowadays MBE provides the greatest flexibility for the growth of many kinds of complex semiconductor multilayers, ferromagnet-semiconductor hybrid structures, and epitaxial metal and oxide layers because of the precise control of the thickness and composition, the cleanliness of the growth process and the doping of the involved layers. It is a versatile technique for growing thin epitaxial structures via the interaction of one or several molecular or atomic beams that occurs on the surface of a heated crystalline substrate.

At the Institute of Semiconductor Technology, TU Braunschweig, the modified Varian Gen II MBE system with a vertical reactor is combined from three vacuum chambers: an entry/exit chamber, a buffer chamber, and a growth chamber. The entry/exit chamber is used to transfer samples from/to work bench and bake them at 250° C for at least 3 hours aiming to desorb water vapor and other impurities. The buffer chamber connects both entry/exit chamber and growth chamber and also used for preparation and storage of samples. The most fundamental components of ZnO MBE system that is used primarily for the work reported here are shown in Figure 2.1 schematically. It consists of double zone effusion cells, shutters, a continuous azimuthal rotation substrate holder, water cooled quartz thickness monitor at the substrate position and in-situ characterization with reflection high energy electron diffraction (RHEED).

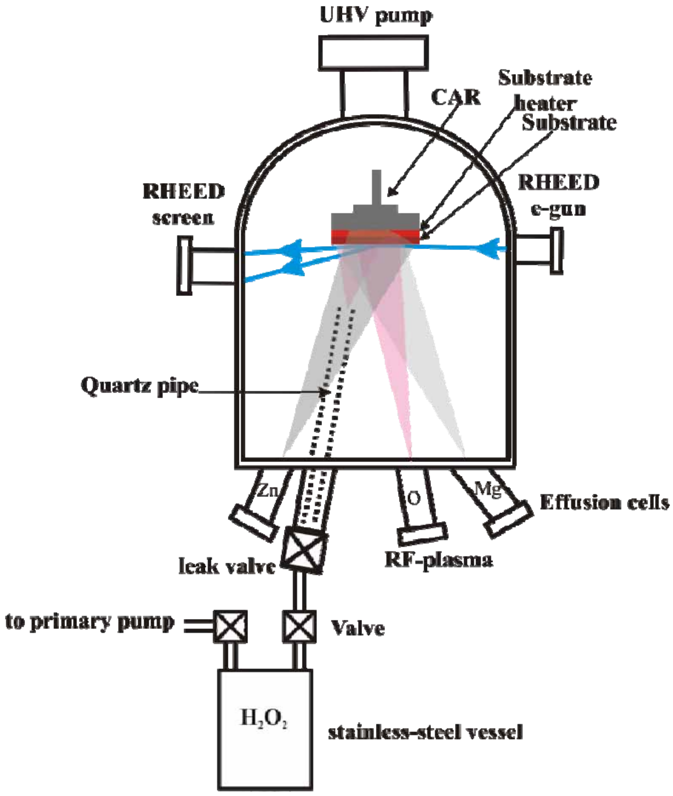

Figure 2.1: *Schematic presentation of the most fundamental components of a ZnO MBE system including a UHV system, substrate manipulator, and RHEED for in-situ analysis.*

To set up a MBE system for the growth of ZnO, a lot of improvements were carried out on a conventional MBE system. A UHV environment and high pure sources guarantee a low unintentional impurity level in the grown sample. The UHV pumping system is facilitated by the Turbo Molecular Pump (TMP). Normal ion pump cannot provide sufficient pumping rate to keep a good vacuum during growth, and the lifetime of an ion pump can be seriously diminished by the low vacuum (typical $1x10^{-5}$–$8x10^{-5}$ Torr) during growth. The growth chamber is pumped by a 2200 l/s TMP. The background can achieve vacuum better than 10^{-8} Torr without using liquid nitrogen. A differential pumping system is added to the RHEED gun so that even the pressure is higher than $8x10^{-5}$ Torr in the growth chamber, the local region that the filament is installed can be good enough for a stable operation.

Samples are loaded onto the growth chamber sample holder via a magnetically coupled transfer rod. The heater is directly attached to the sample holder that rotates on two axes. For improved layer uniformity, the sample holder is designed for continuous azimuthal rotation (CAR) of the sample. The substrate holder and all other parts that are heated are made of materials such as Ta, Mo, and pyrolytic boron nitride (PBN) which do not decompose or outgas impurities even when heated to 1400ºC. To monitor the residual gases, analyze the source beams, and check for leaks, a quadruple mass spectrometer (QMS) is mounted in the vicinity of the CAR. The material sources, or effusions cells, are independently heated until the desired material flux is achieved. Computer controlled shutters are positioned in front of each of the effusion cells to be able to stop the flux reaching the sample within a fraction of a second. The sources in the modified Gen II system are located approximately 52 cm from the sample in the growth position. This distance is large enough to guarantee high uniformity, even for larger wafers. The sources are designed specifically to grow ZnO-based semiconductors. The system has cells for Zn, Mg, Mn, N, and O.

2.1.2. Effusion cells

The effusion cells used in MBE systems exploit the evaporation process of condensed materials as molecular flux source in vacuum. The understanding of the properties of real effusion cells is complicated and not straightforward, so easier models are needed and just the main complications are subsequently added. In a closed crucible, for pure substances, equilibrium is established between the gas and the condensed phase. Such systems have only one degree of freedom *f*; that means that the pressure P_e is a function of the temperature T and can be approximately expressed by the Clapeyron equation [77]

$$P_e(T) = a\, e^{\left(-\frac{\Delta H}{KT}\right)} \tag{2.1}$$

Where; H is the evaporation enthalpy and K the Boltzmann constant. A close look to the fluxes of particles having a mass mi on the condensed phase surface shows that the maximum value for the evaporated flux $J_m[molecule(atom).cm^{-2}.s^{-1}]$ is

$$J_m = \frac{P_e}{\sqrt{2\pi m_i KT}} \tag{2.2}$$

This assumes that each molecule from the gas phase is always trapped by the surface and an equal opposite flux of material must leave the condensed phase to maintain the equilibrium pressure. Considering now that the impinging beam is partially reflected and only a fraction a is accommodate on the surface, the complete expression for the flux leaving the surface can be easily found as

$$J = \alpha J_m \tag{2.3}$$

The factor α is dependent on the microscopic status of the surface and is strongly unpredictable. An ideal Knudsen cell is composed of a large enclosure were the condensed material is in thermodynamic equilibrium with the gas phase and of an orifice so small that the equilibrium pressure p_e is not perturbed. In this ideal case, the orifice should be a surface with an evaporate pressure pe and has not the ability to reflect any of the incoming molecules resulting in $\alpha = 1$ and the number of molecules per time unit of the created beam is a J_m, where a (cm^2) is the orifice area. When it is not possible to consider the enclosure as infinitely large, and it is therefore important to consider the influences of the main body of the cell, the value of the α coefficient is needed [81].

The ideal Knudsen cell exhibits an angular distribution of the evaporated particles that follows a cosine law, where the angle θ is the angle between the beam and the substrate surface normal.

$$\frac{dJ}{d\Omega} = \frac{J_m}{\pi} cos\theta \tag{2.4}$$

$$J = \left[\frac{aP_e}{\pi d^2\sqrt{2\pi m_i KT}}\right] cos\theta \qquad (2\text{-}5)$$

where J $[\text{molecules(atoms)/cm}^2 \cdot \text{s}]$ is the flux at a distance d (cm) from the source opening to the substrate surface , which has an orifice of area a (cm^2) and contains atoms (molecules) of mass mi, having an equilibrium vapour pressure P_e at temperature T.

In ZnO MBE, these metal sources intend to have lower vapour pressure in oxygen ambient because of the formation of an oxide layer on the surface of source materials. The depth of oxidization may change according to both the utilization history and the operation condition of the effusion cell. To obtain stable beam fluxes, especially for Mg, in daily experiment becomes difficult. A more serious problem is that the source material may condense at the orifice of the crucible; where the temperature is lower than inside. This causes a rapid decrease in the beam flux with operation time. For this reason, a double zone effusion cells are used in the employed MBE system. The double zone cell consists of two filaments, one is used to heat the lower part of the crucible, and the other is used to heat the upper part. Each filament is independently powered and controlled by its own thermocouple. An insert cap with an outlet diameter of 1mm was used to reduce the outlet area of the effusion cell and also to give oxygen less possibility to get into the crucible. Further more, the pressure inside the crucible is much higher than in the chamber, so the any incoming oxygen will encounter a metal atom before reaching the solid surface. The rate of oxidation of the source metal is significantly reduced and it is more possible for any thin oxidised layer on the metal break up because the operating temperature is much higher the normal.

Figure 2.2: shows the Zn and Mg beam fluxes for different consumption periods. It is clear the Zn flux is not changing, but in Mg case the Mg flux decrease a bit because MgO was nucleate at the cap outlet. After cleaning the cap the Mg flux is again like new source without changing Mg matrial.

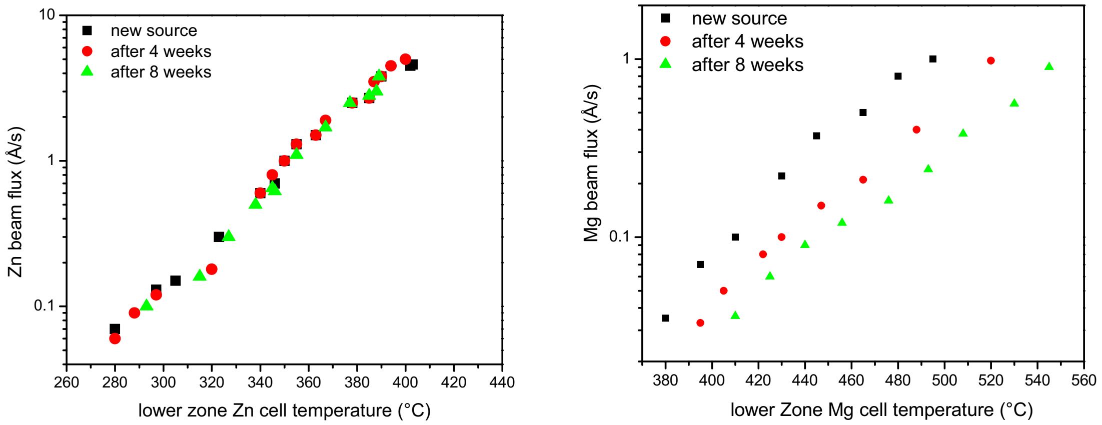

Figure 2.2: *Zn and Mg beam fluxes for different consuming periods from double zone effusion cells versus the base temperatures. The tip temperature is 150° C higher than base temperature. Data measured with water-cooled quartz thickness monitor at the substrate position.*

2.1.3. Oxygen sources for ZnO growth

Because of the high molecular bonding energy of O_2 (5.16 eV) [82] hindering the thermal dissociation of oxygen at the substrate surface, sources of reactive oxygen species are necessary for the growth of ZnO. Therefore, various types of sources are commonly used to produce reactive oxygen species and the type of oxygen source characterises the growth technique. However, these different techniques have their disadvantages. for example, plasma-assisted growth leads to contamination of growing films by source materials [83], possible surface damage by high-energy particles, and degradation of plasma sources due to high reactivity of oxygen radicals. The above problems stimulate the search for alternative sources of oxidizing species for the ZnO MBE, like radical oxygen, nitrogen dioxide [84], ozone [85], water (H_2O) [85] (It is important to note that, as we have found previously, ZnO does not grow when pure water vapour and elemental Zn are used.), and Hydrogen peroxide (H_2O_2). H_2O_2 is very reactive oxygen-containing compound. The main difference between a conventional MBE and the one used in this research is the possibility to use two different oxidization sources H_2O_2 or RF-plasma to provide reactive oxygen.

1. Hydrogen peroxide: H_2O_2 is extremely stable at ambient temperatures with losses of less than 1% per year at 23° C, but assay loss increases with temperature rise. For example, losses are 1% per week at 65° C. A 50 % aqueous solution of hydrogen peroxide kept in a stainless-steel vessel (This is the most suitable material for H_2O_2 equipment) at room temperature served as a source of reactive oxygen. A jet of vapor from the vessel was directed at the substrate through a quartz pipe connected to a leak valve (see Figure 2.1). During the growth of ZnO layers, the pressure in the chamber was maintained at $1x10^{-5}$ to $5x10^{-5}$ Torr by setting different H_2O_2 flows and this pressure, mostly defined by the H_2O_2 pressure, will be nominally referred to as the H_2O_2 pressure. The H_2O_2 pressure is directly related to the H_2O_2 flow and is a very convenient alternative for measuring and controlling the extremely low H_2O_2 flow.

2. Plasma source: In this research, an ADDON radio-frequency (rf) plasma source is used to generate O radical atoms. Included a commercial power supply unit of maximum 600 watts. The rf-matching box directly connected to the source with air-cooling. The plasma discharge is produced by inductive circuit water cooled around the cavity. The cavity is supplied by O_2 gas line via mass flow controller (MFC). Most experimental results in this work are based on the samples grown with this plasma source. Figure 2.3a shows ZnO growth rate is proportional to the oxygen flow rate with the plasma power until reaching 1 Å/s, 1.3 Å/s, and 1.6 Å/s ZnO growth rate at 350 W, 400 W, and 450 W plasma power respectively, after that, the ZnO growth rate starts to decrease slowly. Then, the change in growth rate does not reflect the total flux contributing to growth from the rf-plasma source, because the effective species should also involve the neutral oxygen atom and oxygen radicals. To ensure that the growth rate does not disturbed by the other parameters, such as Zn beam flux and growth temperature, the experiments were carried out under extremely Zn-rich condition and at the growth temperature high enough to re-evaporate the excess Zn impinging on the growing surface. Figure 2.3b The rf-plasma cell yields a 0.41 Å/s, 0.45 Å/s , and 0.5 Å/s ZnO O-controlled growth rate at 350 W, 400W, 450 W respectively, per a 1 sccm flow rate as was determined under the Zn-rich conditions.

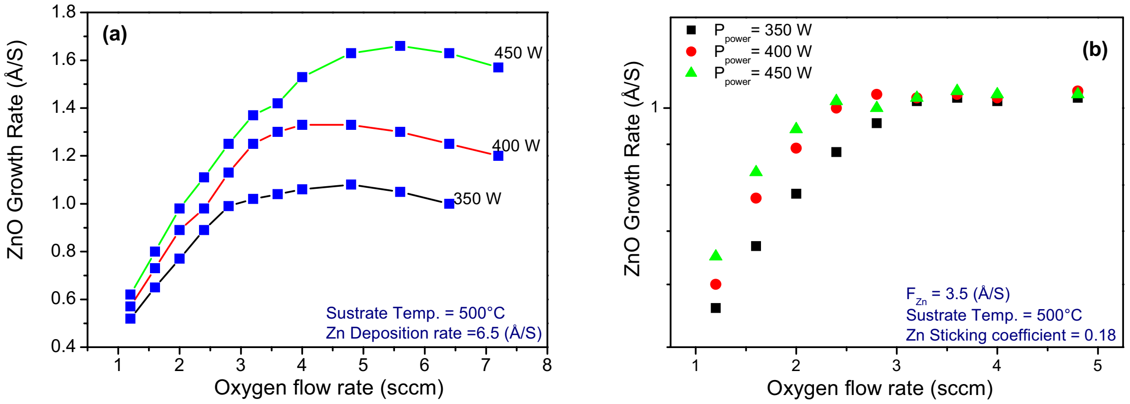

Figure 2.3: *ZnO growth rate is versus oxygen flow rate at different plasma power: a) under Zn rich condition .b) under Zn-rich condition-* stoichiometric- O-rich conditions

2.2. Reflection High-Energy Electron Diffraction

2.2.1. Principles and instrumentation

One of the most useful tools for in-situ monitoring of the growth is reflection high-energy electron diffraction (RHEED) [86]. It can be used to calibrate growth rates [88], observe removal of oxides from the surface[89], calibrate the substrate temperature [90], monitor the arrangement of the surface atoms, give feedback on surface morphology, and provide information about growth kinetics [91],[92]. The layout of the RHEED system is shown in Figure 2.4. In conditions which are usually used in MBE, the RHEED gun emits a high energy beam of electrons in the range 10−35 keV strike the surface at a shallow angle (1°-3°), making it a sensitive probe of the semiconductor surface. Electrons reflect from the surface and strike a phosphor screen forming a pattern consisting of a specula reflection and a diffraction pattern which is indicative of the surface crystallography. A charge-coupled device (CCD) camera with processing software monitors the screen and can record instantaneous pictures or measure the intensity of a given pixel as a function of time. The analysis and RHEED image and intensity were performed with a KSA 400 program.

Despite the popularity of RHEED, there is no complete formal theory for it. However, a number of simplified kinematical approaches have been introduced that are useful for understanding the basic idea of RHEED. They are sufficient for the determination of the unit cell dimension, crystal orientation and the crystal shape. The lack of a formal theory is the reason behind the debate over the interpretation of RHEED results [93].

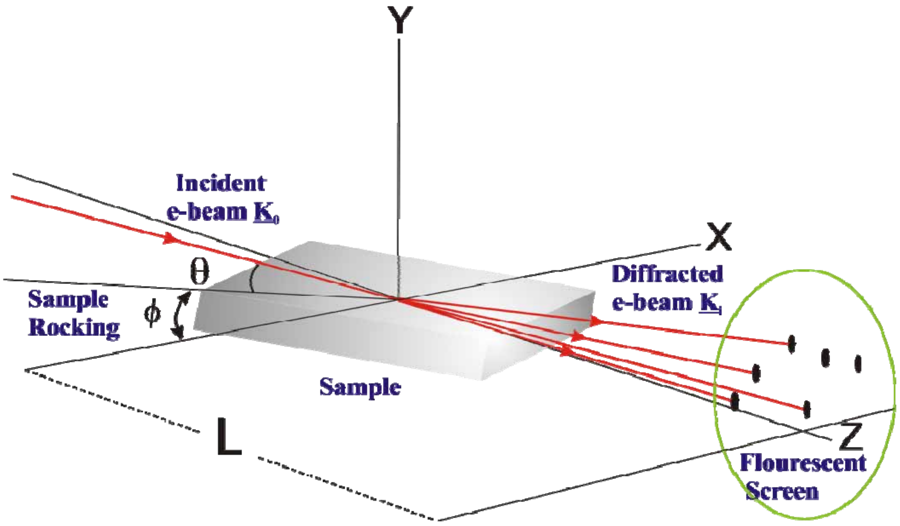

Figure 2.4: *An illustration of the fundamentals of RHEED*

The simplest theory to describe RHEED is the “geometric theory” [86], in which diffraction of a plane wave (of wavevector k) by a single crystal is assumed. No interaction mechanism is taken into account in this treatment. Because of its simplicity, this theory is widely used for experimental calculations. In this theory, diffraction results when the Laue condition is satisfied, i.e.,

$$K-Ko = G \tag{2.6}$$

where ' K and K0 are the wave vectors for the diffracted and the incident beams respectively and G is the reciprocal-lattice vector. When considering only elastic scattering events, which means $|K_o|=|K|$, this condition is satisfied by an infinite number of ' K vectors pointing in all directions, which is the origin of the so-called Ewald sphere. The sphere around the origin of K with radius |K| then defines the Ewald sphere (Figure 2.5). Hence, the Laue condition may be re-formalized as “diffraction occurs for all ' K connecting the origin of the sphere and a reciprocal-lattice point” [86], [94]. The magnitude of the wavevector for high-energy electrons is given by:

$$K_0 = \frac{2\pi}{\lambda} = \frac{1}{\hbar}\sqrt{2m_0qV + \left(\frac{qV}{c}\right)^2} \tag{2.7}$$

Where; m_0 is the electron rest mass, q is its charge and V is the accelerating potential.

2.2.2. Ewald sphere construction

A graphical representation of the conditions for diffraction is provided by the Ewald Sphere construction. A 2-dimensional representation is shown in Figure 2.5, where the incident wave vector K_0 is drawn to terminate at the origin of a reciprocal lattice (a square lattice in this case). A sphere drawn with radius K_0 and with center O is the Ewald Sphere. If a point on the reciprocal lattice lies on the surface of the Ewald Sphere, the condition for elastic scattering is satisfied and diffraction will occur with the scattered beam having wave vector K. The vector G connecting K_0 and K is a reciprocal lattice vector. By varying either the energy, i.e. the length of the incoming wave vector, of the incident beam, or the orientation of the crystal relative to the beam, all reciprocal lattice points may be mapped.

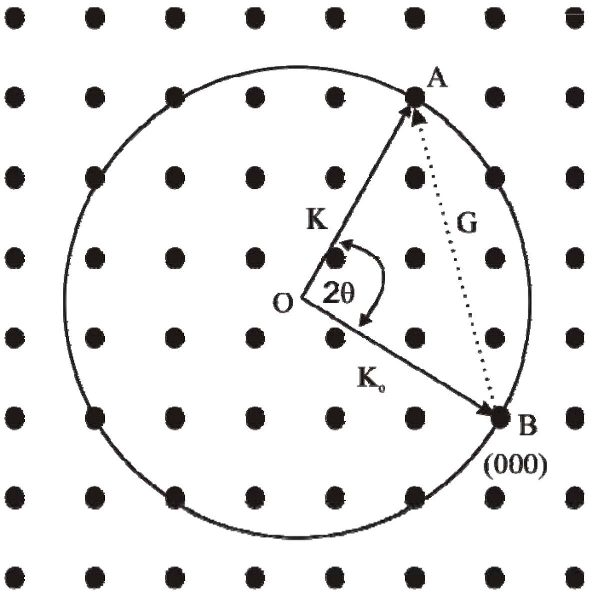

Figure 2.5: *Top view of 2-dimensional representation of Ewald sphere construction.*

In surface physics the 2-dimensional arrangement of atoms that forms the boundary between the bulk crystalline structure and the ambient environment are more intereste. The reciprocal lattice of a 2-dimensional array is no longer a set of points, but rather a set of infinitely long rods extending normal to the surface and having the periodicity of the surface unit mesh. To understand this, consider that distances in reciprocal space are inversely proportional to distances in real space. Therefore if points move farther apart in real space, the associated reciprocal space points move closer together. In the direction normal to a crystal surface the real-space spacing of atoms is removed to infinity, so the reciprocal lattice points are packed infinitely close together to form continuous rods normal to the atoms forming the surface reciprocal mesh.

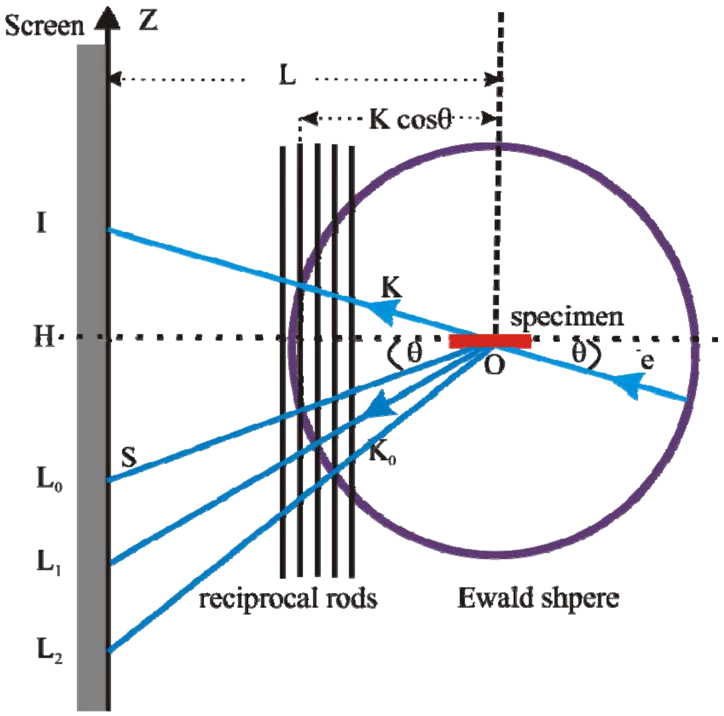

Figure 2.6: *Ewald sphere construction and diffraction geometry of RHEED in side view. Intensity maximum on the screen denoted by Lx corresponds to projected intersections of the Ewald sphere with the reciprocal lattice. S denotes the specular sport meaning the mirror reflection of the electron beam.*

In RHEED, the Ewald sphere is large, for 20 keV electrons K_0 is 785nm^{-1}[86], which is about 200 times larger than the reciprocal lattice unit of ZnO. This means that it produces an almost planar cut through the first few Brillouin zones of the reciprocal lattice. This large radius of the Ewald sphere combined with the small scattering angles facilitates the geometrical interpretation of RHEED patterns, since for many purposes angular distortion can be neglected and the usual small-angle approximations for the trigonometric functions are valid. RHEED is very surface sensitive in that it samples only very few atomic layers beneath the surface. In the construction of the reciprocal lattice therefore we can approximate the sampled volume by two-dimensional layer. The reciprocal lattice then degenerates into a set of one-dimensional rods along the *Z* direction perpendicular to the surface. Using this reciprocal lattice, we get the Ewald sphere construction of continuous rods, as is shown in Figure 2.6. Every rod reproduces a reflection in the diffraction pattern. The reflection occurs on so-called Laue circles of radius L_i centered at *H*, the projection of the component parallel to the surface of k_0 onto the screen. The specular reflection or the specular spot *S* located at the reciprocal lattice is projected on *I*, also labeled (000), where some of the incident beam that misses the sample becomes visible.

2.2.3. Diffraction pattern and surface structure

For semiconductors, it is evident from many experiments that the real surface does not exhibit the same atom arrangement as in bulk. The simplest rearrangement is surface relaxation, where the topmost layer retains the bulk symmetry, but the atomic distances perpendicular to the surface are different from that of bulk. Surface relaxation does not reflect in the symmetry of RHEED pattern, however, can be investigated by analyzing incident angle dependent intensity profile, called RHEED rocking curve. Besides the surface relaxation, surface reconstruction is a stronger disturbance giving rise to rearrangement of the top layer into symmetries different from the surface of a bulk truncation. Such a rearrangement is easily observed by RHEED. For a reconstructed surface, additional fractional patterns appear together with the primary patterns. Since both the reconstructed and normal surface contributes to the primary patterns, they usually are more intense than the fractional pattern. The surface reconstruction reflects the chemical stoichiometry of the surface, hence can be used to control the growth condition.

A real surface should also involve the information from the surface morphology, which reflects in RHEED pattern by intensity distribution. One can image that the reciprocal rod of a real surface broadens anisotropically and un-uniformly along the rod. So that the interaction between the Ewald sphere and the reciprocal rods show modified streaky pattern. If the surface is very rough, the pattern becomes diffraction spots since the electron beam transmit the small island on the surface.

2.2.4. Intensity oscillations and growth dynamics

Since the first report in 1980, RHEED oscillations have been intensively studied because they convey in situ and real-time information on the dynamics of MBE growth. This allows their use not only as an analytical tool, but also for real time feedback control in, for example, phase-locked MBE. RHEED oscillations are generally observed under growth conditions that lead to layer-by-layer growth. In this growth mode, also called Frank–van der Merwe growth, one layer is essentially completed before material is added to the following layer. This periodic variation of the surface morphology, or surface coverage, is generally accepted as the reason for RHEED oscillations [95], [96]. From the RHEED oscillation measurements several parameters that characterize the oscillations can be extracted and analyzed. They are period, amplitude, phase and damping of the oscillations, the behavior at initiation of growth, the recovery after stopping the growth and the frequency distribution in the Fourier spectrum of the oscillation. In favourable cases, a study of these parameters as a function of either growth conditions or diffraction parameters allows the analysis of the growth mechanism as well as the nature of the surface. During layer-by-layer growth in MBE, the surface periodically changes its morphology because of the nucleation and coalescence of islands in the growing layers. The damping of the oscillations and the recovery after growth both happen on the timescale considerable longer than the oscillation period. We can interpret this as increase of long-range roughness that approaches a steady state in the limit of totally damped oscillations, which means the density of two dimensional islands does not change any more when the oscillations damps. After growth interruption, the surface again becomes smooth toward the thermal dynamic equilibrium state. As soon as the surface undulation due to the long-range roughness creates average terrace sizes comparable to the mean nucleation distance of the layer-by-layer growth, the oscillations are damped out. Every deposited atom reaches a step edge before forming an island nucleus and growth proceeds, at least locally, by lateral translation of the terrace distribution. This notation can be verified by measuring RHEED oscillations on vicinal surfaces. When the growth temperature and with it the surface mobility of the adatom is increased, the amplitude of the RHEED oscillations decrease until completely disappear. This transition from layer-by-layer growth to step-flow growth has been used to obtain estimates of the adatom surface mobility[96].

2.3. Atomic force microscopy

Atomic Force Microscopy (AFM) is a robust technique used to study the surface topography of a variety of materials on the nanometer to micrometer scale. It was invented by G. Binnig et al [98] in 1986, and he [99] reportedly obtained atomic resolution of a graphite surface utilizing AFM. In the recent decade AFM has become a universal tool in material research. AFM primarily measures surface topography on a scale from angstroms to 100 microns, but has other variants that measure electrical, magnetic, and physical properties [100]. The technique involves imaging a sample through the use of a probe, or tip, with a radius of about 20 nm. The tip is held several nanometers above the surface using a feedback mechanism that measures surface–tip interactions on the scale of nano-Newton. A detector measures the cantilever movement as the tip moves over the sample. From these tip movements and data from the detector, a computer is used to reconstruct a map of the surface morphology. In this research, AFM DME in AC-contact mode will be used to investigate the surface morphology of ZnO-based semiconductors grown under different growth conditions.

2.4. Scanning electron microscopy

Scanning Electron Microscopy (SEM) is a high-resolution surface imaging technique based on the detection of secondary electrons generated from the specimen in an inelastic process. The earliest known work describing the concept of the SEM is that of M. Knoll in 1935 [101]. Today the SEM is a quasi-standard tool for the analysis of surface morphology and is widely used in the field of semiconductors. In a typical SEM system, primary electrons are generated by thermionic emission from a cathode in an electron gun and are accelerated by a variable voltage of 500 V–30 kV in ultra-high vacuum. The electron beam cross section at the electron gun is demagnified by a two- or three-stage magnetic lens system to a final electron beam probe diameter of 1 nm – 1 μm with an electron current of 10^{-12}–10^{-8} A at the specimen. Scanning coils placed before the final lens causes the electron spot to scan across the specimen surface in the form of a square raster. The current that passes through these coils are usually also made to pass through the deflection coils of the cathode ray tube or picked up as electronic signals and regenerated on a computer screen to generate the image.

Upon impinging on the specimen, there is an interaction between the atoms and electrons in the sample. This interaction causes various signals to be generated and the most commonly used signals are those from secondary and elastic back-scattered electrons. The secondary electrons are electrons of very low energy and thus contain information of only a few angstroms deep on the surface of the layer. These electrons are then detected by a detector consisting of a scintillator-photomultiplier combination. These images are the ones commonly used in SEM to interpret the morphology of a sample.

2.5. X-ray diffraction

X-rays were discovered by Wilhelm Conrad Röntgen discovered in 1895, for which he later obtained the Noble prize for Physics in 1901. X-ray diffractometry (XRD) was later introduced by Max von Laue in 1912 when he discovered the diffraction of x-rays on crystals. Since then XRD is one of the widely used experimental techniques for determining lattice parameters, preferred orientation of the crystal, phase composition (qualitatively and quantitatively), grain sizes, lattice strain, residual stress etc. Since all semiconductor properties are directly related with the structure and hence crystalline quality of the semiconductor material, XRD provides qualitative and to a certain extent, quantitative analysis of grown crystals [98], [102]. Due to the wavelength of the x-rays used and their reachable diffraction space resolution, the method is sensitive for thin films from a few monolayers to several micrometers. XRD is a nondestructive technique and can provide the information from a relatively large area of the specimen compared to Transmission Electron Microscopy. A schematic presentation of the set-up including angular movements that identify the type of measurement is shown in Figure 2.7.

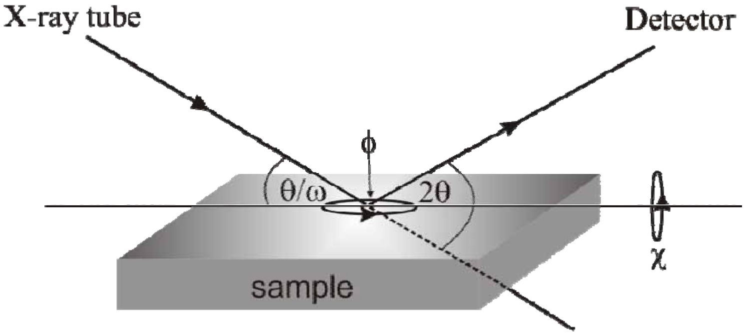

Figure 2.7: *Schematic of an XRD measurement set-up and angular movements that identify the type of measurement*

Figure 2.8 shows the diffraction of x-rays from a crystal. In principle, x-rays of the same wavelength λ are incident at an angle θ to the given plane with a geometric periodic system, for example, a crystalline material of atomic layer separation d. The x-rays are diffracted at the same angle θ to the plane (law of reflection). In semiconductors, x-rays are diffracted in the crystal lattice.

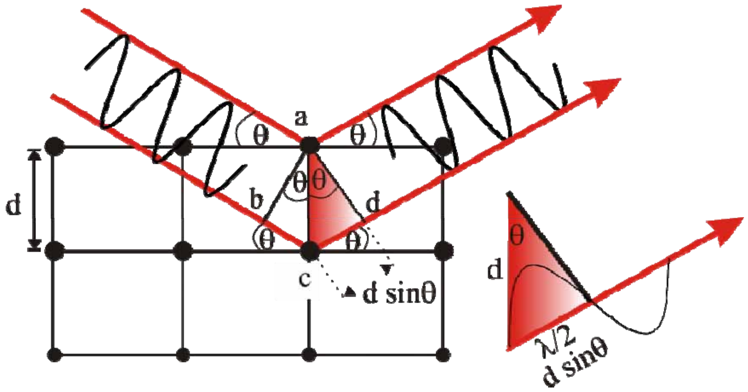

Figure 2.8: *Interaction of x-rays with a crystal*

The diffracted rays can either interfere constructively of destructively. For constructive interference, the path difference bc+cd must be equal to a whole number of wavelengths n, as described by Bragg law:

$$n.\lambda = 2d.sin\theta_B \,, n = \text{integer} \qquad (2.8)$$

The highest intensity I_{max} of the diffracted x-rays is given by $I(\theta=\theta_B) = I_{max}$, where, λ is the wave length, $\theta_B$is the Bragg angle, d_{hkl} is the distance between the planes and n is an integer. For a hexagonal crystal structure, the crystal planes can be described with four Miller's indices (*hkil*) as an extension of the three indices (*hkl*) in cubic crystals. Considering a hexagonal crystal with horizontal lattice parameter a, and vertical lattice parameter c, the distance d_{hkil} between two successive atomic layers is given by:

$$d_{hkil} = \frac{ac}{\sqrt{\frac{4}{3}c^2(h^2+hk+l^2)a^2l^2}} \tag{2.9}$$

In this work, a Siemens D5000, Phillips, and Seifiert with a four crystal monochromator available at the x-ray tube of this diffractometer system is run with a 40 kV, 40 mA bias to generate Cu-Kα1 rays with a wavelength of 0.154056 nm.

Mainly two kinds of scans are used for thin film characterization [103]. One scan is θ–2θ radial scan or ω–2θ scan for measuring a Bragg reflection. In the reciprocal space, ω–2θ scan measures the intensity profile along the reciprocal vector (Figure. 2.9). For such a scan, the detector is rotated twice as fast and in the same direction around the diffractometer axis as the specimen. This leads to a corresponding change in the angle of diffraction and the moved detector can still detect the diffracted rays. A Δθ change in the angle of incidence caused by the moving source leads to a 2Δθ change in the line of sight between the detector and the sample. With this mode diffraction signals from other multiples of the fundamental reflex can be detected, if they are available. For example, if the (0002) and (0004) reflection peaks are available in a 2θ spectrum of a ZnO crystal, then the crystal is oriented towards the c-axis of ZnO. Besides the crystal orientation, the width of 2θ peaks that result from ω–2θ scans also gives information about the crystalline quality.

The other scan is ω transverse scan or ω rocking curve, in which the detector is fixed in position with wide-open entrance (in order to increase the signal intensity by necessary) and the sample is rotated. . In reciprocal space, ω rocking curve corresponds to a scan across the reciprocal point perpendicular to the associated reciprocal vector (Figure 2.9).When the Bragg condition (equation 2.8) is satisfied a diffraction maximum arises and the diffracted x-rays are detected by the detector and channelled to an electronic signal processing system that calculates the angle of diffraction and the intensity of the diffracted x-rays and presents the result as a spectrum of different Bragg angles, with a peak at the most common angle of diffraction. If neighbouring atoms on different atomic layers in a crystal are not perfectly aligned, the Bragg angle θ_B will not be the same for every atomic layer. The more the Bragg angles deviate from the most common one, the broader the spectrum of diffraction angles (commonly called rocking curve) and the more the disorder in the atomic ordering in the crystal being characterised.

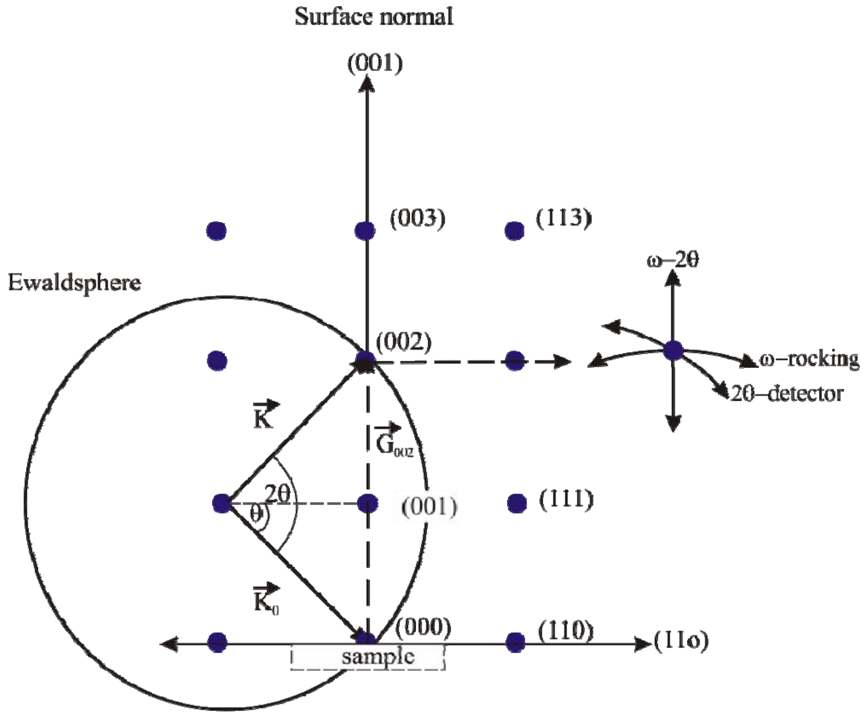

Figure 2.9: *Ewald sphere construction and diffraction geometry of (002) reflection in reciprocal lattice. Scan directions of XRD ω–2θ scan, ω scan, and 2θ detector are presented on the right.*

The physical origins of the peak broadening are different for ω–2θscan and ωrocking curve. In the case of ω–2θ scan, which is described by the Bragg's law broadening in the scan angle is determined by the number and the uniformity of the interlayer distance of the diffraction planes. The uniformity of the interlayer distance of the diffraction planes involves the information of defects in the sample, which is what we want to deduce by the measurement. In the case of ω rocking curve, which is measuring the angle distribution of the diffraction planes, the corresponding information is the mosaicity of a film. The mosaicity is a simplest model that explains diffuse X-ray scattering from a relaxed layer. As standard, the (0002) reflex is taken for rocking curve measurements. X-rays may slightly differ in wavelength and this also affects their angle of diffraction at the point of incidence. Using monochromators to narrow the wavelength spectrum leads to more accurate results. Although the spectrum of x-rays might be narrower after passing the monochromators, large beam diameters would lead to different angles of incidence and thus affecting the angles of diffraction too. Employing slits between the monochromator and the sample will definitely lead to reduced rocking curve widths.

2.6. Transmission electron microscopy

The original form of the Transmission electron microscopy (TEM) was first constructed by Max Knoll and Ernst Ruska at the end of the 1920's at the Technical University of Berlin. TEM is applied to obtain an image of the specimen at high resolution and magnification. From the crosssectional TEM (XTEM) technique, or high-resolution TEM (HRTEM) imaging, the crystallography and microstructure of the system can be investigated to the finest detail. Because XRD analysis gives only ensemble information about the degree of ordering in semiconductor crystals, TEM was employed in this work to view the atomic ordering in the ZnO crystals and also to study the interface between the ZnO epilayer and the MgO buffer and their substrate. In the present work, TEM measurements were carried out at the Physics Department of Aristotle University, Greece. While the HRTEM measurements were carried out at Research Institute for Technical Physics and Materials Science, Hungarian Academy of Sciences.

Conventional TEM set-ups comprise an illumination system (electron gun and a series of lenses), and an imaging system with objective, magnifying, projector lenses and a fluorescent screen. These systems are in a chamber under ultra-high vacuum. The ray diagram of a conventional TEM is drawn schematically in Figure 2.10. Two operation modes can be used, i.e. imaging mode and diffraction mode (Figure 2.10a and b, respectively). In the imaging mode, an image is observed in the image plane on the viewing screen (Figure 2.10a), while in the diffraction mode a diffraction pattern is projected to the viewing screen by changing the strength of the intermediate lens (Figure 2.10b). The contrast in conventional TEM is mainly due to diffraction/scattering contrast and mass-thickness contrast. These are based on the scattering cross-section of the atomic species in the specimen and the number of scattering atoms along the propagation of the electron beam. Strongly scattering regions of the specimen (heavy elements, large thickness) show darker contrast in the bright-field image than weakly scattering regions (light elements, small thickness).

The diffraction pattern of an amorphous specimen consists of diffuse rings, whereas a crystalline specimen generates diffraction spots. These spots are formed due to the constructive interference between the diffracted beams that Bragg condition (2.8). Depending on which diffraction spot contributes to the image formation, bright-field (BF) or dark-field (DF) images can be obtained. A BF image is formed, when only the direct beam is selected by the objective aperture, which is inserted in the back focal plane of the objective lens. For obtaining a DF image, the objective aperture is shifted in such a way that only one of the diffracted beams is contributing to the image formation. Since this beam runs off-axis, its electrons suffer from the spherical aberration and astigmatism of the lenses more than the

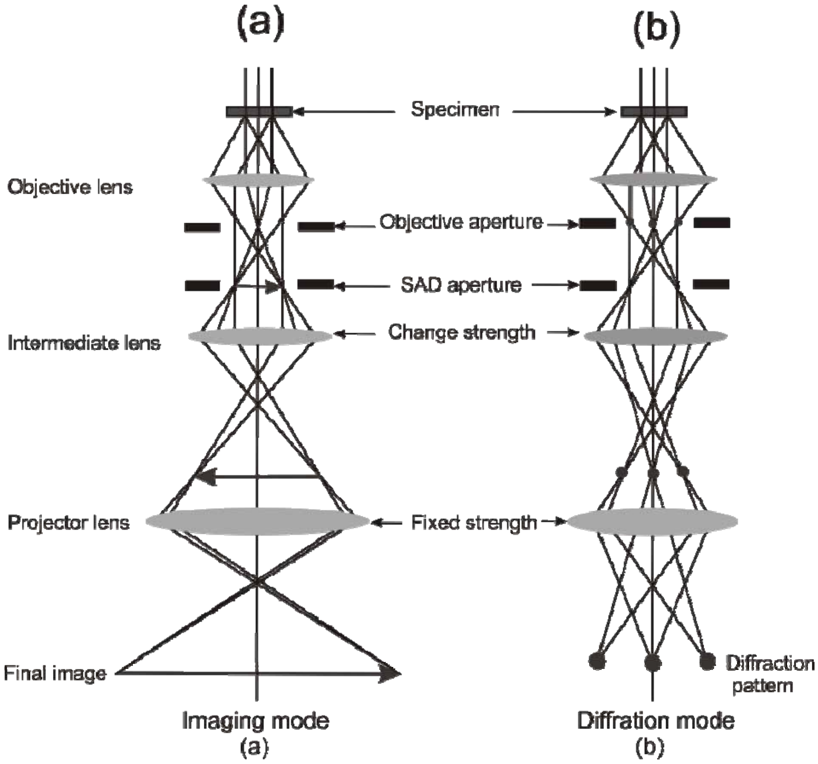

Figure 2.10: *Schematic ray diagram of the conventional TEM: (a) projection of the image onto the viewing screen, and (b) projection of the diffraction pattern onto the viewing screen. [104]*

In this work HRTEM has been employed for the study of ZnO/MgO/Al_2O_3 interfaces. HRTEM image formation is in accordance with Abbe's theory [105], which states that at least one diffracted beam and the direct beam have to be used to form an image. In order to resolve the fine details of the specimen, i.e. atomic columns, also large values of the k vector have to contribute to the image. The HRTEM image can be understood as a complex interference pattern of the various diffracted beams and the direct beam. This interference pattern depends on the imaging conditions and the thickness of the specimen. These reasons require HRTEM image simulations to retrieve the atomic structure of the specimen. For that, a model of the specimen structure has to be assumed. During the simulations, the microscope parameters are used as an input and image intensity patterns are calculated. A digital comparison between simulated and experimental images is performed, and the initial simulation parameters are varied until the best agreement is achieved. A short description of the image formation in HRTEM and image analysis is given farther below. A more detailed description can be found in [105].

For XTEM ZnO specimen preparation two strips of the specimen were cut along the $(11\bar{2}0)$ also on the $(10\bar{1}0)$ directions, and glued face to face on the (0001) plane, then were mechanically thinned down to 25 μm. Subsequently the specimens were thinned to electron transparency by Ar ion milling with energy of 4 kV, at a very low incident angle of 4° in order to avoid artefacts due to amorphization by the argon ions. The cross-sectional HRTEM specimen was additionally thinned at a low energy of 0.5 kV in order to etch out the amorphous layer produced by the high-energy ion milling.

2.7. Photoluminescence spectroscopy

Photoluminescence (PL) is the most widely used optical characterization method. This is because (see section 1.000) PL provides rich information on both intrinsic recombination processes and various radiative recombination processes associated with imperfections of a sample through a fast nondestructive way. The information about the electronic structure of semiconductor could be obtained from the analysis of luminescence spectra.

Two types of spectra can be distinguished upon PL measurements: PL spectrum and photoluminescence-excitation (PLE) spectrum. PL spectrum refers to the variation of luminescence intensity as a function of wavelength (or photon energy), while PLE spectrum is measured by monitoring the variation of luminescence intensity at fixed wavelength (or photon energy) as a function of the wavelength (or photon energy) of the excitation source. PL spectrum provides us the information about the structure of energy levels in the sample. PLE spectrum provides information about the energy transformation among the energy levels in the sample.

In PL, samples are usually mounted in an optical cryostat in order to achieve low temperatures. A lamp with a monochromator or a laser with tunable wavelength is used for the PL excitation. In this research, a He-Cd laser with emission wavelength of 325 nm is used as the excitation source for the ZnO study. The laser beam passes through filters which select the main laser emission line and cut off undesirable lines, and is then focused to a small spot on the sample. The luminescence from the sample is collected by condenser optics and converted to a collimated beam. The beams that pass through the spectrometer are detected by a CCD camera and are converted to an electrical signal (see figure 2.11). The ac signal is then fed to a lock-in amplifier, and the amplified signal is inputted into a computer to be collected and analyzed.

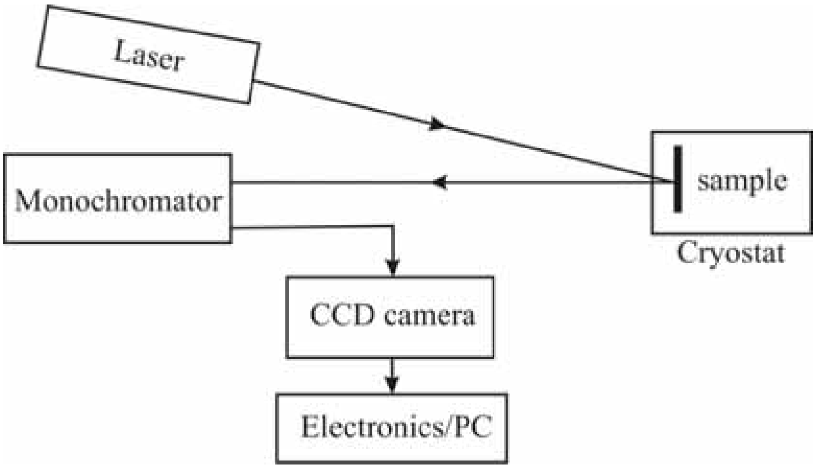

Figure 2.11: *Schematic illustration of PL measurment*

For PL measurements, a 10 mW, 325 nm He-Cd laser was used as the excitation source and a grating monochromator (Triax 320) and photodetector (CCD 3000) were employed.

During the PLE measurements, the emission of a 150 W cw Xe arc lamp was passed through a grating monochromator and focused on the sample. The PL intensity was detected by a grating spectrometer equipped by a photomultiplier tube, working in a photon counting mode. In these experiments the PL intensity was recorded as a function of the excitation wavelength.

For Time-resolved PL (TRPL) spectroscopy at 1.8 KThe triple-frequency emission from a Ti: sapphire mode-locked laser (260 nm wavelength) was used for transient PL measurements. The frequency of the subpicosecond laser pulses was 76 MHz. The diameter of the spot on the sample was about 0.3 mm. The polarization of the laser emission was linear. The PL transients were detected by a UV sensitive Hamamatsu streak camera system with a temporal resolution better than 15 ps.

While photoluminescence (PL) measurements were carried out at the Institute of Semiconductor Technology, Technical University Braunschweig, PLE and TRPL measurements were performed in Ioffe Physico-Technical Institute, St.Petersburg, Russia

2.8. Hall-effect measurements

In semiconductors, both electrons and holes contribute to the current, and thus, the bulk conductivityσ($\sigma = \frac{1}{\rho}$) where ρ is the resistivity) can be expressed as:

$$\sigma = ne\mu_e + pe\mu_h \tag{2.10}$$

In the case of an intrinsic semiconductor:

$$\sigma = \sigma_0 \exp\left(-\frac{E_g}{2K_BT}\right) \tag{2.11}$$

Thus, by ignoring the temperature variation σ of and by plotting lnσ as a function of $\frac{1}{T}$ (which yields a straight line), the energy gapE_g can be derived from the slope $-\frac{E_g}{2K_BT}$. In the case of an extrinsic semiconductor, for $n \gg p$ the material is an n-type semiconductor, and for$p \gg n$ the material is a p-type semiconductor. In order to determine the carrier type, in addition to the conductivity (resistivity) measurements, a complementary measurement, such as Hall-effect is required.

Hall-effect measurements on semiconductors are routinely employed for determining the density and sign of majority carriers. The sign and density of the majority carriers can be easily determined, as well as their mobility. In addition, temperature-dependent measurements can extract information about impurity energy levels within the band gap and the concentrations of those impurities. This information is essential for the development of semiconductor devices, and is a very useful research diagnostic.

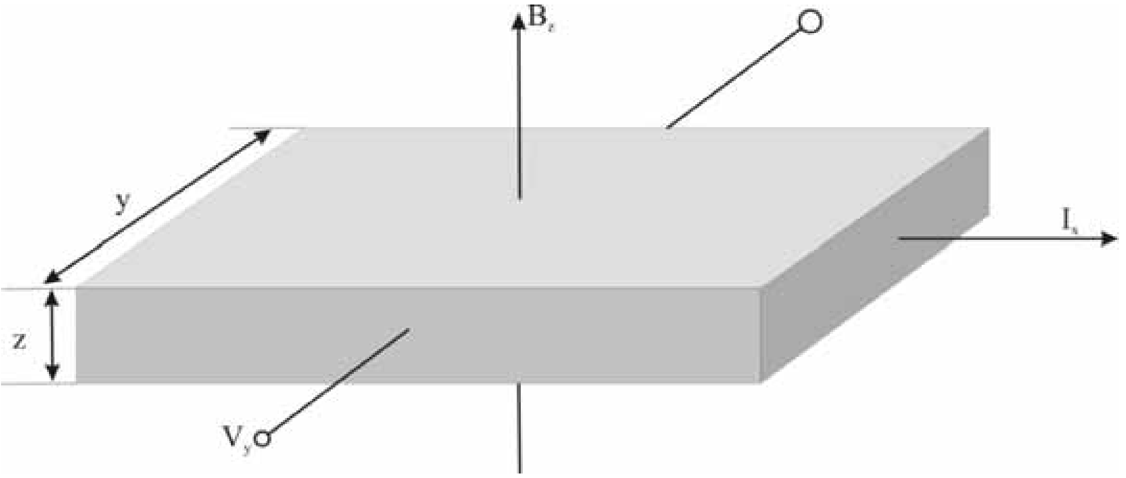

Figure 2.12: *Schematic diagram of Hall-effect measurment*

In this measurement (see Figure 1.12), the magnetic field B is applied (along the z-direction) perpendicular to the current flow direction (x-direction). The charge carriers, moving through a semiconductor, are deflected due to a Lorentz force exerted by an applied magnetic field. As a result of this deflection, a potential difference is established across the side of the semiconductor that is transverse to the magnetic field and the current direction. The Hall voltage $V_y$and electric field E_y ($V_y = yE_y$; y is the sample width) appear according to:

$$E_y = R_H J_x B_z \tag{2.12}$$

Where; $J_x = I_x/yz$ is the current density; $R_H$is the Hall coefficient, which is negative for n-type semiconductors, and it is positive for p-type semiconductors. In other words; for n-type semiconductors $R_H = -(ne)^{-1}$ where for the case of p-type semiconductors $R_H = -(pe)^{-1}$. Thus; from measured the density of carriers in the semiconductor can be determined, and from the field polarity, the conductivity type can be ascertained. If the conductivity of a semiconductor is known, the (Hall) mobility can be also determined from Thus, from $\mu_H = \sigma R_H$ combined conductivity (resistivity) and Hall-effect measurements, the carrier density, type, and mobility can be determined. From these measurements as a function of temperature, one can also derive the temperature variations of the carrier density and mobility.

The doping range sensitivity of this method is between 10^{14} and 10^{19} cm^{-3}. It should be noted that one should distinguish between the Hall mobilityμ_H and drift mobility μ the ratio of over can typically vary in the range between 1 and 2 depending on the dominant scattering mechanisms, which in turn depend on temperature and doping concentration.

2.9. Electrochemical capacitance–voltage profiling

The Electrochemical capacitance–voltage profiling (ECV) technique was developed by Ambridge and co-workers more than 25 years ago [106]. It has the advantage over Hall measurements in that it can determine the uniformity of doping with thickness and characterize multilayers with multiple doping levels, including p-n junctions. In this apparatus (see Figure 1.13), the traditional metal Schottky-metal ohmic contact for the C-V measurement is replaced by a conductive electrolyte solution. Variation of the voltage on the electrolyte cell leads to dissolution of the semiconductor, so that the semiconductor may be repetitively etched and measured, leading to a highly accurate measurement of carrier concentration versus depth in the sample. Both the electrolytic dissolution and the etching are performed in the same measurement apparatus, and a small AC signal (<<1 V), typically at a low frequency of 0.3–3 kHz is superposed on the DC bias during the capacitance measurement step.

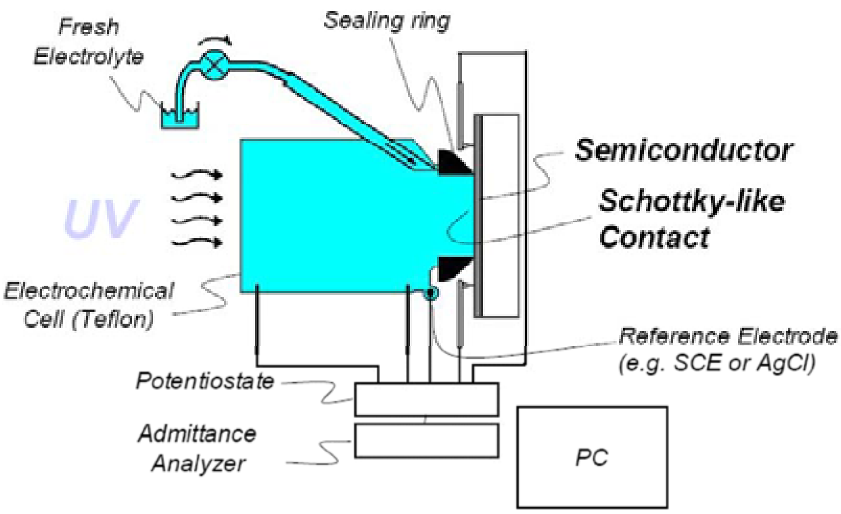

Figure 2.13: *Electrochemical capacitance–voltage profiling measurement setup*

In contact with an electrolyte, semiconductors can be etched by four different methods (chemical, photochemical, electrochemical, and photoelectrochemical) depending on whether or not holes are supplied from an external circuit or generated by above band-gap radiation to aid the etching process. In ECV profiling of n-type material, it is essential that etching occurs only when the sample is illuminated by above band-gap radiation (UV light) which generates holes that are subsequently transported to the surface by an applied bias. The required etching mode is, photoelectrochemical and we require the rates of all other etching processes to be as small as possible. The measurement and etching processes are then separated and Faraday's Law of Electrolysis is used to calculate the amount of material removed and, hence, the etched depth. The other three etching processes will lead to incorrect estimates of the etching depth. For most semiconductors the correct choice of electrolyte means that only photoelectrochemical etching occurs, for example, GaAs related III–V materials are routinely profiled using NaOH as the electrolyte. However, unlike other wide band-gap semiconductors, ZnO is amphoteric and soluble in both acidic and basic solutions. Even very dilute acidic (HCl) and basic (NaOH) solutions chemically etched ZnO with very high etching rate. Thus, we have found that the chemical etching rate can be reduced below the limit of sensitivity by using slightly acidic solution 0.1 M $ZnCl_2$ as an electrolyte.

3. ZnO heteroepitaxy

ZnO layer can be grown either homoepitaxially or heteroepitaxially on foreign substrates. The best choice is homoepitaxy, in which case one employs a substrate whose lattice parameters, crystal structure and thermal expansion coefficient are the same with those of the material to be grown. In heteroepitaxy, the substrate material and the material to be grown are different. The use of suitable substrate is an important aspect in the growth of semiconductors, to reduce the strains, crack and dislocation density in epitaxial films. In the absence of homoepitaxial substrates, substrates with the similar crystallographic symmetry, smallest lattice mismatch and close in-plane linear expansion coefficients should be chose. Heteroepitaxial ZnO films were successfully deposited on different substrates such as, Si, GaAs, but Si and GaAs, are not expected to be appropriate substrates because of the formation of an amorphous-like oxide layer at the substrate surface, which destroys the following epitaxial growth. Since the lattice mismatch between GaN and ZnO is 1.8%, and GaN is one of the most chemically robust semiconductors, one could expect that GaN is a good substrate material for ZnO heteroepitaxy. However studies showed that polycrystalline Ga_2O_3 layer forms at interface if no special pretreatment is carried out. It seems that only oxide Substrates can avoid oxidation and to be used as the substrate for ZnO heteroepitaxy. $ScMgAlO_4$ is an oxide substrate and has only 0.2% lattice mismatch with ZnO, it was also the first substrate, on which ZnO-based light-emitting diodes were realized [107]. However, the unavailability of this substrate makes it less promising for commercial ZnO growth. Indeed, previous studies show that, the best ZnO films were deposited on sapphire substrate, using chemical vapor deposition, pulsed laser deposition, and rf-MBE, H_2O_2-MBE. However, due to the large lattice and thermal mismatch between sapphire and ZnO, the ZnO film suffers from high dislocation density. Now the issue is how to accommodate for lattice mismatch between the substrate and ZnO, and thus minimize dislocation density.

Through this research several different substrate and oxidation combinations have been studied in sequence for ZnO growth. These are 30% H_2O_2-MBE of ZnO on GaN template [108], 50% H_2O_2-MBE of ZnO [109];[110];[111]:[112] and rf-plasma MBE of ZnO on (0001) Al_2O_3 with high temperature MgO buffer layer [113]:[114] using rf-MBE. This chapter concentrates on, 50% H_2O_2-MBE of ZnO and rf-plasma MBE of ZnO on (0001) Al_2O_3 with high temperature (HT) MgO buffer layer.

3.1. Buffer layer

The use of a buffer layer can significantly improve the quality of ZnO layers. It was recently shown that the deposition of a thin MgO buffer layer on the sapphire substrate significantly improves the ZnO overgrown [110]; [115]. Furthermore, annealing of the MgO buffer layer at high temperature improved the surface morphology and reduced the dislocation density [116]. It was shown that ZnO polarity can be controlled by the thickness of MgO, at deposition parameters which do not lead to the formation of spinel between Al_2O_3 and MgO [117]. Even implementation of low-temperature 30 nm ZnMgO buffer layer deposited at 280°C and subsequently annealed at 560°C was reported [118]. Recently, it was shown that ZnO deposited on (111) spinel suffers from inversion domains boundaries [119]. This means that spinel cannot control the polarity of the overgrown ZnO films. However, by using Mg modification of O-terminated $MgAl_2O_4$ (111) surface, one can eliminate the inversion domains and thus can, stabilize the polarity [120]. Nevertheless, the exact role of the MgO buffer layer was not systematically studied up to now.

3.2. Growth procedure

The growth of ZnO epilayers is carried out using a modified Varian Gen II MBE system described in section 2.1. 6N-purity Zn and 5N Mg elementals were evaporated using double zone effusion cells in order to reduce the oxidation of the source materials described in section 2.1.2. Either 50% H_2O_2 placed in a stainless-steel vessel in a stabilized temperature water bath or rf-plasma source were used as oxidant. 5N oxygen gas is injected into the RF-plasma source through a mass flow controller system. The oxygen RF-plasma source is kept at 400 W. The pressure in the chamber during the ZnO epitaxial growth was maintained at the level of 1×10^{-5} to 5×10^{-5} Torr by setting different H_2O_2 flows controlled by a leak valve, or by setting different O_2 gas flows controlled by MFC. Commercial Al_2O_3 (0001) substrates are used. Prior to the growth, a 1μm thick Ti film is deposited onto the back side of the substrates for more efficient absorption of infrared radiation from a substrate heater. The substrates were degreased in boiling acetone and iso-propanol for 10 minute and then dried with nitrogen jet. After this cleaning procedure the substrates were mounted on indium-free molybdenum holders and loaded into entry/exit chamber and baked at 250°C for at least 3 hours aiming to desorb water vapor and other impurities. After transferring the substrate into the growth chamber, it was thermally cleaned at 750°C in an ultra high vacuum at the pressure of 10^{-8} Torr for 60 min and treated in oxygen at 750°C for 30 min to produce an oxygen terminated c-sapphire surface. The substrate temperature (T_S) was measured using an infrared pyrometer calibrated at the Aluminum melting point and TS versus heater power dependence. After the thermal treatment the sapphire substrates show a sharp streaky RHEED pattern indicating a clean and flat surface.

The typical growth procedure was as follows:

First, a HT MgO buffer layer was grown on cleaned c-sapphire at 700°C with a slow growth rate of about 0.05 $Ås^{-1}$ under oxygen-rich conditions. After the deposition of about 2 nm thick MgO buffer, a low-temperature (LT) ZnO buffer layer was grown at 300°C at a growth rate of about 0.1 $Ås^{-1}$. After the growth of about 3 nm LT ZnO buffer, the RHEED patterns gradually changed from streaky to spotty. This indicates a roughening of the growth surface. The growth is stopped and annealing started at 700°C for about 5 min. Then a sharp streaky RHEED pattern of ZnO appears again. This procedure was repeated again at 400°C in order to produce a thicker ZnO buffer layer.

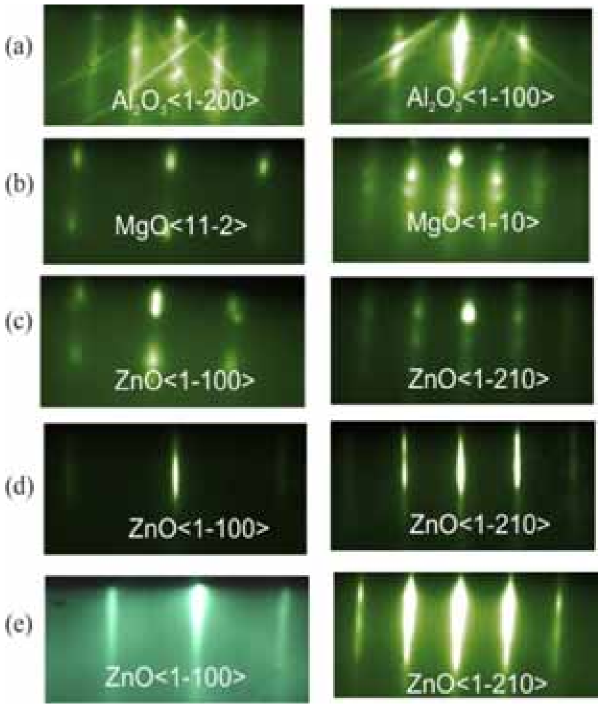

Figure 3.1: *RHEED patterns depicting the surface morphology evolution during the ZnO growth stages:*

a) Sapphire substrate after 20 min treatment in plasma at 700°C.
b) 2D nucleation of MgO buffer layer at 700°C.
c) Low temperature ZnO buffer layer growth at 300°C.
d) Low temperature ZnO buffer layer after annealing at 700°C for 5min.
e) Main ZnO epitaxial layer growth at 500°C.

RHEED was used for in-situ analysis of the surface morphology evolution during the buffer and ZnO growth stages. Figure3.1 shows the surface morphology evolution during the growth stages, beginning from the sapphire substrate (cf. Figure 3.1a). At the beginning of MgO deposition, a streaky pattern appears. Figure 3.1b indicates a 2D nucleation due to low interface energy between MgO and oxygen-terminated Al_2O_3 (0001). We proceed with LT ZnO buffer growth at 300°C on 2D MgO of about 2 nm thick. As the growth continues, RHEED pattern changes gradually to 3D after about 3 nm growth of LT ZnO buffer (Figure 3.1c). The growth is stopped and annealing started at 700°C for about 5 min, after which a sharp streaky RHEED pattern of ZnO appears Figure 3.1d. The growth of the main ZnO epilayer then started at 500°C with Zn beam flux around 0.3 nm/s and oxygen flow rate of 1.6 sccm under the plasma power of 400 W. After only a few nm ZnO growth, an intense RHEED specular spot appears and a (3x3) reconstruction pattern evolves (cf. Figure3.1e). These features hold till the end of growth.

3.3. Optimal growth conditions and growth kinetics

The growth temperature is one of the crucial parameters to achieve high quality ZnO films. According to the MBE technical principle discussed in section 1.2, several processes occur when molecules arrive at the substrate, including adsorption, migration on the substrate surface, interaction with other atoms, incorporation into the crystal, or desorption, all of which are affected by T_s. Only at high temperatures, the arriving Zn and O atoms have sufficient energy to move around on the surface and take their correct bonding positions. However, if the temperature is too high, these atoms may be re-evaporated from the surface, which leads to low growth rate. If the temperature is too low, these atoms cannot find the correct positions without high enough energy, which leads to high grow rate but poor crystal quality of the ZnO films. Therefore, the optimization of growth temperature is a key procedure to obtain high quality ZnO films. Another important parameter to control the ZnO growth is the O/Zn ratio. Under different conditions, MBE-growth of ZnO exhibits three distinct growth regimes as shown in Figure 3.2: O-rich (O/Zn>1), stoichiometric (O/Zn =1) and Zn-rich (O/Zn<1). When the Zn flux is kept constant during the growth, the O/Zn ratio varies with the active oxygen flux. The growth rate increases as the active oxygen flux rises under Zn-rich conditions and reaches the saturation under stoichiometric conditions. While further increasing in the active oxygen flux, lead to O-rich conditions. The O/Zn ratio influences the electrical, optical and other properties of ZnO films. High crystal quality ZnO was obtained under the stoichiometric flux condition together with the lowest dislocation density and the highest electron mobility compared to the ZnO films grown under nonstoichiometric flux conditions[110];[112].

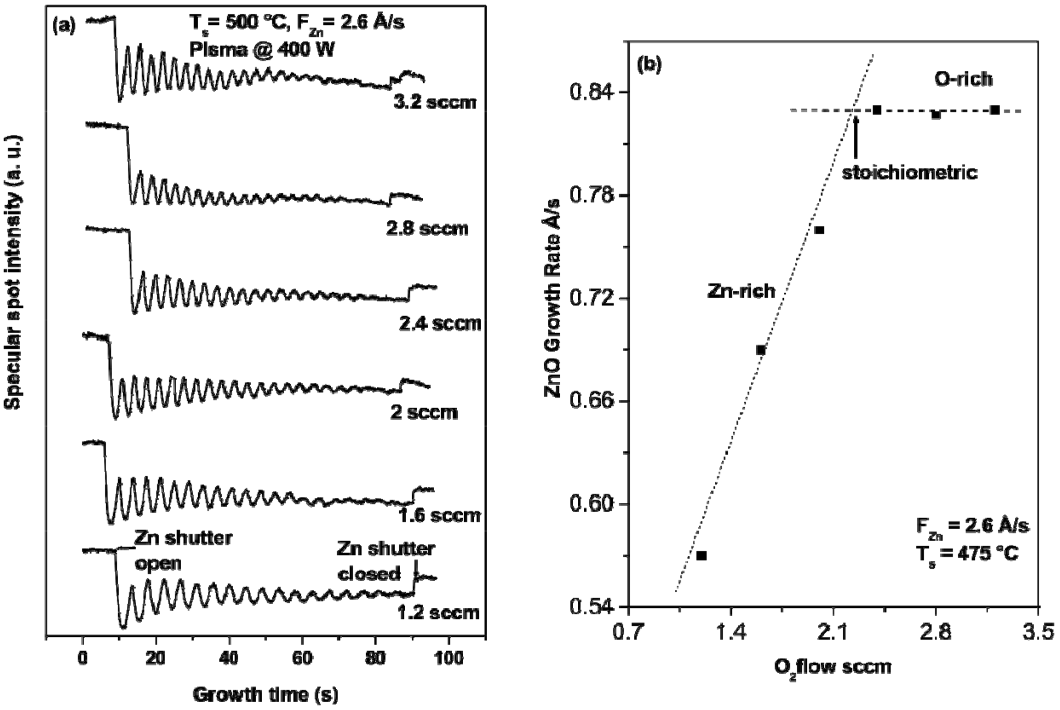

Figure 3.2: a) *RHEED intensity oscillations at* r_{Zn}*=2.6 Å/s,* T_s*=475 °C,* P_{rf}*=450W and different oxygen flow.*
b) ZnO growth rate at r_{Zn}*=2.6 Å/s,* T_s*=475 °C,* P_{rf}*=450W as a function of oxygen flow.*

As it was described in section2.1.3, the main difference between a conventional MBE and the one used in this research is the possibility to use two different oxidization sources H_2O_2 or rf-plasma to provide reactive oxygen. The growth procedures were the same in both cases. In the next two subsections, details of growth kinetics will be discuss and how one can achieve the optimal growth conditions of ZnO using either H_2O_2 or rf-plasma.

3.3.1 Using H_2O_2 as oxidant

The narrowing of the ZnO layer XRD rocking curve and roughness of the ZnO surface were used to optimiz the growth parameters and study the influence of growth parameters on the ZnO layer quality. Since structural defects in a wurtzite crystal, such as ZnO and GaN, manifest themselves in the tilt and twist angle and the average block size of microstructures in the epilayer, the broadening of an x-ray rocking curve can be used to assess film quality. The tilt is defined by the rotation of mosaic blocks out of the growth plane, which is caused by screw dislocations, while the twist caused by edge dislocations is defined by in-plane rotations. The tilt angle of a GaN epilayer was found to be linearly dependent on the full width at half maximum (FWHM) value of (0002) rocking curve [121]. The influence of growth temperature on the FWHM of the (0002) x-ray rocking curve was used in order to improve the ZnO layer quality. Figure 3.3 represents the FWHM (0002) diffraction peak in an XRD (0002) rocking curve which was obtained for the ZnO layers versus the growth temprature (T_s). These layers were grown at the same Zn rate (1.0 Ås^{-1}), which where monitored by quartz thickness monitor before the growth, and at the same H_2O_2 pressure ($3.5x10^{-5}$ Torr). One can deduce from this graph that, the quality of the ZnO layers becomes better as we increase the T_s till 500°C, where the best layers quality were obtained . Inset in Figure 3.3 is the XRD diffraction peak (0002) ω-rocking curve of the ZnO layers grown at 500°C, with extremely narrow value FWHM of 27 arcsec. The optimal growth temperature was 500°C. The FWHM increases again if the growth temperature is increased or decreased. Increasing the growth temperature causes Zn desorption from the surface and leads to oxygen-rich growth conditions.

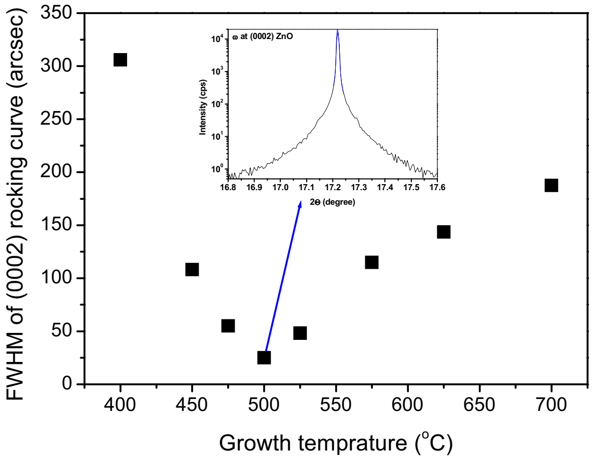

Figure3.3: *FWHM of (0002) XRD rocking curve for as-grown ZnO layers at different substrate temperature at the same Zn rate (1.0 Ås^{-1}), and at the same H_2O_2 pressure ($3.5x10^{-5}$)*

The influence of the Zn deposition rate variation from 0.6 Ås^{-1} to 4 Ås^{-1} on the FWHM of the (0002) ω-scan for the ZnO layers obtained is presented in Figure 3.4b. All the ZnO epilayers presented in this plot were grown at 500°C, and at a H_2O_2 pressure of 3.5×10^{-5} Torr. The FWHM values of X-ray ω-scan curves decrease with increasing Zn deposition rate up to 0.1nm/s, but it becomes larger for further increase in the Zn deposition rate. The dependence of the FWHM of the (0002) ω-scan of as-grown ZnO layers on the H_2O_2 pressure is depicted in Figure 3.4a, showing an optimal H_2O_2 pressure, a deviation from which leads to broadening of the FWHM, and hence, the worse ZnO crystal quality. From Figure3.4, one can conclude that the optimized growth parameters (at Ts=500°C) are at a Zn rate 1.0 Ås^{-1} and a H_2O_2 pressure of 3.5x10^{-5} Torr.

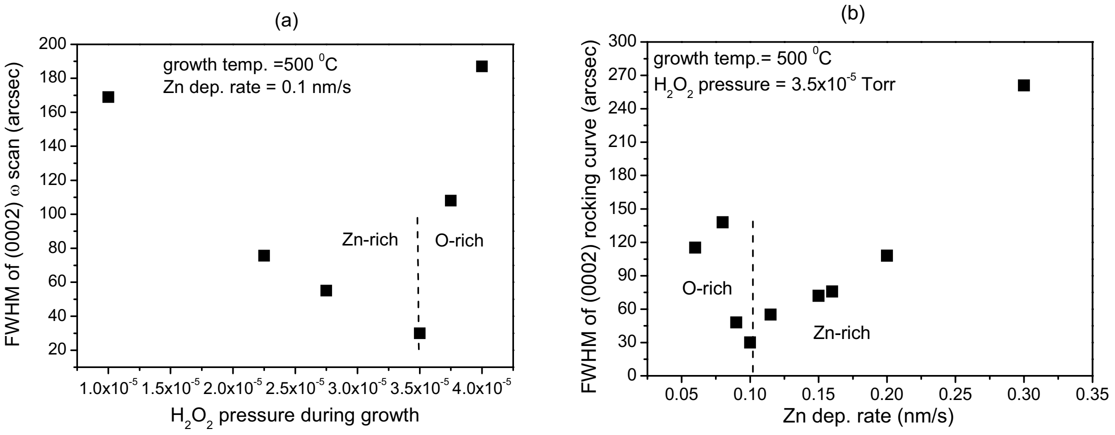

Figure 3.4: *a) The FWHM of (0002) ω-scan curves for ZnO layers grown at different H_2O_2 pressures.*
b) The FWHM of (0002) ω-scan curves for ZnO layers grown at different Zn deposition rates.

The broadening of the FWHM of the XRD rocking curve at low temperatures is caused by low surface diffusion and the 3D growth mode as shown by RHEED and AFM investigations. The increase of the surface roughness and respective broadening of the FWHM of the XRD rocking curve (cf. Figure 3.3) with increasing growth temperature above 500°C can be explained as follows: increasing the growth temperature causes Zn desorption from the surface and leads to oxygen-rich growth conditions. According to the investigations described above, as well as to our investigations of the dependence of the ZnO growth rate on the Zn deposition rate and H_2O_2 pressure, the optimal growth conditions were obtained in the case when the O/Zn ratio is about 1.0 with a slight oxygen excess. By employing the results of the investigations described above, we successfully grew high-quality ZnO layers on two-inch sapphire substrates in optimized conditions (growth temperature 500°C, Zn rate 1.0 Ås^{-1} and H_2O_2 flow related pressure in the growth chamber of 3.5x10^{-5} Torr).

3.3.2 Using plasma source as oxidant

H_2O_2-MBE is a cheap and efficient technique of the epitaxial growth of ZnO. It has been found that the growth rate was changing from run to run. Because the concentration of H_2O_2 changing to the lower concentration during the daily operation. The above problem stimulate the search for onther source for oxidizing species for the ZnO MBE, Oxygen plasma source seems to be a attractive alternative to the H_2O_2.

Typical growth initiation procedures like in the H_2O_2 case, includes growth of a HT MgO buffer layer at T_S=700°C. Thereafter, a LT ZnO buffer layer at 300° C, followed by annealing at 700°C under the activated oxygen flux for 5 min. This procedure was repeated at 400°C to produce a ~10-nm-thick ZnO buffer layer. Then, the main ZnO layer (250-700 nm) was grown at T_S=200-700°C, employing various O/Zn flux ratios for growth kinetic studies and optimization of growth conditions. After only a few nm ZnO growth, an intense RHEED specular spot appeared and a (3x3) reconstruction pattern sometimes evolved.

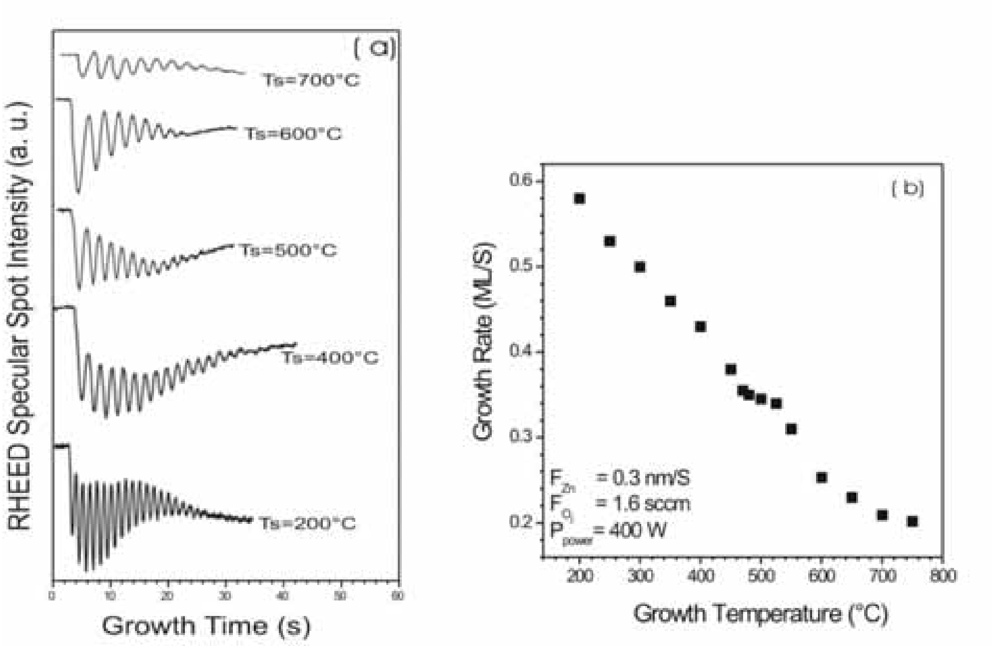

Figure 3.5: *a) RHEED specular spot intensity oscilllations on 00 rod on* $<1\bar{1}00>$ *azimuth at* $r_{Zn} = 4.5$ *Å/s,* $r_O = 2.4$ *sccm,* $P_{rf} = 400W$ *and different* T_S.
b) The temperature dependence of the growth rate in monolayer per second evaluated from the set of such RHEED oscillations.

Layer-by-layer growth of the main ZnO layer is proven by recording RHEED intensity oscillations. Figure 3.5(a) shows RHEED specular spot intensity oscillation with electron beam directed along the $<1\bar{2}10>$ ZnO azimuth at various T_S=200°C-700°C. At high T_S>500°C, the RHEED oscillations damp faster for two reasons: firstly, because of the strong decrease in the Zn incorporation coefficient (α_{Zn} [122]), which may lead to oxygen-rich 3D growth mode. Secondly, due to the change in the growth mode from 2D nucleation to a step-flow mode, since the RHEED specular spot becomes even sharper. At low T_S<400°C, the

RHEED oscillations degrade more rapidly due to surface roughening probably induced by the insufficient desorption of the excessive Zn from the growth surface, that is reflected in diffused RHEED patterns. Nevertheless, RHEED oscillations were recorded even at 200°C. The oscillations are most pronounced for Zn-rich growth, with the O/Zn ratio close to 1 at T_S=400°C-500°C. The ZnO growth rate (r_{ZnO}) as a function of T_S derived from RHEED oscillations is presented in Figure 3.5b. A nearly constant growth rate is observed between 450°C and 550°C as shown in Figure 3.5b. The kinks at the dependences correspond to change of the growth stoichiometry from O-rich (at high T_S) to Zn-rich (at low T_S), where the growth is governed by Zn and O incorporation, respectively.

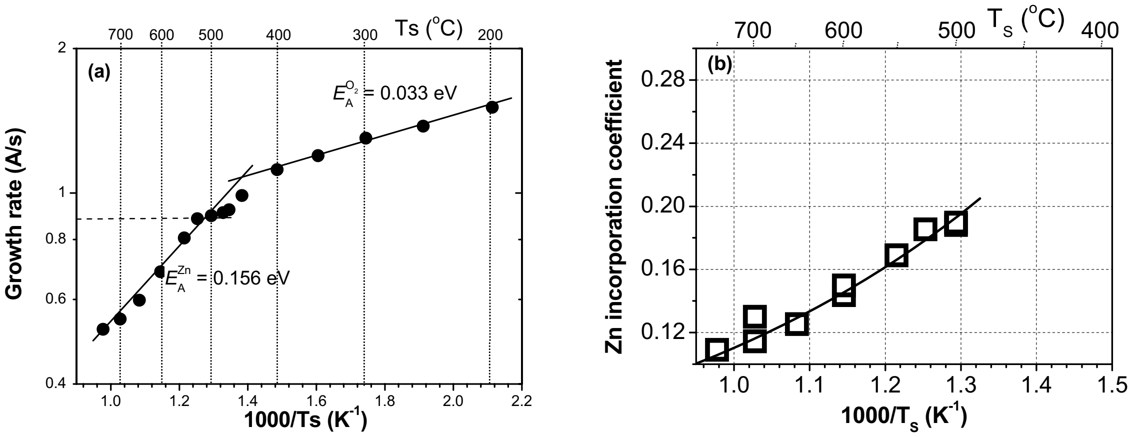

Figure 3.6: *a) ZnO growth rate as a function of TS for rZn=3 Å/s, rO=1.6 sccm, and Prf=400W. Horizontal dashed line shows the kink rZnO value.*

b) Absolute α_{Zn} values versus T_S, defined as $\alpha_{Zn}=r_{ZnO}(T)/r_{ZnO}(max)$, where r_{ZnO} (max) is recalculated from the Zn flux measured by a quartz monitor at room temperature.

The activation energies of the desorption for both regions agree well with previously reported data [122], being much larger for Zn. The kink r_{ZnO} values determine the activated O-flux supplied by the RF plasma source at T_S=500°C, 400W and a given O_2-flow rate. It equals 0.5±0.05 Ås^{-1} per sccm. Absolute α_{Zn} values versus T_S, defined as $\alpha_{Zn}=r_{ZnO}(T)/r_{ZnO}(max)$, where r_{ZnO}(max) is recalculated from the Zn flux measured by a quartz monitor, using Zn/ZnO molar mass and density ratios, are shown in Figure 3.6b. Extrapolation of the dependence to lower T_S gives α_{Zn} (300°C) ~ 0.5 which fits reasonably well to the value determined in a ZnSe MBE [124]. ZnO layers reveal strong variation of surface morphology versus growth conditions. In the case of growth at 400°C, AFM micrographs of the surface show islands with irregular and rough steps. A root mean square (rms) surface roughness of 5.0 nm was estimated (Figure 3.7a). When the growth temperature was increased to 500°C, the roughness decreased from 5.0 to 0.2 nm. A coalescence of the hexagonal islands is observed and the step edge becomes regular (Figure 3.7b). When the growth temperature was further increased to 700°C, the formation of hexagonal pits on an atomically flat surface with rms roughness of 0.45 nm was observed (cf. Figure 3.7c).

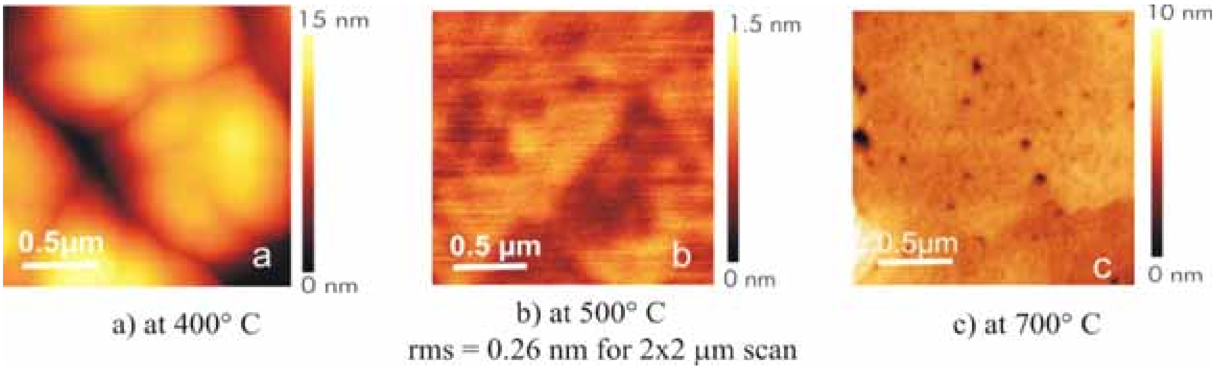

Figure 3.7: *AFM images of surfaces of ZnO layers grown at different temperatures: a) 400°C, b) 500°C, and c) 700°C*

These results show that the broadening of the FWHM of the XRD rocking curve (section 3.3.1) at low temperatures is caused by low surface diffusion and 3-dimensional growth mode. The increase of the surface roughness and respective broadening of the FWHM of the XRD rocking curve with increasing growth temperature above 500°C can be explained as follows: increasing the growth temperature causes Zn desorption from the surface and leads to oxygen-rich growth conditions.The optimal growth conditions were obtained when II/VI ratio is about 1.0 with a slight oxygen excess and growth temperature 500°C.

3.4. The role of high temperature MgO buffer

The significant role of the MgO buffer layer is evident by comparing a ZnO film about 540 nm thick deposited on (0001) Al_2O_3 substrate without MgO buffer layer, and a ZnO film of the same thickness deposited under the same conditions on (0001) Al_2O_3 substrate covered by a 2nm thick HT MgO buffer layer (700°C). Improvement of ZnO epilayers surface morphology is already obvious from RHEED data. Further evidence is shown in Figure 3.8, which compares AFM results of a ZnO epilayer grown without (Figure 3.8(a)) and with (Figure 3.8(b)) HT MgO buffer. The rms value of surface roughness is 40 nm and less than 0.5 nm for the epilayer grown without and with HT MgO buffer, respectively. Besides the roughness, the morphology implies different growth mode. For the sample grown without an MgO buffer (Figure 3.8(a)), faceted crystallites of close to hexagonal shape characterize the morphology. Boundaries can be observed between adjacent crystallites. Such a surface usually corresponds to the columnar growth. This was confirmed by RHEED as 3D growth mode. In the contrast, the surface of the sample grown with the MgO buffer is atomic flat (Figure 3.8(b)).

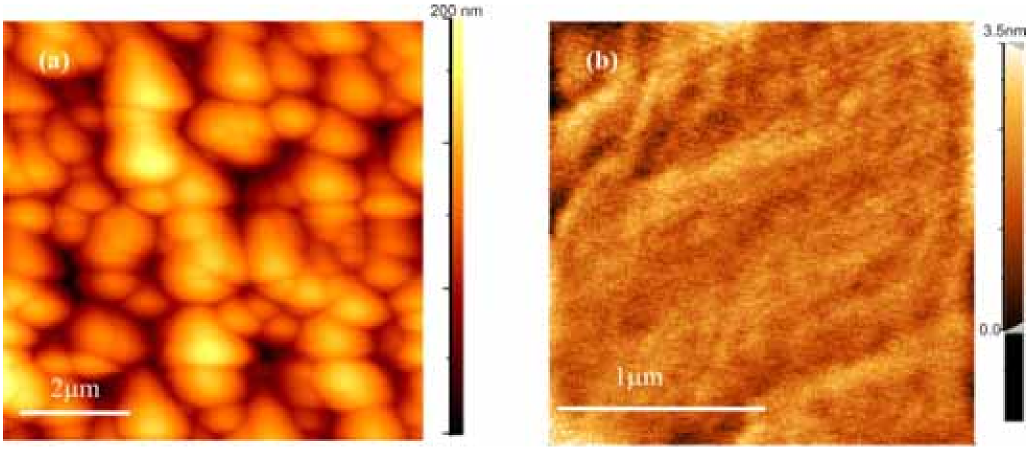

Figure3.8: *AFM images show 500 nm thick ZnO epilayers grown on sapphire substrates. (a) without and (b) with a HT MgO buffer layer. The rms value of roughness is (a) 40 nm and (b) less than 0.5 nm,* respectively.

The improvement in crystal quality of the ZnO film grown with a HT MgO buffer layer is assessed by HR-XRD.

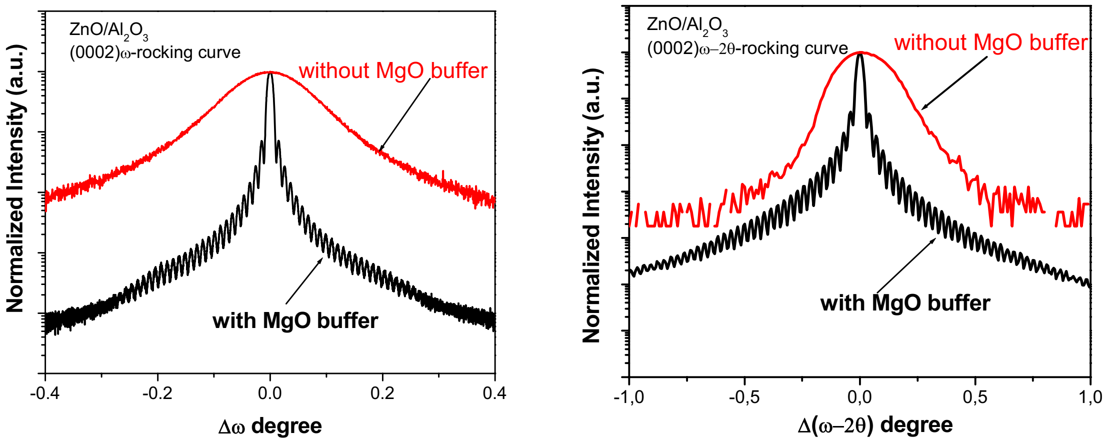

Figure 3.9: *XRD (0002) diffraction peaks of ω and ω -2θ scans of ZnO epilayers with and without HT MgO buffer. The intensity is plotted in logarithm scale in order to show the interference fringes clearly for film grown with HT MgO buffer.*

Figure 3.9 shows the HR-XRD ω-rocking and ω–2θ scans curves of the ZnO (0002) diffraction peaks. The presence of interference fringes in the ω, and ω–2θ scans for film grown with HT MgO buffer indicates a flat surface and sharp interface. The full width at half maximum (FWHM) of the (0002) rocking-curve gives an extremely narrow width of 25 arcseconds implying little tilt in the c-planes. These properties of the (0002) diffraction peak indicate the extreme ordering along the growth direction of ZnO (0001) as a consequence of well-controlled layer-by-layer.

Another indication of improvement in the crystalline quality is given by XTEM measurements. The XTEM measurments by Prof. J. Stoimenos, Aristotle University of Thessaloniki, Greece. The XTEM micrograph in Figure 3.10a shows the film deposited without HT MgO buffer layer. A high density of threading dislocations is evident; their density is estimated to be $5x10^{10}$ cm^{-2}. Figure10.b shows the ZnO film which was grown on the MgO buffer layer; the threading dislocations were reduced to $4x10^{9}$ cm^{-2}[125]], namely the dislocation density is one order of magnitude lower than without the HT MgO buffer. The HT MgO buffer layer cannot be resolved in Figure3.10b due to the low magnification.

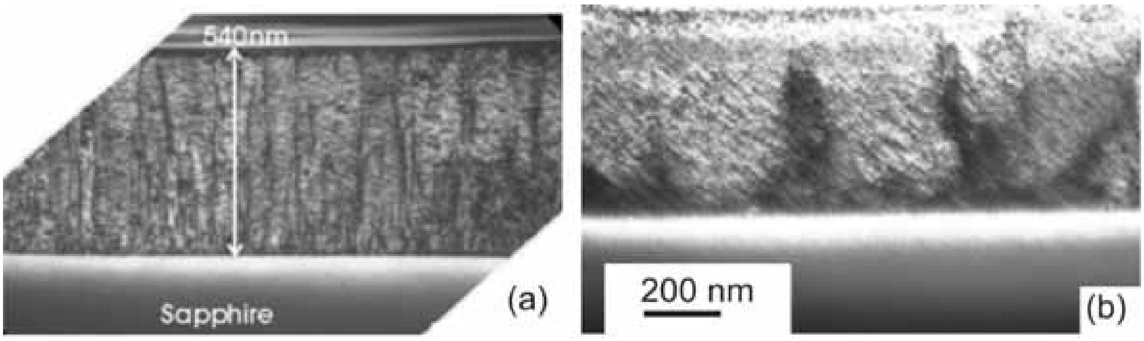

Figure3.10: *XTEM micrographs from ZnO films about 540nm thick. The micrographs were taken with the electron beam parallel to the* (1$\bar{1}$00) *crystallographic direction in respect of the sapphire substrate. a) From a film deposited without a MgO buffer layer. b) A ZnO film deposited under the same condition with a HT MgO buffer layer about 2 nm thick.*

As it was shown above, the quality of the ZnO films, epitaxially grown on sapphire, can be substantially improved by using HT MgO buffer layer. The formation of the MgO layer on the sapphire substrate and the reaction occurring with the MgO and Al_2O_3 substrate will systematically study by TEM in section 3.6.

3.5. Crystal quality of ZnO layers on (0001) sapphire

3.5.1. XRD investigations

High quality ZnO layers on 2-inch sapphire substrates were grown in optimized conditions by employing the results of the investigations described above. To characterize the structural quality of the grown films, ω–2θ scans were performed and the intensity of the diffracted x-rays plotted as a function of 2θ. From equation (2.8), if more than one (n=1, n=2 …) order diffraction peaks of only one crystal plane are available, then the crystal is oriented towards the direction perpendicular to this plane. In Figure 3.11, both the first (0002) and the second (0004) order diffraction peaks for the ZnO layers are clearly seen at 2θ = 34.57° and 72.61°. To verify these Bragg angles at the two reflexes, the distance d in equation (2.8) is calculated with θ = 17.28° and 36.35°. For each angle, d = 0.260 nm and this value corresponds to half the vertical lattice parameter C_0, i.e. the monolayer thickness of ZnO.

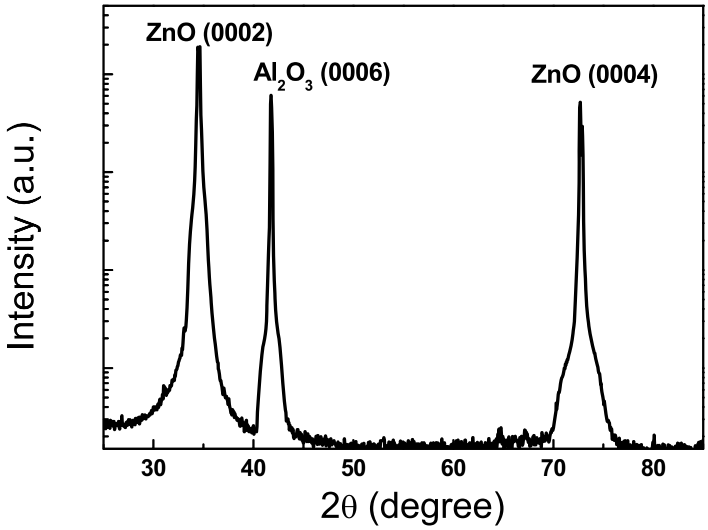

Figure 3.11: *XRD 2θ spectrum for ZnO layers grown on sapphire with HT MgO buffer. Both the (0002) and (0004) reflex peaks of ZnO are present.*

Figure3.12 shows a reciprocal space mapping of the (0002) diffraction of a ZnO epilayer with a thickness of 105 nm on sapphire substrate. The streak from top left to bottom right stems from the detector and will not be considered here. The dotted vertical streak stems from the ZnO film and corresponds to ω/2Θ scan in the growth direction. The dots are the maxima of the interference fringes due to the finite film thickness. They are symmetrically distributed around the ZnO Bragg maximum thus suggesting a uniform distribution of the lattice strain.

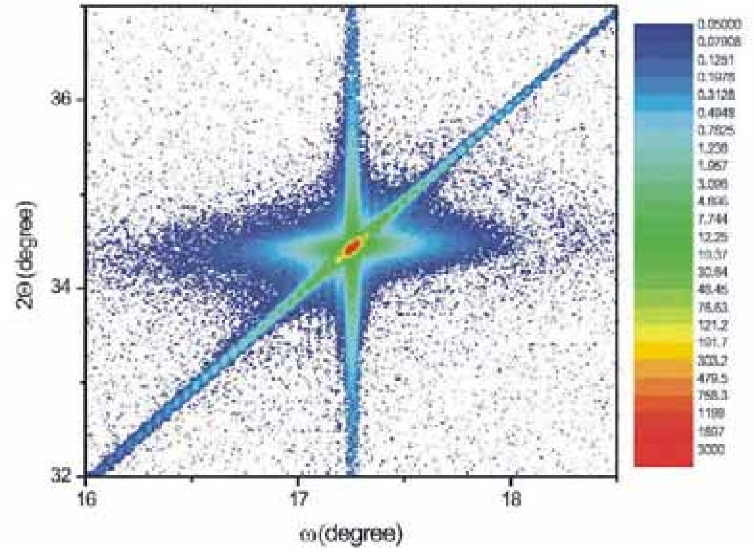

Figure 3.12: *(0002) reciprocal-space mapping of the ZnO layer grown on 2-inch sapphire substrate (XRD measurement by J. Bläsing, Uni Magdeburg)*

Figure 3.13a shows a (0002) ω–2θ rocking curve of 200 nm ZnO layer grown in optimized conditions on 2 inch sapphire substrate. The thickness fringes indicate excellent surface and interface flattnes. Figure3.13b shows a (0002) rocking curve mapping along 2 inch ZnO epiwafer. A high lateral homogeneity is clearly noticed.

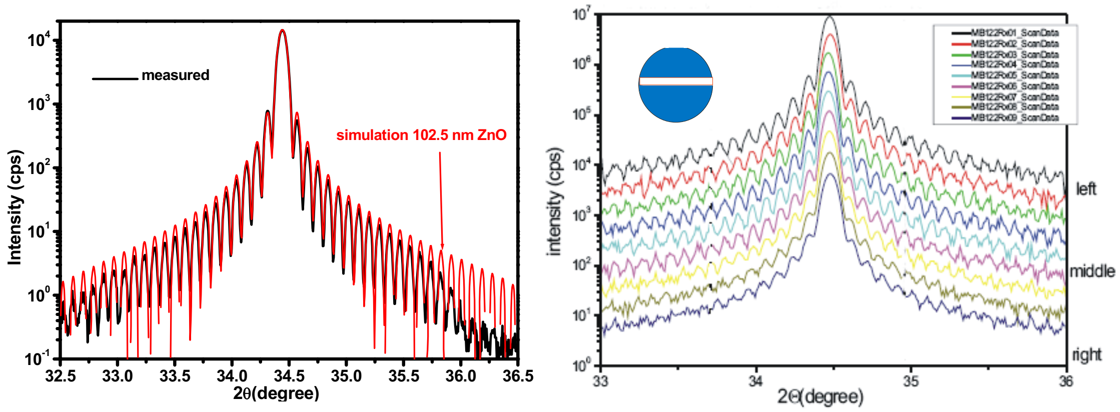

Figure 3.13: *a) (0002) ω–2θ rocking curve of 200 nm ZnO layer grown in optimized conditions. b) (0002) rocking curve mapping along a 2 inch ZnO epiwafer (XRD measurement by J. Bläsing, Uni Magdeburg)*

The profiles of ω–rocking scans across the ZnO (0002) and $(11\bar{1}0)$ reflections are illustrated in Figure 3.14. The full width at half maximum of the (0002) reflection, 0.007 degree, is much smaller than that of the $(11\bar{1}0)$ reflection, 0.27 degree revealing the micro-twist dominates the mosaicity, while micro-tilt is much less important. This pronounced difference of the rocking curve widths between the (0002) and $(11\bar{1}0)$ reflections strongly indicates that the density of pure edge threading dislocations is greater than that of pure screw dislocations. These observations are qualitatively similar to what was observed for GaN grown on c-plane sapphire [125]. The analogous phenomena are attributed to the similar crystal structures of ZnO and GaN, both belonging to space group $P6_3mc$, and the similar lateral lattice parameter, with a difference of ~1.8%.

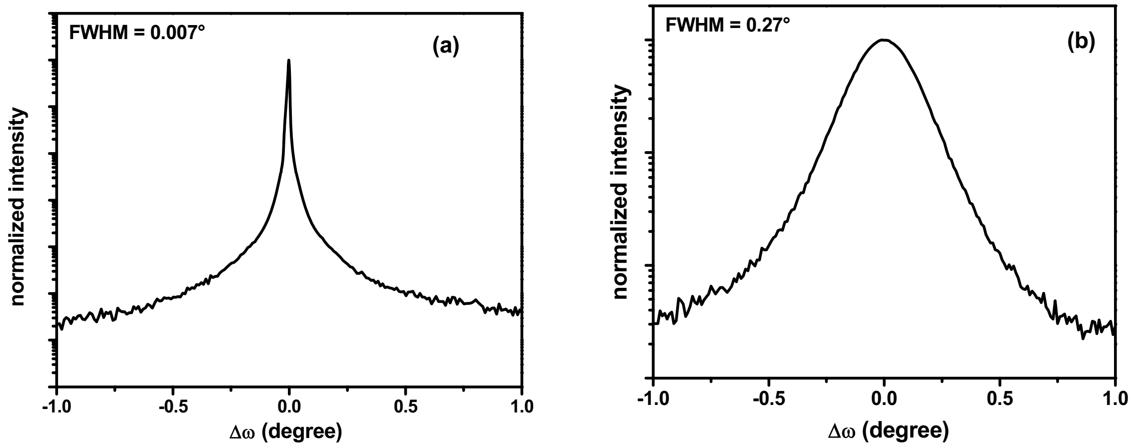

Figure 3.14: *ω–rocking scans across the ZnO (0002) (a) and $(10\bar{1}0)$ (b) reflections of 400 nm ZnO layer grown with HT MgO buffer. (XRD measurement by J. Bläsing, Uni Magdeburg)*

3.5.2. TEM investigations

The good crystal quality of the ZnO film was also confirmed by XTEM observations. As it was expected the selected area diffraction pattern (SADP) confirms the following epitaxial relation (0001) ZnO (0001) Al_2O_3 with $(11\bar{1}0)$ ZnO$\|(11\bar{2}0)$ Al_2O_3 The typical defects are threading dislocations as shown in Figure 3.15a. The thickness of this film was 300 nm. The threading dislocations were inhomogeneously distributed in areas exhibiting higher density in the order of 10^{10} cm^{-2}, as shown in Figure 3.15a, and in areas where the density was two orders of magnitude lower, as shown in Figure 3.15b. It is estimated that the mean value of the threading dislocation density was $4x10^9$ cm^{-2}

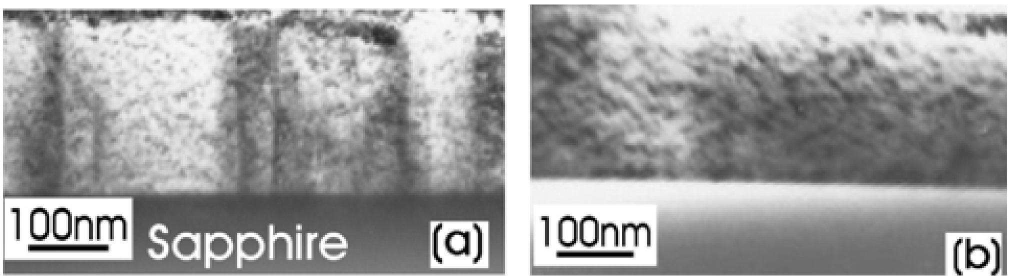

Figure 3.15: *XTEM micrographs from the ZnO film. The micrographs were taken with the electron beam parallel to the* $(11\bar{2}0)$ *axis of the ZnO film. (a) The main defects are threading dislocations inhomogeneously distributed in the film. In this area dislocation density is of the order* $1x10^{10}$ cm^{-2}*. (b) An adjacent area where the dislocation density is low of the order* $1x10^{8}cm^{-2}$ *reveals the non-homogeneous distribution of the dislocations.*

The structure of the Al_2O_3/MgO/ZnO interface was also studied by HR-XTEM microscopy in both $(10\bar{1}0)$ and $(11\bar{2}0)$ sections with respect to the Al_2O_3 lattice. The HRTEM measurements were done by B. Pecz, Hungarian Academy of Sciences. The HRTEM micrograph in the $(10\bar{1}0)$ section is shown in Figure3.16.

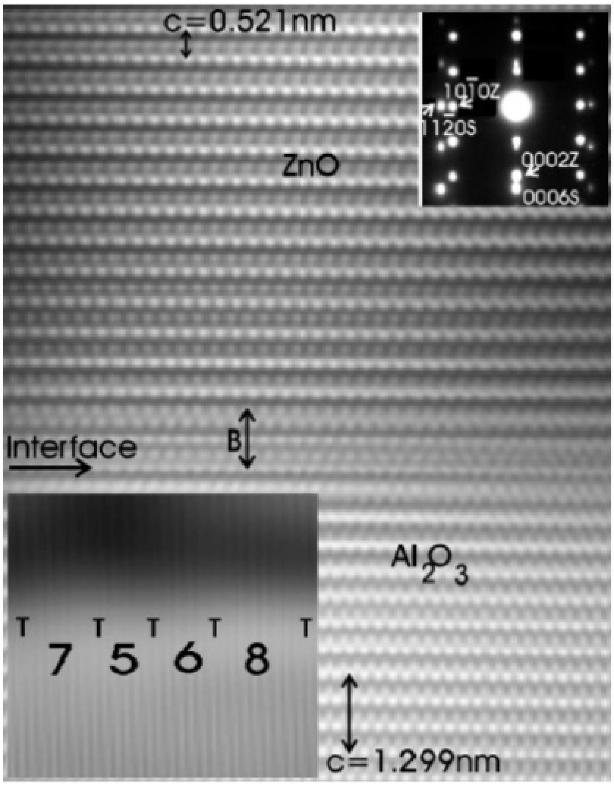

Figure 3.16: *HR-XTEM micrograph from the interface. The electron beam was parallel to the* $(10\bar{1}0)$ *direction with respect to the* Al_2O_3 *substrate. The corresponding diffraction pattern is shown in the inset of the figure at the upper right corner. Only the lattices of the* Al_2O_3 *and ZnO can be distinguished by exhibiting the hexagonal symmetry. The expected MgO 2 nm thick buffer layer at the interface is denoted by B. The Fourier-filtered image at the interface is shown in the inset. The* $(10\bar{1}0)$ *ZnO and* $(11\bar{2}0)$ Al_2O_3 *lattice planes are shown, respectively. The misfit dislocations at the interface are denoted by T.*

The corresponding diffraction pattern is shown in the inset of the figure. Surprisingly only the lattices of the Al_2O_3 and ZnO can be distinguished. The region of the expected 2 nm thick MgO buffer layer at the interface is denoted by B in Figure3.16; however, only the ZnO structure is evident in this zone. The same configuration is observed in the $(11\bar{2}0)$ section, as shown in Figure3.17a. The expected 2 nm thick MgO buffer layer at the interface is also denoted by B.

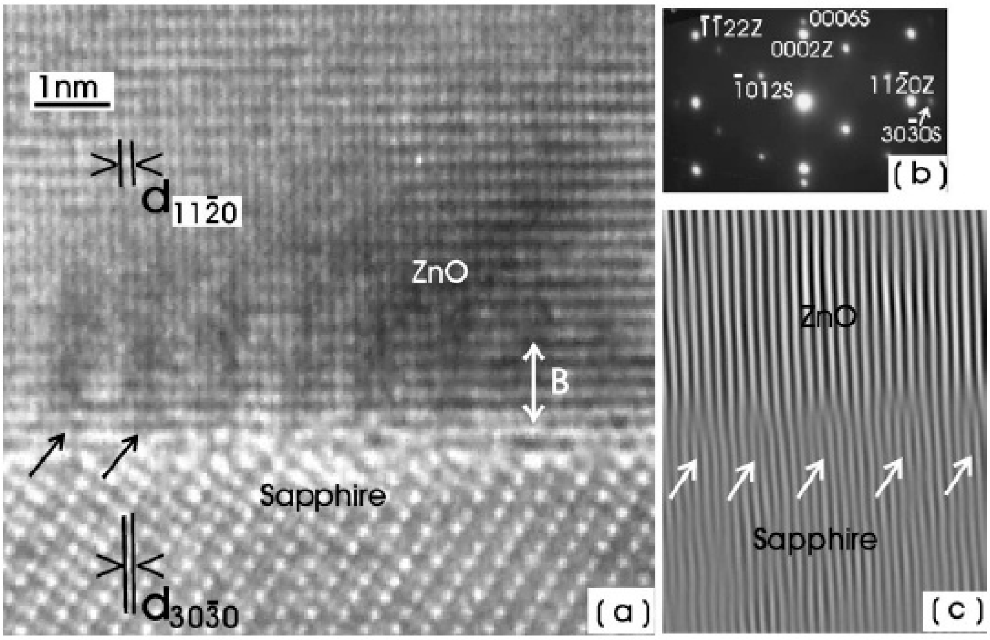

Figure 3.17: *HR-XTEM micrograph from the interface. The electron beam was parallel to the $(11\bar{2}0)$ direction with respect to the Al_2O_3 substrate. (a) Only the ZnO structure is evident up to the Al_2O_3 interface. The expected MgO 2 nm thick buffer layer is denoted by B. (b) The related diffraction pattern from the interface. (c) Fourier-filtered image from the interface using the $(11\bar{2}0)$ ZnO and the $(30\bar{3}0)$ Al_2O_3 reflections. The extra lattice planes are denoted by arrows.*

The related diffraction pattern from the interface is shown in Figure 3.17b. Only the ZnO $(11\bar{2}0)$ and (0002) lattice planes are observed in zone B. All the misfit dislocations are well confined at the ZnO/Al_2O_3 interface, as the Fourier-filtered image reveals in Figure3.17c, using the $(11\bar{2}0)$ and the $(30\bar{3}0)$ reflections for ZnO and sapphire, respectively. A missing ZnO plane after every six to seven planes is evident. Namely, every seventh or sixth $(30\bar{3}0)$ plane of sapphire terminates at the interface matching with six or five $(11\bar{2}0)$ planes of ZnO. The same is observed in the Fourier- filtered image of the $(11\bar{2}0)$ ZnO section, as shown in the inset in Figure3.16. In this case misfit dislocations appear every five to eigth planes of Al_2O_3 that corresponds to four to seven lattice planes in ZnO. This configuration facilitates the better matching of the two lattices, characterized as domain matching epitaxy (DME), where integral multiples of lattice constants match across the interface. In each domain the residual strain depends on the ratio m_s/m_z according to:

$$\epsilon_r = \frac{m_z d_z - m_s d_s}{m_z d_z} \tag{3.1}$$

Where m_z and m_s are the number of the lattice planes for the ZnO and Al_2O_3 in the domain. For a ratio $m_s/m_z=6/5$ and taking into account that the d spacing for the $(30\bar{3}0)$ and the $(11\bar{2}0)$ lattice planes of Sapphire and ZnO are $d_s= 0.13737$nm and $d_z= 0.16247$nm, respectively. The equation (3.1) gives residual negative misfit $\varepsilon_r=-0.013899$, namely in this domain the overgrown is under a small compressive strain. In the adjacent domains with lattice planes ratio 7/6, the equation (3.1) gives a positive residual misfit $\varepsilon_r=0.014275$. Therefore the total residual misfit in these adjacent domains is reduced to $\varepsilon_r=0.00037$. According to this interpretation it is evident that almost all the misfit is absorbed at the ZnO/Al_2O_3 interface.

The possibility that MgO buffer layer is pseudomorphic was also considered,[127]. The misfit between MgO and Al_2O_3 is high, more than 7%. Therefore the elastic interaction between the misfit dislocations, which will be very close, must be taken into account according to equilibrium theory for strained layer relaxation [20]. According to the new approach in a system with large misfit the critical thickness for the formation of a pseudomorphic zone is significantly higher. The formation of a new misfit dislocation has to overcome the resistance caused by the superposed self-stress field of the already existing misfit dislocations. Thus, the critical thickness h_c is higher, given by the relation:

$$h_c = \left(\frac{b cos\lambda}{2f}\right)\left\{1 + \left[\frac{1-\left(\frac{\nu}{4}\right)}{4\pi(1+\nu)\cos^2\lambda}\right]\right\}\ln\left(\frac{h}{b}\right) \tag{3.2}$$

where f is the misfit, b is the Burgers vector, v is the Poisson ratio and λ is the angle between the Burgers vector and the direction in the interface normal to the dislocation line [127]. The misfit f for the system $<1\bar{1}0>$MgO//$<1\bar{1}00>Al_2O_3$ is $f = 0.078$ or 7.8%. The misfit dislocation are **b**=a/2<110> of the 60^o type, b=0.9719 nm. Therefore from equation (3.2) the critical thickness h_c was calculated, considering that $\lambda=60^o$ and $\nu=0.3$. Thus, the critical thickness is estimated to be 0.31nm, namely about 1/3 of the deposited MgO buffer layer. Therefore a relaxed MgO layer should exists as was confirmed by RHEED in Figure3.1b.

A plausible explanation for this discrepancy between the TEM and RHEED observations is to consider the modification of the Al_2O_3 substrate by the deposited MgO buffer layer. Also interdiffusion between Zn and Mg during the deposition and annealing time of the ZnO is possible. Indeed the thermodynamic solubility limit of MgO in ZnO (for thermodynamic equilibrium) was reported to be 4 mol% of MgO, namely the formation of the $Mg_xZn_{1-x}O$ compound with x=0.04 is stable [128]. Moreover single crystalline $Mg_xZn_{1-x}O$ films having the wurtzite structure were deposited on Sapphire by laser ablation with Mg contain up to x=0.33[129]. The supersaturated $Mg_xZn_{1-x}O$ films are stable at low temperatures, for example a $Mg_xZn_{1-x}O$ film with x=0.22 can be stable below 700°C. Above this temperature partial separation of phases, with the formation of MgO precipitates in a $Mg_xZn_{1-x}O$ matrix with x=0.15 is observed. It is worth noticing that the $Mg_xZn_{1-x}O$ compound with x=0.15 is stable at least up to 1000°C [129]. Interdiffusion in $Mg_xZn_{1-x}O$/ZnO heterointerphases is also observed, which starts above 700 °C [23]. Therefore the formation of $Mg_xZn_{1-x}O$ alloy with a very small Mg content during the ZnO deposition, also during the annealing of the ZnO buffer layer at 750°C is expected. It is considered that the complete mixing of Mg and Zn in the 300nm thick film, shown in Figure 3.15 gives $Mg_xZn_{1-x}O$ alloy with x=0.033, which is below the solubility limit.

3.6. Formation of spinel at Al_2O_3/MgO hetero-interface

In section 3.4, it was shown the effect of thin HT MgO on ZnO heteroepitaxy by improving the surface morphology and crystal quality of the grown epilayers. In this section, The HT MgO buffer effects and its associated mechanisms are to be discussed from the view point of structural properties at the hetero-interface [131]. For the better understanding of the beneficial role of the MgO buffer layer a rather thick HT MgO layer, about 25 nm, was deposited on the (0001) Al_2O_3 substrate followed by a 70 nm thick ZnO layer, as shown in Figure3.18a. Due to the weak contrast the MgO layer is hardly resolvable in the bright field micrograph in Figure 3.18a. The MgO buffer is roughnand introduces significant roughness in the ZnO film. The corresponding diffraction pattern of the deposited layers in respect of the $(1\bar{1}00)$ section of the sapphire substrate is shown in Figure3.18b.

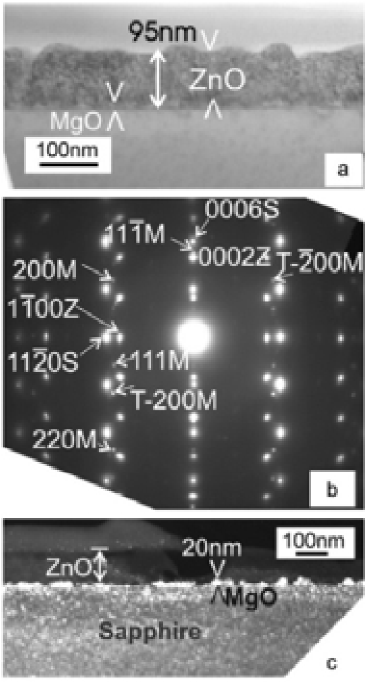

Figure 3.18: *A ZnO film grown on 25 nm thick MgO buffer layer. (a) Bright field (BF) XTEM micrograph with the electron beam parallel to* $[1\bar{1}00]$ *direction of sapphire. (b) The corresponding diffraction pattern. The diffraction spots, which belong to the sapphire are denoted by the letter S, those of ZnO by Z and the spots belonging to the MgO are denoted the letter M. (c) Dark field micrograph taken from the (200) MgO reflection*

Three sets of spots can be distinguished in this micrograph, spots attributed to the Al_2O_3 substrate, to the ZnO overgrown and spots corresponding to the (110) section of the MgO buffer layer. The diffraction spots, which belong to the sapphire are denoted by the letter S, those of ZnO by Z and finally the spots belonging to the MgO are denoted the letter M. The MgO buffer layer has the following epitaxial relation with the Al_2O_3 substrate $[1\bar{1}00]$ Al_2O_3//$[1\bar{1}0]$ MgO, and $[11\bar{2}0]$ Al_2O_3//$[11\bar{2}]$ MgO, also. [0001]Al_2O_3//[111] MgO. Twin spots were also observed, which are denoted by the letter **T** in Figure3.18b. The twin axis is the $[11\bar{1}]$, which is parallel to the c-axis of the sapphire substrate. Therefore the parent and twin spots have as common reflection the $(11\bar{1})$ one. The double positioning of the individual MgO grains produces twining, because the MgO nucleus have equal probability to be in epitaxial relation with the hexagonal substrate, in two equivalent positions which are rotated by 180° degrees. Figure 3.18c is a DF micrograph taken from the (200) MgO reflection, Due to twining not all the MgO grains are in contrast so that the 25nm thick MgO zone appears as discontinuous in Figure3.18c.

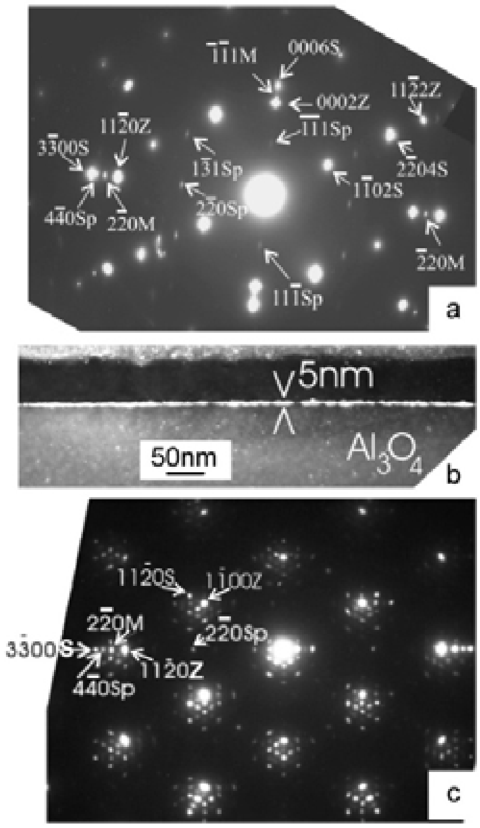

Figure 3.19: *The same film as in figure 3.10 seen on the $(11\bar{2}0)$ section in respect of sapphire. (a) The corresponding diffraction pattern. In addition of the expected spots of Al_2O_3, ZnO and MgO, also spots belonging to the spinel ($MgAl_2O_4$) were observed (denoted by letters SP). (b) This is a DF micrograph taken from the $(2\bar{2}0)$ spinel reflection. (c) PVTEM specimen, selected area diffraction pattern taken with the electron beam parallel to the [0001] direction of the sapphire substrate.*

Rotating the specimen for 30^o around the [0001] axis of the sapphire substrate we have taken the section $(11\bar{2}0)$, the corresponding sections for the MgO and the ZnO are the (112) and $(1\bar{1}00)$, respectively, as shown in Figure 3.19a. Surprisingly very weak extra reflections were also observed, these reflections were indexed and it was found that they belong to the spinel compound $MgOAl_2O_3$ (SG: $Fd\bar{3}m$, a=7.978 Å), which has cubic symmetry. The diffraction spots $2\bar{2}0$, $11\bar{1}$, $1\bar{3}1$ and $4\bar{4}0$ to the (112) section of the Spinel structure were identified, denoted by the letters Sp in Figure 3.19a. Figure 3.19b is a DF micrograph taken from the 220 spot of spinel, a 5nm thin layer in contact with the sapphire substrate is evident. The spinel layer is in epitaxial relation with the sapphire substrate having the following relation:

$[1\bar{1}00]_{sapphire}//[1\bar{1}10]_{spinel}$, and $[11\bar{2}0]_{sapphire}//[112]_{spinel}$, also $[0001]_{sapphire}//[11\bar{1}]_{spinel}$.

This was also confirmed by PVTEM observations after thinning the specimen from the backside. In the corresponding diffraction pattern, taken with the electron beam perpendicular to the sapphire basal plane, four groups of spots belonging to the sapphire, spinel, MgO and ZnO can be distinguished denoted by arrows in Figure 3.19c. In addition a high number of extra spots due to the double diffraction of the electron beam in the four superimposed layers are evident.

The overall view of the structure is shown in the high resolution XTEM (HRXTEM) micrograph in Figure 3.20a. The lattice planes of the intermediate spinel layer are resolved. The MgO hemispherical grains and the ZnO overgrown are also evident.

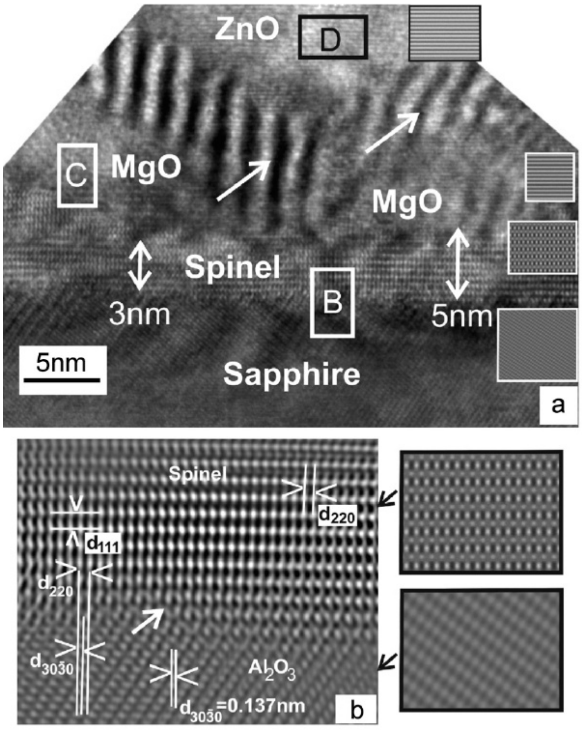

Figure3.20: *HRTEM micrographs taken with the electron beam parallel to the (11-20) axis in respect of sapphire. As framed insets HRTEM simulations of the Al2O3, MgAl2O4, MgO and ZnO structures along the projection direction are shown. (a) The overall view of the structure close to the sapphire interface is shown. The lattice planes of the spinel layer are evident. Due to the hemispherical shape of the MgO grains the MgO and ZnO lattices are superimposed giving moire patterns, which are denoted by arrows. (b) Fourier-filtered lattice images taken from the spinel/sapphire interface from the area denoted by the letter (B) in (a).*

Due to the hemispherical shape of the MgO grains the MgO and the ZnO lattices are superimposed giving moiré patterns, which are denoted by arrows in Figure3.20a.

Figure3.20b is the Fourier-filtered lattice images taken from the Spinel/Sapphire interface denoted by the letter (B) in Figure 3.20a, It is evident that one (220) lattice plane of the spinel phase corresponds to two $(30\overline{3}0)$ planes of sapphire. Therefore the misfit *f* between sapphire and spinel is given by the equation:

$$\mathrm{f} = \frac{\mathrm{d}_{220}^{\mathrm{spin}} - 2\mathrm{d}_{30\overline{3}0}^{\mathrm{sap}}}{2\mathrm{d}_{30\overline{3}0}^{\mathrm{sap}}} \qquad (3.3)$$

Where; $\mathrm{d}_{220}^{\mathrm{spin}}$= 0.2820 nm and $\mathrm{d}_{30\overline{3}0}^{\mathrm{sap}}$= 0.1374 nm. From equation (3.3) it is estimated that the misfit between sapphire and spinel is small, about 2.6%. This means that we will have one extra $(30\overline{3}0)$ lattice plane of sapphire in every 38 (440) lattice planes of spinel. Therefore the 18% misfit between ZnO and Al_2O_3 is progressively deviated between ZnO/MgO, MgO/Spinel and Spinel/Al_2O_3. The misfit between the MgO grains and the Spinel layer is about 5.6% while the maximum misfit, about 9.2%, exists at the ZnO/MgO interface. In order to relieve this misfit, misfit dislocations must be introduced. Thus, for every eleven $(11\overline{2}0)$ lattice planes of ZnO an extra (220) plane of MgO is expected. This periodicity of misfit dislocations is difficult to be resolved due to the overlapping of the ZnO and MgO lattice planes, because of the hemispherical shape of the MgO grains, resulting to the formation of moiré pattern, as shown in Figure3.20a. However measuring, for the same distance, the number of the lattice planes in the areas (C) for MgO and (D) for ZnO in Figure 3.20a, far from the interface, we found that 21 ZnO planes corresponds to 23 MgO lattice planes, the measured lattice plane ratio is 1.095, which is very close to the theoretical one, which is 1.092. Nevertheless the actual misfit between the (220) MgO and the $(11\overline{2}0)$ ZnO lattice plane can be calculated from the periodicity of the moiré patterns, which are of the displacement type. Thus, the periodicity of the moiré patterns when all the misfit is taken by misfit dislocation at the interface is given by the equation: [132],

$$\mathrm{D} = \frac{\left(\mathrm{d}_{11\overline{2}0}^{\mathrm{ZnO}}\right)\cdot\left(\mathrm{d}_{220}^{\mathrm{MgO}}\right)}{\left(\mathrm{d}_{11\overline{2}0}^{\mathrm{ZnO}}\right)-\left(\mathrm{d}_{220}^{\mathrm{MgO}}\right)} \qquad (3.4)$$

Considering that for undistorted ZnO and MgO lattices are $d_{11\overline{2}0}^{ZnO}$=0.162525 nm and d_{220}^{MgO}=14887 nm, respectively the equation (3.4) gives the theoretical value for the periodicity of the moiré pattern D= 1.772 nm. This value is very close to the measured one, from Figure3.20a, which was found to be $\mathrm{M}_{\mathrm{easured}}$=1.769nm confirming that almost the entire misfit is relieved by misfit dislocations.

The HRTEM simulated images of the atomic models are also included in the insets of Figure 3.20a and b, which were generated using the multislice algorithm of the EMS software [133].

The experimental conditions of thickness and defocus were defined by calculating the map of through focus thickness images of the perfect crystals along the experimentally determined orientations. For the simulated images perfect crystals with the observed epitaxial relationship are considered. For the particular imaging conditions atomic columns are projected onto white spots (defocus from 120 to 130 nm, thickness from 2 to 5 nm). It is evident that the simulated images are in agreement with the experimental one.

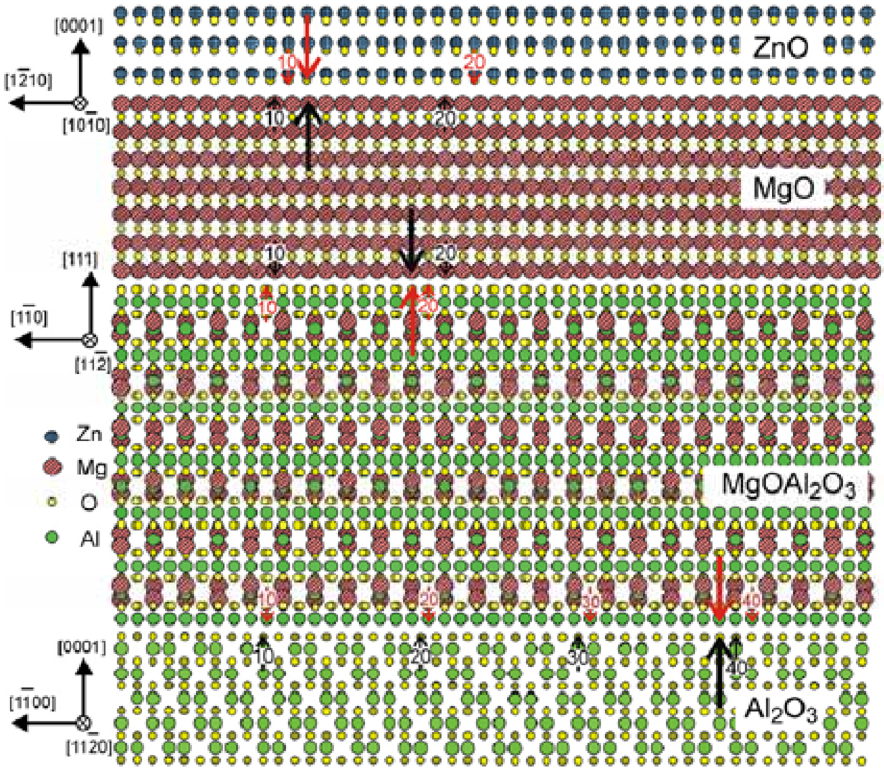

Figure 3.21: *Atomic configuration of the observed epitaxial relationships: [11$\bar{2}$0]Al_2O_3//[112]MgA12O4//[112]MgO//[10$\bar{1}$0]ZnO The misfit between the layers are 2.6%, 5.6% and 9.2%, respectively. At each interface the lattice planes of the joined crystals are numbered by small arrows and the coincident planes are specified by big arrows. Shading of atoms denotes different levels along the projection direction.*

In figurue 3.21, the observed epitaxial relationship:

[11$\bar{2}$0]Al_2O_3//[112]MgA12O4//[112]MgO//[10$\bar{1}$0]ZnO is depicted by atomic models. At the interfaces, the lattice planes of the joined crystals are numbered by small arrows and the coincident planes are specified by big arrows. Shading of atoms denotes different levels along the projection direction. The stacking sequence of atoms of the spinel structure along the [111] direction, is –O–Al–O–Mg–Al–Mg–O– where the O atoms form a face-centered-cubic sublattice with the Al and Mg atoms occupying half of the octahedral and one-eighth of the tetrahedral sites, respectively. The misfit between the layers leads to one extra [30$\bar{3}$0] lattice plane of Al_2O_3 in every 38 (440) lattice planes of $MgAl_2O_4$, one extra (440) lattice plane of $MgAl_2O_4$ in every 18 (220) lattice planes of MgO, and one extra (220) lattice plane of MgO in every 11 [11$\bar{2}$0] lattice planes of ZnO. The deposited layers are joined (and the lattices matched) following the experimental calculated lattice constants so that the actual misfit is revealed

Formation of spinel during the early stage of growth:

In order to understand the role of the spinel layer, we had to know if this layer is formed during the MgO deposition or it is formed later during the deposition of the thicker ZnO film, which requires more time. For this reason MgO layer, 20 nm thick, was deposited on sapphire under the same conditions applied for the growth of the MgO buffer layer. The 25nm thick deposited layer is shown in the DF-XTEM micrograph in Figure3.22a taken from the $2\bar{2}0$ diffraction spot of MgO. The island growth of the MgO is evident in this figure. Since the $2\bar{2}0$ spot of MgO and the $4\bar{4}0$ of spinel are very close, the two layers cannot be distinguished. A spinel layer, 5nm thick, in contact with the sapphire substrate is evident in the DF micrograph taken from the $(1\bar{3}1)$ spot in Figure 3.22b. This reflection is the strongest in the spinel structure. The corresponding diffraction pattern in section $(11\bar{2}0)$, in respect of sapphire, is shown in Figure 3.22c; the very weak spinel spots are denoted by arrows. This means that during the deposition of the MgO, interdiffusion of Mg and Al occurs, forming a thin spinel layer. This is consistent with other publications, which have shown that under similar conditions a 2.5nm thick spinel layer is formed even at 580°C [132].

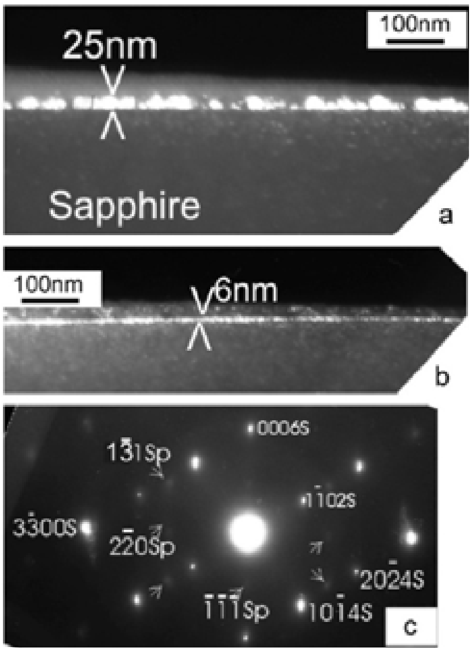

Figure 3.22: *XTEM micrographs taken from a thick MgO layer epitaxially deposited on sapphire. (a) DF micrograph taken from the MgO spot. (b) DF micrograph taken from the (131) spot of spinel. (c) The corresponding selected area diffraction patterns taken in the (110) section in respect of the sapphire substrate, the faint spinel spots are denoted by arrows.*

Therefore, the formation of the intermediate spinel layer in epitaxial relation with the sapphire substrate and the MgO overgrown is consequence of a solid-state reaction, where Mg^{2+} and Al^{3+} cations counter diffuse through the rigid oxygen sub-lattice [134].The spinel is grown by a slight shift in the oxygen positions, which change their hexagonal stacking in sapphire,

…ABAB… to the cubic …ABCABC… stacking sequence in spinel [135]. In this case the interstitial Al^{3+} ions crossing the interface neither create nor destroy lattice sites. During the formation of the spinel at both MgO/spinel and spinel/Al_2O_3 interfaces for the charge balance three Mg^{2+} ions diffuse inward for every two Al^{3+} ions diffusing outward. Therefore, for every spinel molecules forming at the MgO/$MgAl_2O_4$ interface three spinel molecules form at the Al_2O_3/$MgAl_2O_4$ interface [136], resulting to the faster growth of the spinel at the sapphire side. Marker experiments reveal that the $MgAl_2O_4$ film is formed in a ratio of 1:3 inside MgO and sapphire [138].

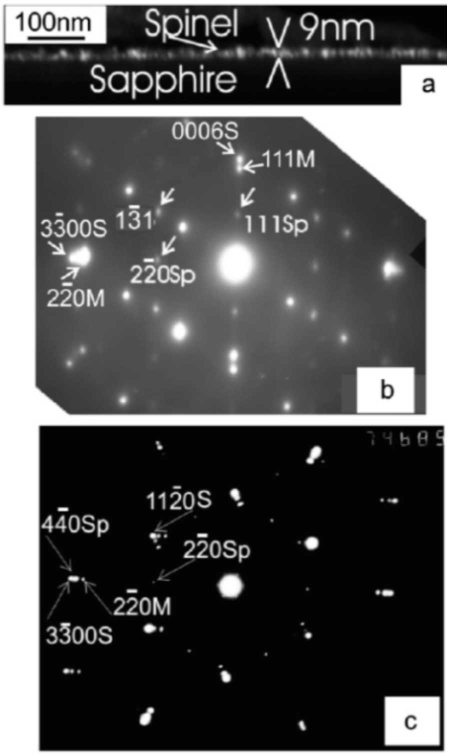

Figure 3.23: *The same MgO specimen as in figure3.13 after annealing at 1000°C for 30 min.*

a) DF micrograph from the spinel layer taken from the (131) spinel spot. The spinel layer was extended to 9 nm.
b) The corresponding diffraction pattern in respect of the (11$\bar{2}$0) section of sapphire. The spinel spots are now intense and sharp.
c) PVTEM specimen, selected area diffraction pattern taken with the electron beam parallel to the [0001] direction of the sapphire substrate.

The same specimen was subsequently annealed at 1000°C for 30 min. As a result the spinel layer was extended to 9 nm as shown in the DF micrograph in Figure 3.23a, which was taken from the (1$\bar{3}$1) spinel spot, as shown in Figure 3.23b. Also the diffraction spots belonging to it became sharper and more intense. The very sharp spinel diffraction spots are also evident in the PVTEM selected area diffraction pattern in figure 3.23c taken with the electron beam normal to the sapphire basal plane. In this case the specimen was thinned from the backside. These results reveal that the intermediate spinel layer is very stable and appropriate for high-temperature process.The formation of the cubic intermediate spinel layer not only reduces the misfit in the ZnO/Al_2O_3 system, but also can be used as a good quality cubic substrate for the epitaxial deposition of other compounds on sapphire. Annealing experiments reveal that as soon as the spinel layer is formed at about 700°C, it remains stable at least up to 1000°C.

3.7. Optical quality of ZnO layers on (0001) sapphire

In order to make high-performance optoelectronic devices on the base of ZnO, it is necessary to investigate the optical properties and transitions processes in ZnO. There are a lot of experimental techniques for the study of the optical transitions processes in ZnO, such as optical absorption, transmission, reflection, spectroscopic, ellipsometry, PL, CL, and PLexcitation (PLE) etc. Photoluminescence data is often used to characterize ZnO, because it is an excellent emitter. The spectra are typically dominated by bound excitons in the range of 3.3595 to 3.3678 eV at low temperatures.

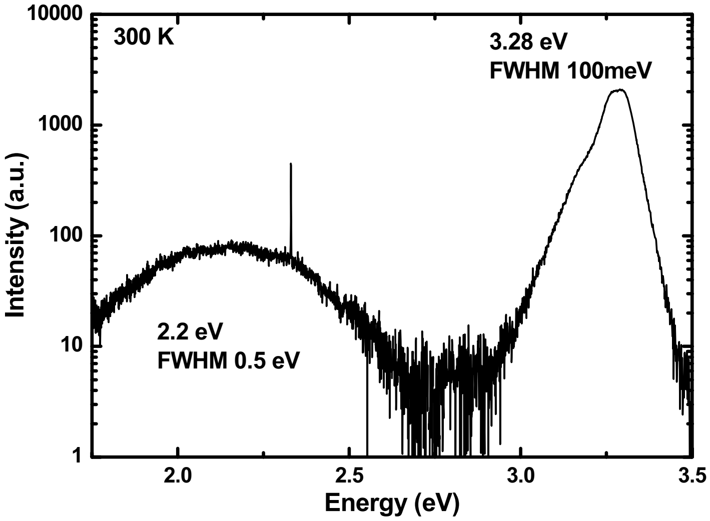

Firure3.24: *Room temperature PL spectrum of ZnO layers grown on (0001) sapphire with HT-MgO buffer. (Measurements by I.C. Robin, LETI, Grenoble, France)*

However, numerous authors [23]; [138];[139];[140] have accounted for these bound excitons in different ways leading to some confusion when assigning lines to a specific transition. Figure3.24 presents the room temperature spectrum of ZnO (0001) layer grown on sapphire with HT MgO buffer layer, obtained with a quadrupled pulsed YAG laser at 266 nm and an excitation density of about 30 W/cm2. This spectrum presents a peak centred at 3.28 eV due to the LO phonon replica of free excitonic transitions and a broad emission band probably due to oxygen vacancies.

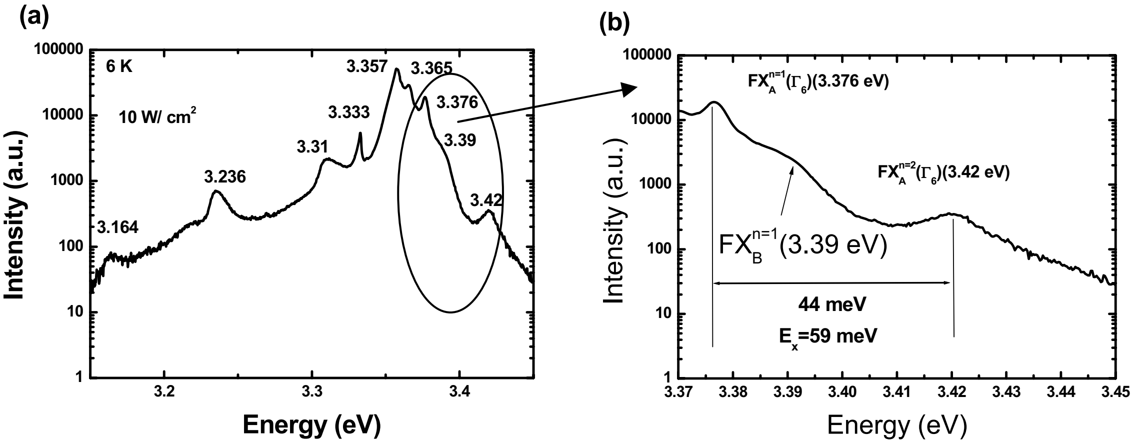

Firure3.25: *a) PL spectrum of the excitonic spectral region measured at 6K. b) Identification of the peaks in the free exciton region. (Measurements by I .C. Robin, LETI, Grenoble, France)*

For the PL temperature dependence we focused so far on the excitonic spectral region. Figure3.25 presents the low temperature PL spectrum for an excitation density of 10 W/cm^2. The transitions above 3.376 eV (Figure3.25 b) are attributed to free exciton emissions. The peaks at 3.376 and 3.42 eV are attributed to the ground state and the first excited state of the A exciton in the (Γ_6) band. The energy separation between those two emissions is equal to 3/4 of the exciton binding energy. From this separation (44 meV) we indeed determine an exciton binding energy of 59 meV. The emission at 3.39 eV could be due to the emission from the ground state of the B exciton. The transitions at 3.357 and 3.365 eV are attributed to neutral donors bound excitons (D^0X). The emission at 3.357 eV is probably due to the presence of Al impurities and the emission at 3.365 eV is due to other neutral or ionized donors. The emission at 3.333 eV is probably also of excitonic nature. It shows most of the established features of the Y-line recombination commonly observed in ZnSe and ZnTe and corresponds to excitons bound to structural defects. The emission at 3.31 and the emissions at 3.236 eV and 3.164 eV correspond to phonon replicas of the free exciton A. Note that the presence of those fine structures, especially the free exciton transitions indicates a high quality of the material with a low defect density.

Temperature dependence of PL spectra between 6K and room temperature every 30 K under the same excitation conditions (10 W/cm^2) was performed. Figure 3.26 presents normalized PL spectra measured between 6K and room temperature. The Y line disappears above 20 K because of the thermal activation [23].

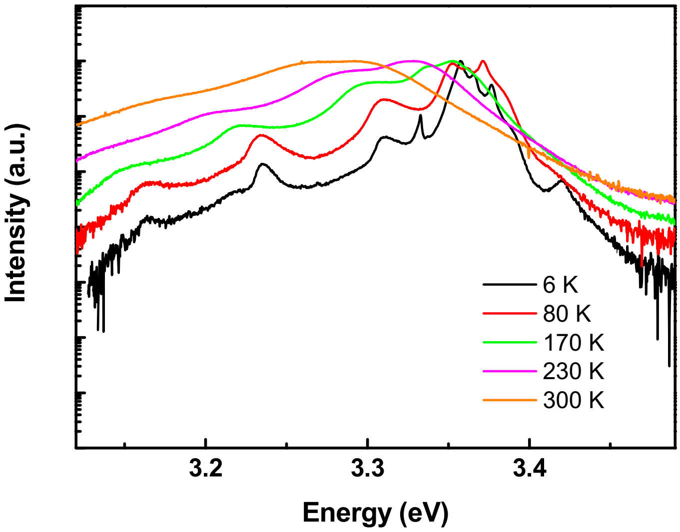

Firure3.26: *Normalized PL spectra measured between 6K and room temperature. (Measurements by I. C. Robin, LETI, Grenoble, France)*

The peaks broaden due to the coupling to the phonons. From 80K, the A free exciton F_{XA} n=1(Γ_6) transition becomes more intense than the D^0X lines. This corresponds to a delocalization of the bound excitons due to thermal activation.

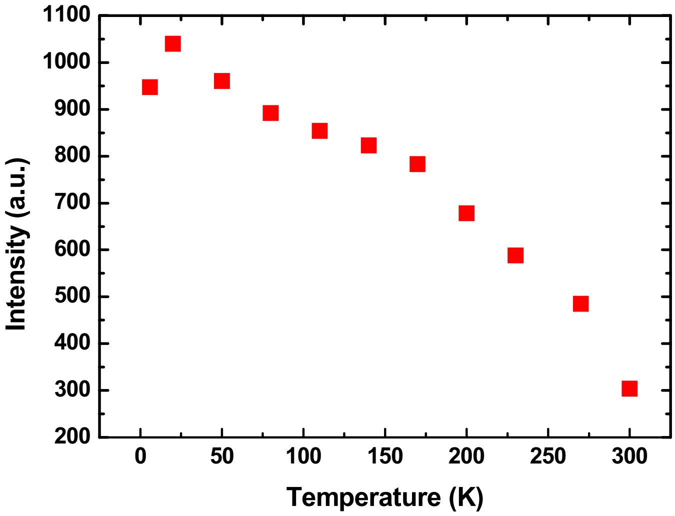

Firure3.27: *Evolution of the PL intensity between 6K and room temperature*

Figure3.27 presents the evolution of the PL integral intensity of the excitonic region between 6K and room temperature. It slowly decreases coming at 300K to about one third of the intensity at 6K. This corresponds to the activation of non-radiative channels in the capturing and recombination processes. However the non-radiative channels don't become dominant, even at room temperature (otherwise we would observe an exponential decay of the intensity).

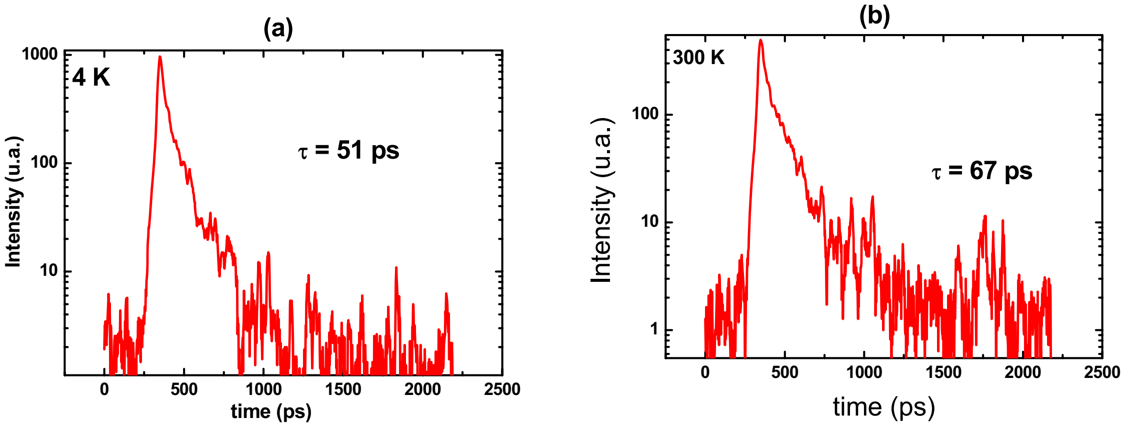

Firure3.28: *decay times measured on free exciton transitions at: a) 4 K and b) 300K (Measurements by I. C. Robin, LETI, Grenoble, France)*

To confirm this result, we also did decay time measurements using a tripled Ti: sapphire laser and a streak camera. Figure3.28 presents decay times measured on free exciton transitions at 6K and its first phonon replica at 300K. For a given temperature, the decay time is independent of the emission energy.The decay time measured at 4K is of the same order than the one measured at 300K. This confirms that the non radiative channels are not dominant up to 300K.

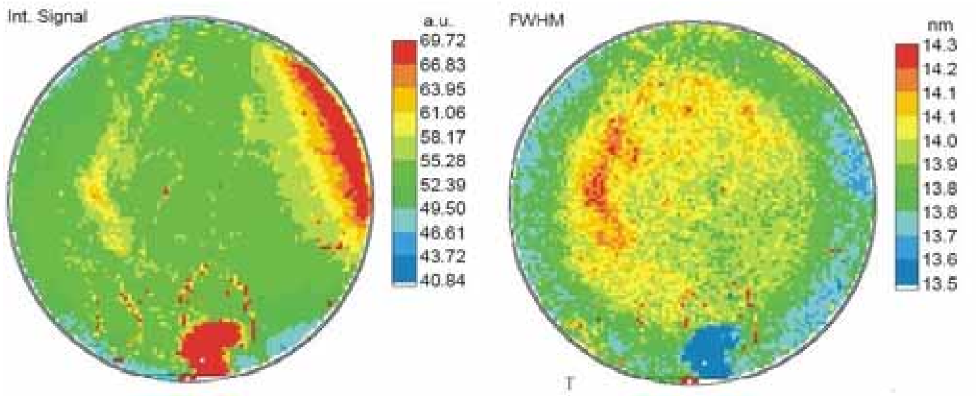

Firure 3.29: *PL mapping of 2 inch ZnO layers grown on (0001) sapphire with HT-MgO buffer: a) PL intensity mapping; b) PL FWHM mapping. (Measurements by M. Heuken, Aixtron AG).*

PL mapping of 2 inch ZnO epiwafer are presented in Figure 3.29. High lateral homogeneity of the epiwafer is clearly seen from both PL intensity distribution (cf. figure3.29a) and PL FWHM distribution (cf. figure3.29b).

3.8. Electrical properties of ZnO layers on (0001) sapphire

In this section electrical properties of ZnO layers on (0001) sapphire substrates grown at different growth parameters will be investigate. The target for the growth of these samples was to control and understand the electrical properties of the undoped ZnO layers as a first step to produce p-conductive ZnO layers and thus fabricate ZnO p-n homojunctions device for LEDs. ZnO is intrinsically n-type owing to donor defects such as oxygen vacancies and zinc interstitials (section 1.1.2). Hall-effect measurements and ECV measurements in this section were done by V. Petukhov, Institute of Semiconductor Technology, Braunschweig.

The effect of HT MgO layers on the electrical properties of ZnO layers grown on (0001) sapphire was investigated. For ZnO layers with thickness about 500nm grown with out HT MgO buffer on (0001) sapphire substrates the carrier concentration at room temperature was about 2.0×10^{18}cm^{-3} and hall mobility of 35 cm^2/Vs, while the samples grown with HT MgO layer and with the same thickness the carrier concentration at room temperature was about one order lower and electron hall mobility of 60 cm^2/Vs. These results agree well with the XRD and TEM results (see section 3.4) since the dislocation density is more than on order less in the ZnO layers grown with HT MgO buffer.

As it was discussed in the previous sections in this chapter, a high crystal quality with the lowest dislocation density of ZnO epilayers grown on (0001) sapphire was obtained under the stoichiometric flux condition compared to the ZnO films grown under nonstoichiometric flux conditions (section 3.5). So the electrical properties of ZnO epilayers are also responsible for O/Zn ratio as shown in Figure3.30. The influence of O/Zn ratio on the carrier concentration and hall mobility is presented in Figure 3.30a and Figure 3.30b respectively. All ZnO epilayers presented in these plots were grown at the same growth condition except the O/Zn ratio parameter. With increasing the O/Zn ratio from Zn-rich condition to stoichiometric the carrier concentration values reduce from 2.1×10^{18} cm^{-3} (O/Zn=0.5) to 6.6×10^{17} cm^{-3} (O/Zn=1) further increasing in the O/Zn ratio to O-rich condition leads to increasing the carrier concentration values again in up to 2.5×10^{18} cm^{-3} (O/Zn=1.5). On the other hand, the hall mobility increased with increasing the O/Zn ratio to be at the maximum value (69cm^2/Vs) at O/Zn=1.2 (nearly O-rich) then started to decrease again. This results because, in ZnO the zinc interstitials (Zn_i) native defect, a double donor, has a low formation enthalpy under both Zn-rich and O-rich growth conditions [141]. The native defects that can compensate Zn_i, such as oxygen interstitials (O_i) or zinc vacancies (V_{Zn}). Therefore, electrons from native defect are the dominant carriers in ZnO in O-rich and Zn-rich growth conditions, while the role of this native defect is less at the stoichiometric growth conditions.

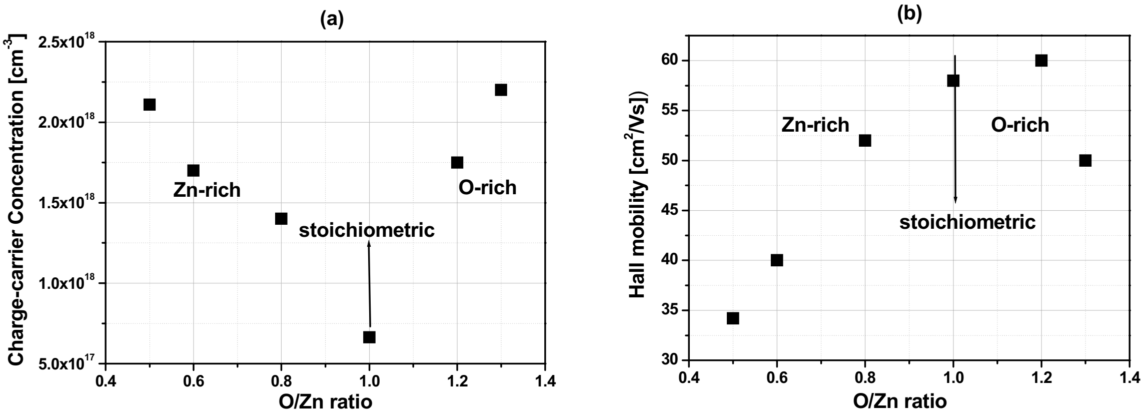

Figure 3.30: *shows the influence of O/Zn ratio on: a) the carrier concentration b) the hall mobility.* All other growth parameters except the O/Zn ratio were the same.

Another important parameter for the electrical properties of the ZnO layers was the sample thickness. Table 3.1 shows the chanenge in the carrier concentration and the hall mobility at room temperature versus the sample thickness. It can be clearly seen that hall mobility at 300K increases with increasing the ZnO layer thickness and hall carrier concentration in contrast decreases.

Sample thick (μm)	0.25	0.5	2.5
n (cm^{-3})	6.5×10^{17}	4.5×10^{17}	6.0×10^{16}
μ (cm^2/Vs)	55	67	96

Table 3.1: *shows the change in the carrier concentration and the hall mobility at room temperature versus the sample thickness.*

In order to better understand the electronic properties of the samples, temperature-dependent Hall measurements were performed. A plot of carrier concentration and electron hall mobility as a function of temperature for the sample of 2.5 μm thick is shown in Figure 3.31. The carrier concentration behavior is monotonous and the value changes a little through the whole nearly constant for all temperature range while the hall mobility increases with decreasing the temperatures till 70K and then become constant. The observed behavior suggests that the dominant current conduction mechanism may be through defect hopping with a lower density of defects available for conduction as the temperature decreases.

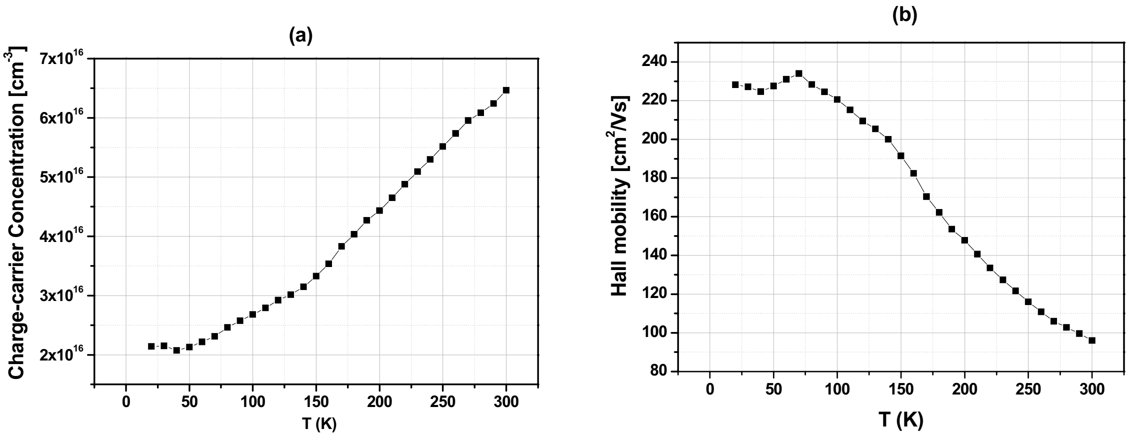

Figure 3.31: *Hall-effect measurements: a) plot of carrier concentration b) electron mobility as a function of temperature.*

The same sample with 2.5 μm was also investigated with ECV profiling using a 0.1 mol $ZnCl_2$ solution as an electrolyte. Figure 3.32 shows the carrier concentration of ECV profile versus depth measured for the top of 2.5 μm thick sample. The surface carrier concentration is $2.0\text{x}10^{16}$ cm^{-3}, increasing to a maximum value of $1.0\text{x}10^{18}$ cm^{-3} at the ZnO/sapphire substrate interface.

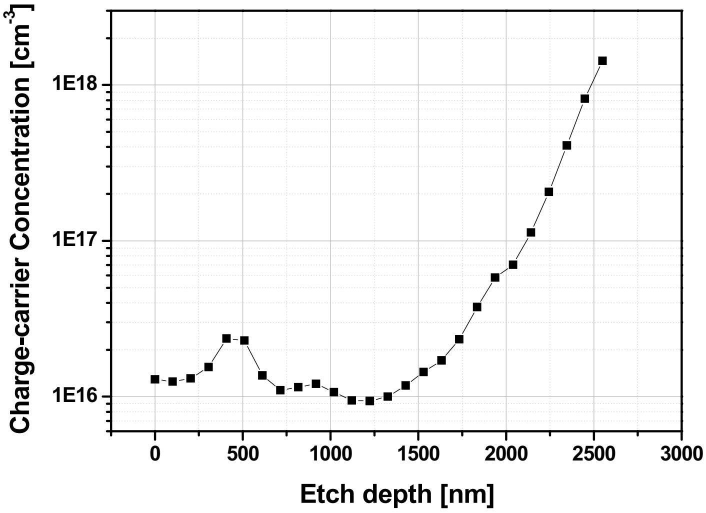

Figure 3.32: *Carrier concentration of ECV profile for a 2500 nm ZnO layers grown on c- Al_2O_3 etched with 0.1 M $ZnCl_2$.*

The distribution of charge-carriers is obviously homogeneous beginning from approximately 1.0 μm away from substrate. This behavior is typical of the specimens examined of ZnO grown on sapphire, as was shown for GaN on sapphire [142]. As it was disucused in section 3.4 Figure 3.10. One can obviously see screw and mixed dislocation lines. In case of the sample grown without MgO buffer (Figure 3.10a) the density of dislocations is noticeably higher near the layer/substrate interface Zone. Considering this, one can conclude that most dislocations are formed in the surrounding area of sapphire substrate. Also in Figure 3.17c the Fourier-filtered image at the interface illustrates the character of edge-dislocation lines formation. For six atomic planes of ZnO there are seven atomic planes of sapphire, which produces an edge-dislocation directly at the interface, but further along the c-axis in ZnO the atomic packaging looks perfect representing no edge-line defects.

Bringing all together, the behavior of electrical properties of samples with different thicknesses and c-axis inhomogeinity of charge-carrier distribution with a sharp rise at the interface becomes clear. While a big part of the electronic transport of thinner layers takes place at the interface between the substrate and epitaxial layer, where the density of one-dimensional defects is very high and, thus, mobility of electrons is lower, the role of interfacial part is less pronounced in thicker samples. This results in a higher mobility. The dislocations enforce also the generation of intrinsic point defects which act as shallow donors and increase the charge carrier concentration.

4. ZnO-based device structures

For the development of ZnO-based optoelectronic devices, it is necessary to have high quality materials of both n-type and p-type. Although there are a number of reports on p-type measurements in ZnO films, today there is still no reproducible and reliable method of producing good quality p-type ZnO. High quality undoped ZnO layers grown using HT MgO buffer is naturally of n-type that has been already reported (chapter 3). It is generally recognized that these native defects and $(N_2)_o$ donors in the case of Nitrogen doping of ZnO makes challengeable fabrication of p-doped epitaxial ZnO. [143]. P-type heteroepitaxial substrates such as SiC and GaN epilayers with less lattice mismatch to ZnO are promising for the realisation of p-n heterojunctions while work is ongoing to overcome the problem of p-doping ZnO and facilitate the obtain of p-n homojunctions. In this chapter, the fabrication of p-n heterojunctions and studies of N-doped based ZnO layers will be presented.

4.1. ZnO-based hetero-junction

The p-n junction is necessary for applications in optoelectronics and also for many applications in microelectronics. This requires a controllable n- and p-type doping in ZnO. Acceptor incorporation in ZnO has proven to be a great challenge to the ZnO research community. The general reason for this is the very low solubility of dopants and doping compensations by native defects. So far, the properties of ZnO might be best exploited by constructing hetero-junctions with ZnO active regions; in this way, the emission properties of an LED can still be determined by the advantageous properties of ZnO. Therefore, the growth of n-type ZnO on other p-type materials could provide an alternative way to realize ZnO-based p-n hetero-junctions. Lately, many p-n hetero- junctions have been achieved using various p-type materials (GaN, AlGaN, Si, CdTe, GaAs, and Diamond) [144]-[149]. The main factor to be considered, which influences the properties of the p-n hetero- junctions, is the close lattice match of ZnO layer and the substrate employed. In this case 4H-SiC is a good candidate since it has the same wurtzite crystalline structure and relatively good lattice matching to ZnO with lattice misfit of ~5%. Only few reports on the growth of n-ZnO on p-SiC hve been published [150]; [151]. Figure 4.1 shows the band alignment for the n-ZnO/p-SiC p-n junction deduced with the help of the Anderson model [152]. Such a band alignment strongly depends on the difference in the electron affinity χ of the materials forming the p-n junction and interface effects such as interface dipoles. Different values of electron affinity have been published for SiC. In any case, the resultant band alignment is of type II. In the case of forward bias, electrons on the conduction band of the n-type ZnO should drift towards the active region (middle) of the junction, and holes on the valence band of the p-type 4H-SiC should drift also towards the active region from other siade. Since ZnO is the material of interest, the best case scenario would be for the active region to be on the ZnO side of the p-n heterojunction. This could facilitate application in light emission e.g. LED and near ultra-violet radiation detection (for example a photodiode).

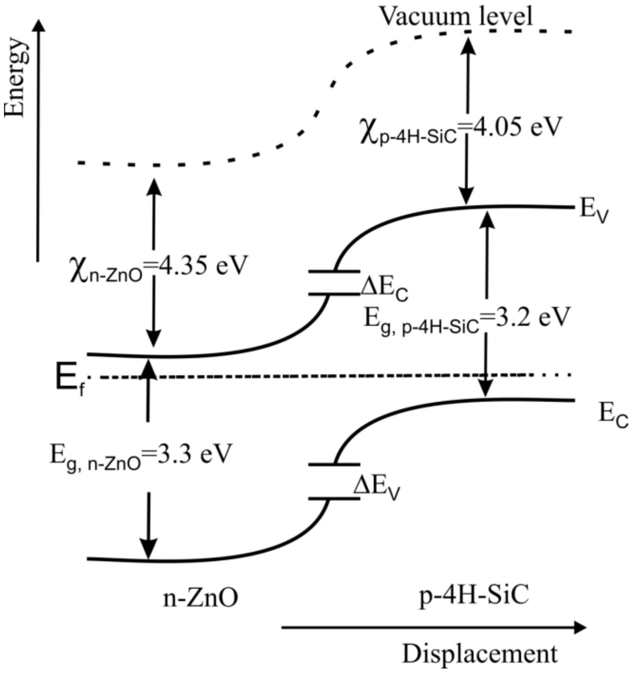

Figure 4.1: *Band diagram of an n-ZnO/p-SiC p-n junction*

4.1.1. Growth of n-ZnO layers on p-4H-SiC

The p-type 4H-SiC epilayers were previously prepared in a horizontal hot-wall reactor by chemical vapour deposition (CVD) on commercially available 4H-SiC (0001) substrates misoriented 8° towards $<11\bar{2}0>$ in the Institut für Kristallzüchtung Berlin[153]. They are 10−27 µm thick and have a hole concentration of $>5\times10^{18}$ cm^{-3}. The growth of n-ZnO layers is carried out using MBE system described before in chapter 2. Before loading the p-SiC substrate into the reactor, it was sequentially cleaned with organic solvents, H_2SO_4:H_2O_2 (1:1), rinsed with deionised water followed by immersion in a HF solution in order to remove the surface oxide. The substrate was loaded directly to the buffer chamber and then thermally cleaned at 900°C for 60 min. After that the substrate was transferred to the growth chamber. The growth started with a LT ZnO buffer layer grown at 200°C under Zn-rich conditions. After the deposition of the 6 nm thick ZnO buffer, RHEED patterns gradually changed from streaky to spotty. The growth has been then stopped and annealing started at 700°C for about 5 min. Then a streaky RHEED pattern of ZnO appeared again. This procedure was repeated several times in order to produce a thicker ZnO buffer layer. The main ZnO layer was grown at 450°C. At the end of the growth, the RHEED pattern becomes spotty, indicating an increase in surface roughness. According to the RHEED, ZnO single crystalline hexagonal wurtzite structure layers on 4H-SiC substrate were obtained. The improvement in crystal quality of the ZnO film is assessed by XRD. Only two peaks at (0002) and (0004) were obtained from wide angle ω–2θ XRD scan of the ZnO layers grown on 4H-SiC (0001) substrates. This indicates the c-axis oriented growth of the ZnO layers on SiC substrate. Figure 4.2 shows the XRD ω-rocking curve of the ZnO (0002) diffraction peak. The full width at half maxim (FWHM) of the (0002) rocking curve has the value of 0.13°. This FWHM value is to our knowledge the lowest for ZnO layers on 4H-SiC substrates compared to 0.32° on 6H-SiC substrate [154].

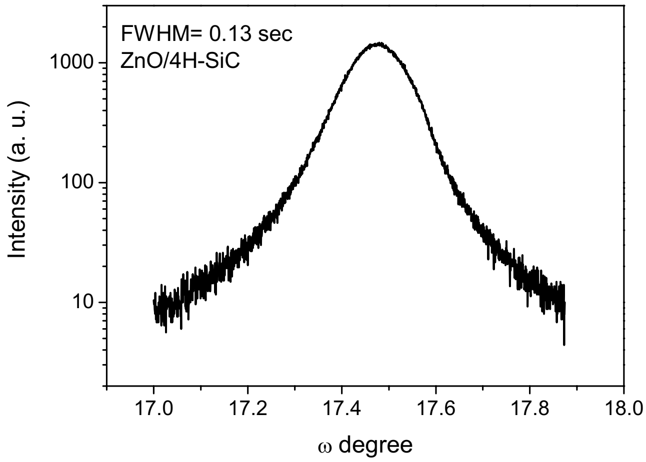

Figure4.2: *(0002) Omega rocking curve of ZnO layer grown on 4H-SiC substrate (FWHM is 0.13°).*

4.1.2. Characterisation of n-ZnO/p-SiC heterojunctions

Mesa diode structures were fabricated with diameters of 130 µm. Ti/Au 30nm/300nm were deposited on the n-ZnO area of the p-n heterojunction diode by electron-beam evaporation. These metal contacts were also used a a mask for mesa structure etching. A 0.5% HCl aqueous solution has been used to etch the ZnO layer down to the p-SiC layer. This technique exploits the property of ZnO to be etched rapidly in acids, while, Ti/Au and p-SiC layers are very resistive to these chemicalsAfter that Ohmic contacts with a diameter of 1.0 mm to p-SiC were achieved by sputtering 150 nm Al at room temperature, followed by rapid isothermal annealing at 650°C /120 s, and 920°C/300 s at 10^{-4} mbr pressure.

.

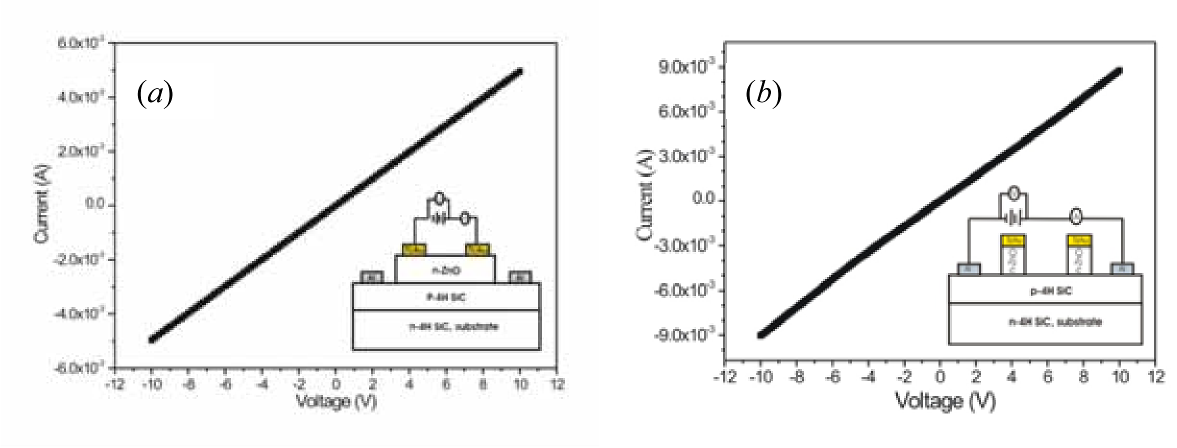

Figure 4.3: *a) I-V characteristics on two Ti/Au metal contacts on n-ZnO. Inset gives the cross sectional view of the fabricated contacts.*

b) I-V characteristics on tow Al metal contacts on p-SiC. Inset gives the cross-sectional view of the fabricated contacts.

The schematic digrams of the fabricated devices are shown as the inset of Figure 4.3 and Figure4.4 Current-voltage (I-V) characteristics of the heterostructures were measured on the fabricated mesa structures.

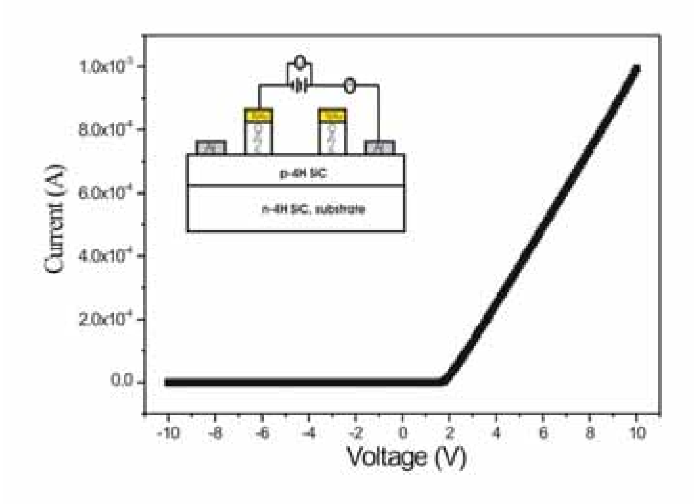

Figure 4.4: *I-V characteristics of n-ZnO/p-4H-SiC heterostructures showing clear rectifying behavior. Inset gives the cross-sectional view of the fabricated p-n heterostructures.*

The Hall measurements of both p-SiC and n-ZnO films were made at room temperature (RT) using the four-point van der Pauw technique. The intrinsic carrier concentrations of the ZnO layers determined from Hall measurement yields that the film has a background *n*-type carrier concentration of $6\text{x}10^{17}$ cm^{-3} and a Hall mobility of 55 cm^2/V sec. Figure 4.3 shows the *I-V* curve measured for a pair of Ti/Au contacts on the top of n-ZnO layers (a) and a pair of Al contacts on p-SiC (b). The linear trend shows good Ohmic contacts. After ensuring Ohmic behavior of the metal-semiconductor interfaces, *I-V* of the ZnO *p-n* heterojunction was measured at room temperature. The measurement results are shown in Figure 4.4. The turn-on voltage of the diode is around 2 V as seen from the *I-V* characteristics, from where the exponential increase in current begins. Turn-on voltage of about 2 V is reasonable due to the wide band gap of ZnO [155].

4.2. Quest for p-n homojunction in ZnO: N-doping

From the theory, nitrogen is the most promising element for *p*-type ZnO [14]. As it is already mentioned, nitrogen can be brought into ZnO to the concentrations of more than 10^{19}cm^{-3} [156]. In the other experiments electron paramagnetic resonance measurements have demonstrated that N substitutes O in the ZnO lattice [157]. There are some reports on N-doped ZnO, achieved with different growth methods [158];[159];[160]. Unfortunately, these experiments are still irreproducible. One of the explanations for the difficulties with nitrogen doping is the formation of the double N complex, which promotes the formation of the compensating defects [161].

4.2.1. Growth of nitrogen-doped ZnO layers

ZnO:N epilayers with a thickness of about 400nm were grown by MBE described earlier (chapter 2), which employs an RF-plasma-activated oxygen-nitrogen flux mixture, on c-sapphire substrates using. Oxygen and nitrogen fluxes were activated in the single plasma cell at the RF-power of 400W. The buffer layer sequence comprising HT thin MgO layer and totally 250 nm-thick undoped n-ZnO layers (chpter 3) ensures reproducibly the 2D growth mode of bulk ZnO:N epilayers at the 350-480ºC T_S range. The O/Zn flux ratio was varied from 0.11 to 1.25, whereas N flow rate was in the 0.5-1.2 sccm range.

The growth regimes for all samples under consideration are listed in the Table 4.1. The as-grown samples were compared with those exposed to the post-growth annealing during 30 minutes in a quartz reactor in the air within the 650-800ºC temperature range. Figure 4.5 presents SEM images of the layers, grown at different *Ts* under the Zn- and O-rich conditions. The images were taken before the annealing procedure. One can see that the surface morphology does not significantly depend on the O/Zn flux ratio at such a low oxygen excess [162], but rather controlled by the growth temperature.

Ts, ^{0}C	**O/Zn**	**d, nm**	**N flux, sccm**	**CV measurements (300K): type of the conductivity**			
				As-grown	**650°C, 30min**	**700°C, 30min**	**800°C, 30min**
480	0.41	410	0.8	compensated	n-type	-	compensated
450	0.25	320	1.2	compensated	n-type	-	-
400	1.19	860	0.48	compensated	n-type	-	-
400	0.89	370	1.2	compensated	p-type	p-type	-
400	1.08	420	2	p-type	-	p-type	-
375	1.25	390	1.2	compensated	-	p-type	-
350	1.08	420	2	compensated	-	p-type	-

Table4.1: *Growth regimes and type of the conductivity for the as-grown and annealed ZnO:N films. (CV measurements by Prof. S. Ivanov Ioffe Institute, St. Petersburg, Russia)*

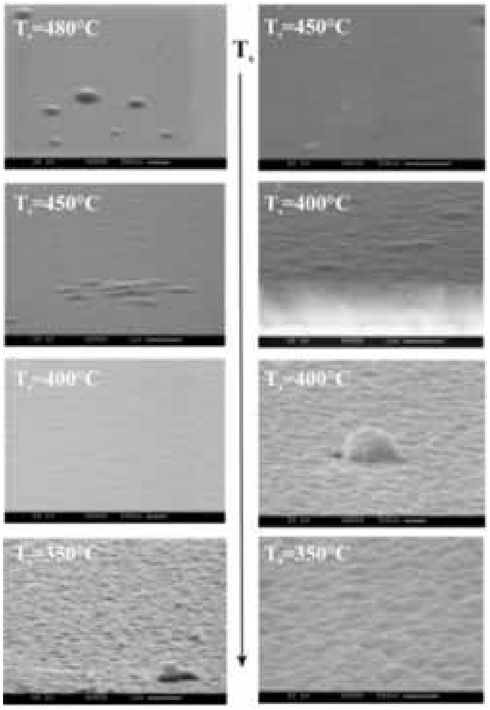

Figure4.5: *SEM images of the non-annealed ZnO:N layers grown in Zn-rich (left column) and O-rich (right column) conditions.*

Images reveal rather flat surface of the samples grown at T_S exceeding 400°C. At the lower T_S the surface roughness increases. Figure 4.6 shows SEM images of sample grown at 350°C before and after the annealing procedure. One can see that the heat treatment flattens slightly the surface morphology of the film, keeping a 2D character of the surface even after 800ºC annealing.

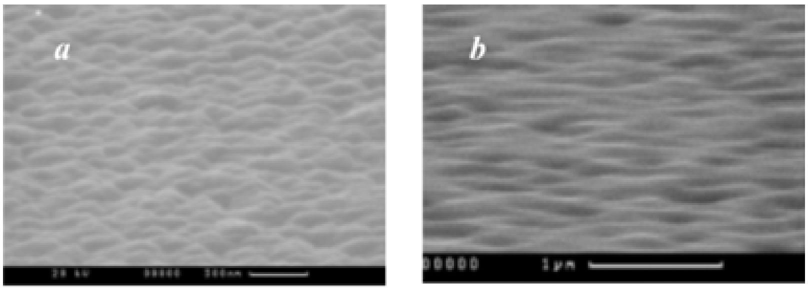

Figure 4.6: *SEM images of sample grown at 350°C: before (a) and after (b)*

4.2.2. Crystalline quality of nitrogen-doped ZnO layers

For the detailed characterization of the internal crystal quality of the N-doped ZnO films XRD analysis was used. Measurements were performed with a triple-crystal diffractometer using different diffraction geometries: symmetrical Bragg, symmetrical Laue and grazing incidence ones. Diffraction pattern was measured in a θ–2θ-scan mode and ω–mode. Intensity mapping around the reciprocal lattice point for the asymmetrical Bragg reflection (11-22) was obtained as well. Analysis of the peak broadening in different geometry using the approach [163] resulted in defining the principal parameters of the layer microstructure, namely, components of the microdistortion tensor and the size of coherent regions in parallel and normal directions to the surface. The densities of different dislocation ensembles have been calculated. Figure 4.7 demonstrates θ–2θ-scan diffraction peaks for ZnO:N layer, grown at T_S=400°C, in the symmetrical Bragg reflection (0002) (solid line) and the Laue reflection (10-10) (dashed line). Narrow diffraction peak in the symmetrical Bragg geometry indicates that there are very few threading dislocations with screw components in the film. Nevertheless, the comparison of the θ–2θ-peak widths measured in both geometries evidences that the density of the threading edge dislocations, which affect the Laue diffraction only, is rather high.

T_s, °C	ρ vert. screw, cm^{-2}	ρ vert. edge, cm^{-2}	ρ bound, cm^{-2}	ρ horiz., cm^{-2}	τz, μm	τx, μm
400	$<10^6$	$1.0x10^9$	$6.2x10^8$	$1.2x10^7$	0.6	>1
350	$1.6x10^9$	$1.1x10^{10}$	$1.3x10^{10}$	$9.0x10^8$	0.35	0.15

Table 4.2: *Density of dislocations (ρ) and coherent region dimensions (τ) determined from the X-ray diffraction data*

Table 4.2 shows the defect structure parameters (density for individual dislocation types and dimensions of coherent regions *τx*), obtained from the analysis of the diffraction peaks of the samples grown at T_S = 400°C and 350°C. It can be seen that the *τx* value obtained from the Bragg reflection analysis is in a good agreement with the scale of the surface roughness in the SEM images of the samples. The sample grown at lower temperature (350°C) is characterized by the higher density of all type dislocations and quite small lateral dimension of the coherent regions.

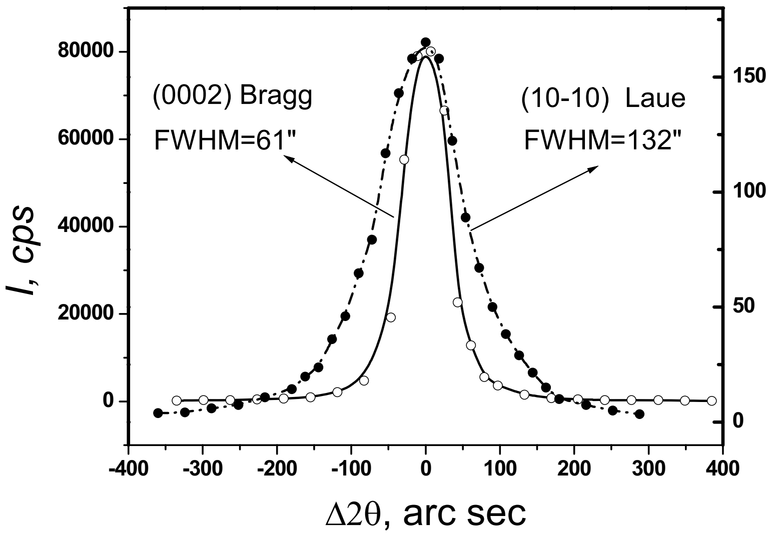

Figure 4.7: *θ–2θ–scan diffraction peaks for sample grown at 350°C in symmetrical Bragg reflection (0002) (solid line) and in Laue reflection (10-10) (dash line). (XRD measurements by Prof. S. Ivanov Ioffe Institute, St. Petersburg, Russia)*

The high-temperature film (400°C) contains primarily pure edge threading dislocations perpendicular to the sample surface. A part of these dislocations is located in small angle boundaries causing a rotation of crystalline blocks around the normal to the surface (twisting). Summarizing the results of the structural characterization, we can conclude that ZnO:N films grown at low temperatures contain more imperfections than those grown at higher T_S. Surprisingly, only the former films demonstrate p-type conductivity after the annealing procedure as will be shown below.

4.2.3. PL measurements

The low temperature (77K) PL spectra (Figure 4.8) contain "green" band in energy range (2.1-2.5) eV, which is attributed to the defects in ZnO and the UV band edge emission. One can see that the "green" band is dominated as compared with UV band in PL spectra of the two samples grown at Ts=350°C.

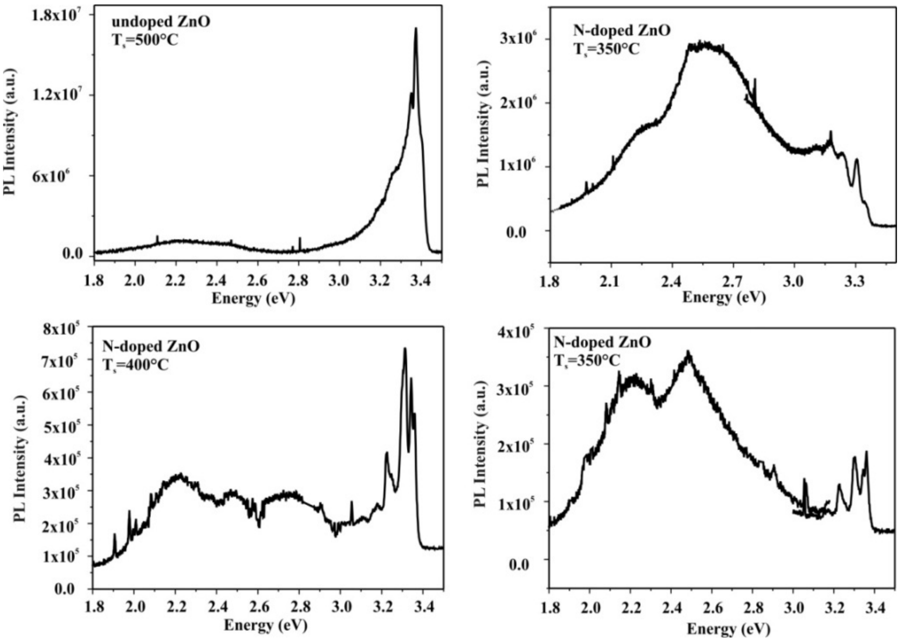

Figure 4.8: *PL spectra of undoped ZnO and N-doped ZnO at 77 K. (PL measurements by Prof. S. Ivanov Ioffe Institute, St. Petersburg, Russia)*

Figure 4.9 presents the details of the band edge PL. Preliminary identification of the PL lines observed is the following. The spectra of the annealed buffer layer demonstrate neutral donor-bond exciton band (D^0X), free exciton line (FE) and the LO-replicas of the free exciton line [164]. The spectra of N-doped samples contain D^0X line, band of emission of excitons bound to neutral acceptors A^0X at energy 3.345eV and 3.352eV [165]. After annealing at 700°C for 30 minutes in air, the line at 3.35eV which we associated with A^0X transitions became more clears. The spectrum of the sample grown at 350°C demonstrates additional line at 3.316eV, which is close to the two-electron satellite transitions associated with the neutral-bond exciton at 3.36eV [166].

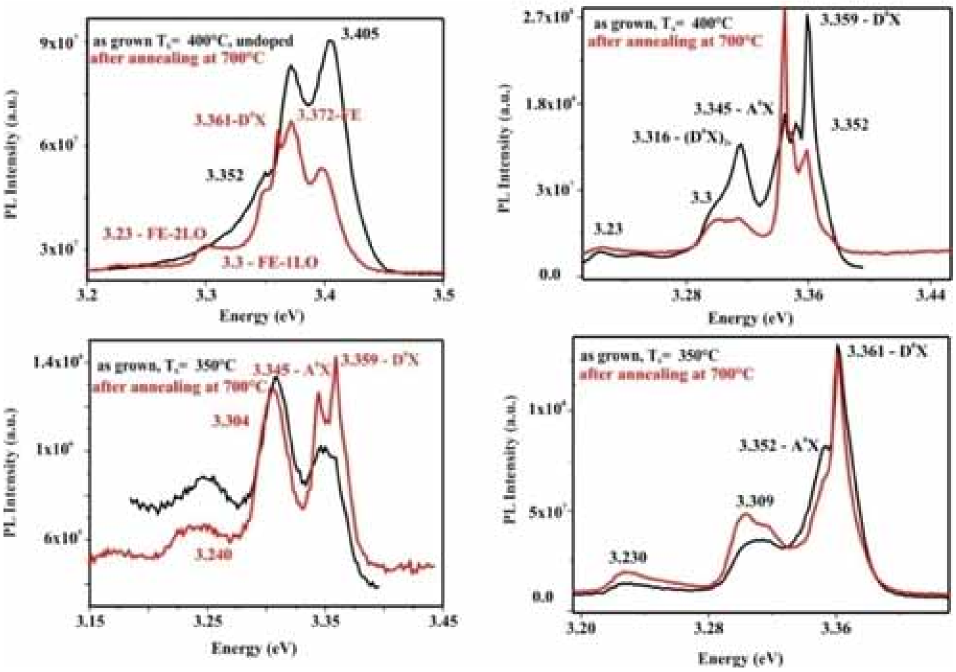

Figure 4.9: *Details of the band edge PL spectra of undoped ZnO and N-doped ZnO at 77 K. (PL measurements by Prof. S. Ivanov Ioffe Institute, St. Petersburg, Russia)*

The spectra of all N-doped samples contain band at (3.3-3.309) eV which may be related to the excitons bond to structural defects[166]. In the energy range (3.230-3.240)eV broad line is observed for N-doped samples, this line is very close to DAP transitions[165];[167].

4.2.4. SIMS measurements

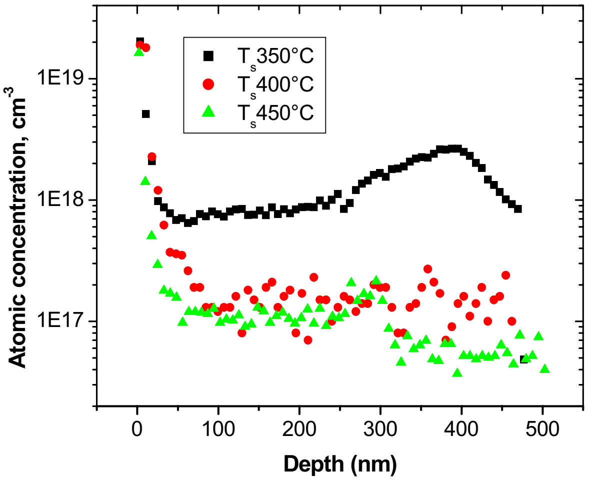

Figure 4.10: *SIMS profiles of N-doped ZnO films as a function of substrate temperature. (SIMS measurements by Prof. S. Ivanov Ioffe Institute, St. Petersburg, Russia)*

To determine the concentration of nitrogen dopant in our film, we used secondary ion mass spectrometry (SIMS). In a SIMS measurement, the surface of the sample is bombarded by primary ions (typically Cs+, O-, or O+), emitting secondary ions. Secondary ions are separated in a mass spectrum analyzer to yield information about the concentrations of specific elements. By digging a flat-bottom crater in the sample surface and analyzing the secondary ions from different depths, one can generate concentration profiles for different elements. Figure 4.10 shows the SIMS profile of a about 400 nm thick N-doped grown ZnO film, deposited on an (0001) sapphire substrate. The nitrogen concentration for sample grown at 350°C is quite uniform throughout the depth at about 1×10^{18} atoms/cm-3. The N concentration in the film decreases with increasing Ts, which may be due to the fact that the zinc atoms prefer to bind with oxygen than nitrogen at higher Ts due to larger binding energy of O–Zn bond. It is noticeable that the difference in N concentration becomes almost neglidble for T_s= 400°C or higher.

4.2.5. Electrical characterization

For the electrical characterization of the layers both CV and Hall measurements were employed. The parameters of the nitrogen-doped layers were compared with those of the undoped film. The results of the CV measurements for the ZnO:N films before and after annealing are summarized in Table 1. One can see that as-grown ZnO:N films are generally compensated except for MBN36, but some show p-type after the annealing. It is seen from the data that the lower T_S, the higher N-flow rate and the slightly O-rich conditions are favorable for achieving p-type conductivity in RS MBE using O-N gas mixture in a single plasma cell. One should mention that in the majority of the layers the frequency-dependent behavior of the p-type conductivity was observed. Undoped samples demonstrate usually n-type conductivity with the net carrier density around $1\text{x}10^{18}\text{cm}^{-3}$.

To verify the obtained results, Hall measurements were performed. The standard Van der Pauw geometry was used. Undoped sample showed n-type conductivity with the net electron density of $3\text{x}10^{18}\text{cm}^{-3}$ and mobility μ= 40 cm2/Vs (300K). ZnO:N layers demonstrated principally different behavior. All of them were grown atop an undoped buffer layer. To define properly a contribution of the buffer layer to measured electrical characteristics of the ZnO:N films, we assumed that the ZnO buffer layer and ZnO:N film are connected in parallel.

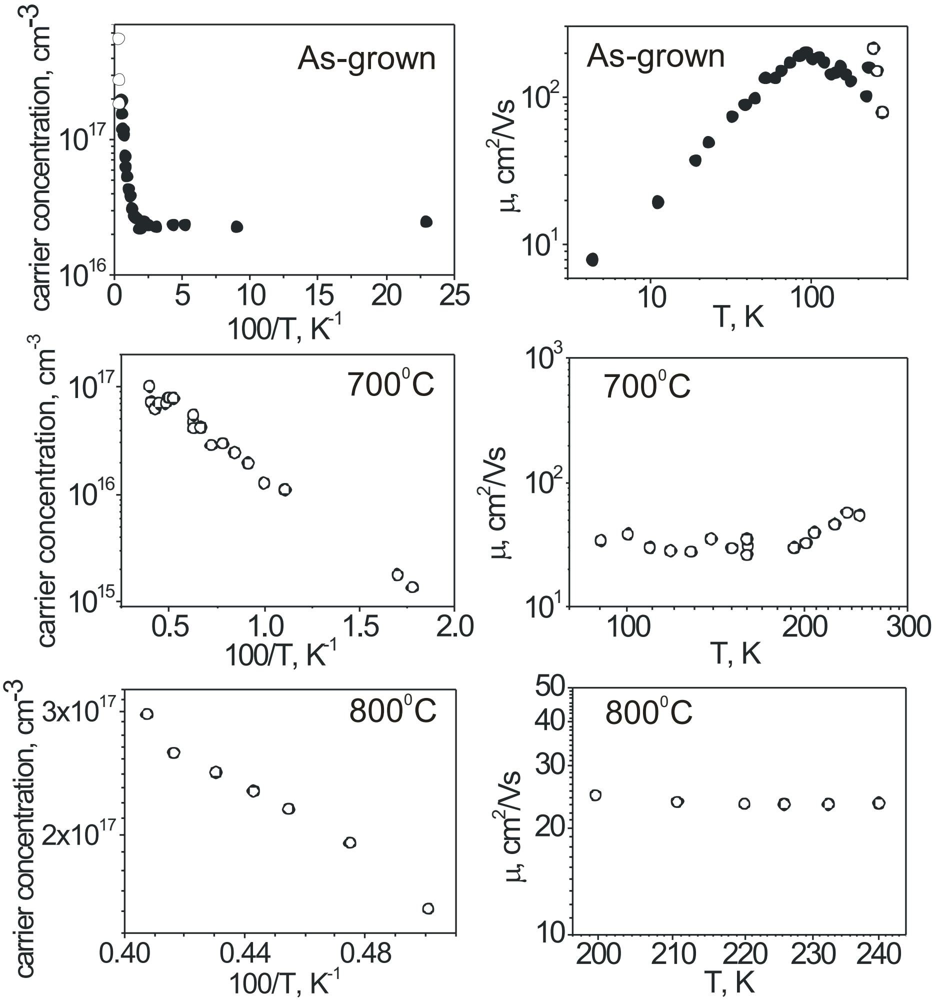

Figure 4.11: *Carrier concentration (left column) and mobility (right column) for the MBN36 film before and after annealing. Electrons are marked with filled symbols and holes with empty ones. (Hall-effect measurements by Prof. S. Ivanov Ioffe Institute, St. Petersburg, Russia)*

To verify the obtained results, Hall measurements were performed. The standard Van der Pauw geometry was used. Undoped sample showed n-type conductivity with the net electron density of 3×10^{18}cm^{-3} and mobility $\mu = 40$ cm^2/Vs (300K). ZnO:N layers demonstrated principally different behavior. All of them were grown atop an undoped buffer layer. To define properly a contribution of the buffer layer to measured electrical characteristics of the ZnO:N films, we assumed that the ZnO buffer layer and ZnO:N film are connected in parallel. Figure 4.11 presents the resulting dependences of the carrier concentration and mobility on the sample temperature (*T*) for MBN36 film before and after annealing. The as-grown film shows p-type conductivity, although only at T above 200K, while the n-type conductivity is observed at lower T that can be related to conducting through the n-type buffer layer. The annealed samples exhibited clear p-type in the wide temperature ranges. At T = 300K the following parameters were demonstrated by MBN36 sample annealed at the temperature of 700°C and 800°C: p = 1x10^{17} cm^{-3}, μ= 55 cm^2/Vs and p = 3x10^{17} cm^{-3} , μ= 25 cm^2/Vs, respectively. The former hole mobility value could be slightly overstated due to the influence on measurements of the buffer layer via vertical dislocations shunting a p-n junction, that cannot be taken into account in the used simplest model.

The obtained results can be explained in the frame of the compensating defect formation models in ZnO, developed in the number of papers and based on the first-principle calculation[143];[168]. In these works it was shown that donor-type defects (such as Zn_i, V_O, $(N_2)_O$) have rather low formation energy and that net p-type doping requires a delicate balance between the necessity of high dopant solubility and low concentration of compensating donor defects. We suggest that in our experiments the main compensation mechanism via the point defects Zn_i and V_O is overcome by the slightly O-rich conditions which still does not suppress significantly proper N incorporation in O vacancies, while the low T_S and as high as possible N flux facilitate the N incorporation. The formation of $(N_2)_O$ donors expected under the RF-plasma conditions is assumed to be partly eliminated by the annealing. The rough surface morphology appears to be a positive factor also, as it provides a much larger density of surface dangling bonds for N incorporation as compared to the flat one. However the worse structural quality obviously prevents obtaining LED devices due to the shortage of a p-n junction by the vertical edge dislocations.

5. ZnO/ZnMgO heterostructures

Excitons in ZnO-based quantum well heterostructures exhibit high stability compared to bulk semiconductors or III–V QWs due to enhancement of the binding energy and reduction of the exciton–phonon coupling [169][170]caused by quantum confinement. Due to these effects, excitons are expected to play an important role in many-body processes such as laser action and nonlinear absorption of ZnO QWs even at room temperature. In principle the threshold for lasing using biexcitons is expected to be ever lower than that using an exciton-exciton scattering process[172]. There is a great potential in the possibility of using biexcitons as a laser action mechanism for UV wavelengths and room temperature operation because of their large binding energy in ZnO (12-16 meV) and ZnO quantum wells (more than 30 meV)[171]. There are only a few papers on the coherent optical properties of excitons and biexcitons in ZnO[173][174][175]. A detailed study of excitons and biexcitons in ZnO quantum wells (QWs) is thus important for understanding the optical properties of these wide band gap heterostructures, especially in view of their potential application to ultraviolet–blue optoelectronic devices [176]. This chapter presents the growth and characterisation of $Zn_xMg_{1-x}O$ layers, single ZnO/ZnMgO quantum well structures grown on ZnO layers and ZnO nonorods to fabricate ZnO/$Zn_xMg_{1-x}O$ quantum well structures and superlattices, it is important to produce a smooth film surface and high interface flatness. ZnO/$Zn_xMg_{1-x}O$ heterostructures were grown on 300 nm ZnO epiwafer produced using the MBE growth system (see chapter 3) and ZnO nanorods fabricated using the grown in collaboration with Augustine Che Mofor, who operates the vapour-transport system..

5.1. Growth of ZnMgO layers

The growth of ZnO and $Zn_{1-x}Mg_xO$ layers with up to 30% Mg (determined prior to growth using a quartz crystal monitor) was carried out on ZnO quasi-substrate in the same MBE system described in chapter2. First, a high quality ZnO layers with thickness of 300 nm was grown on 2-inch (0001) sapphire substrate (see chapter 3). These ZnO layers were then used as wafers for the growth of ZnMgO without additional cleaning. One quarter of the 2 inch ZnO wafer is employed for each ZnMgO growth experiment. The growth rate of ZnO was determined by the oxygen flow rate and growth was carried out under matrial-rich condition. The Mg composition was controlled by changing Mg deposition rate. Prior the growth of ZnMgO layers, RHEED oscillations were obtained from ZnO quasi-substrate (Figure 5.1a). Then $Zn_{1-x}Mg_xO$ growth started at 450°C, also RHEED oscillations were obtained from

$Zn_xMg_{1-x}O$ layers. Figure 1b shows the RHEED oscillations detected during $Zn_{0.9}Mg_{0.1}O$ growth at a substrate temperature of 450°C on ZnO wafer. Figure 5.1 (c and d) show the Atomic force microscope (AFM) images of the 300 nm thick ZnO and a 200 nm $Zn_{0.9}Mg_{0.1}O$ surfaces. The scan area is 2 µm × 2 µm. The root mean square (rms) roughness values determined from the scans are 0.26 nm and 0.7 nm of as grown 2-inch ZnO layers and $Zn_{0.9}Mg_{0.1}O$ layers, respectively.

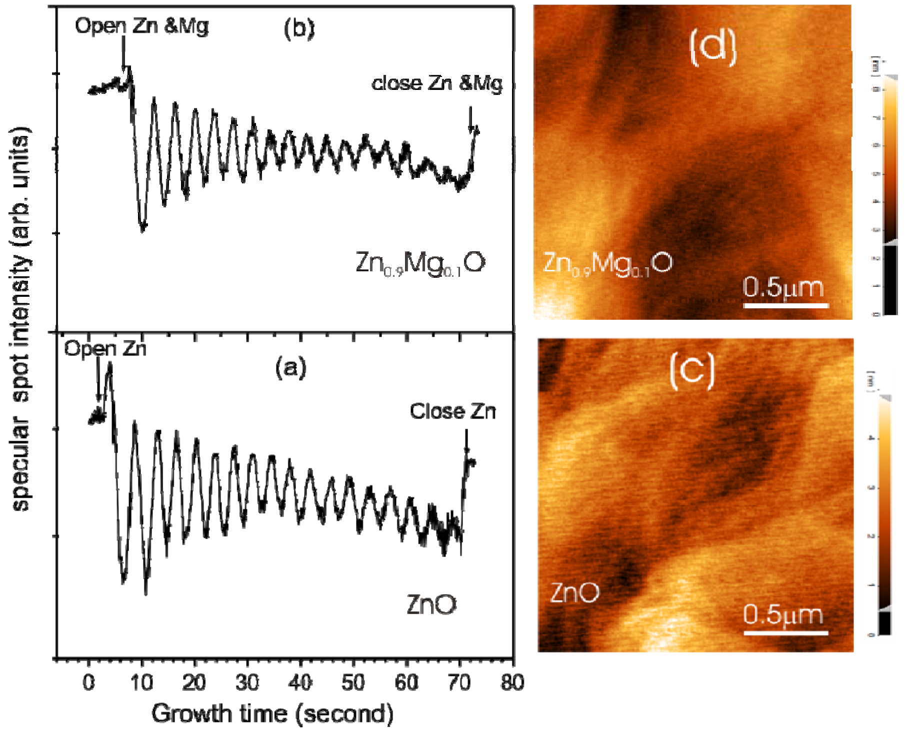

Figure5.1: *a) RHEED specular spot intensity oscilllations on 00 rod on <1-100> azimuth on ZnO, arrows indicate where the growth is interrupted.*

b) AFM image of 200 nm $Zn_{0.9}Mg_{0.1}O$ *layers grown on ZnO epiwafer with rms value of roughness is 0.7 nm.*

Single phase $Zn_xMg_{1-x}O$ ($x \leq 0.30$) thin films having wurtzite structure and c-axis orientation have been prepared on high quality ZnO wafer. At Mg composition higher than 30%, RHEED pattern change from wurzit to rocksalt, as verified by RHEED and XRD analysis. As the sample was rotated around its axis, each RHEED pattern was repeated every 60° which proves the hexagonal wurtzite structure of the $Zn_xMg_{1-x}O$ ($x \leq 0.30$) growing films.

Figure 5.2a shows the x-ray ω–2θ scan from a $Zn_{0.9}Mg_{0.1}O$ film both the first (0002) and the second (0004) order diffraction peaks for the ZnMgO layers are clearly seen. This indicates that the ZnMgO film is oriented to c-axis of the hexagonal wurtzit structure. Figure 5.2b shows the XRD *ω*–rocking curve of the same sample (0002) diffraction peak. The FWHM of the (0002) rocking curve is as small as 36 arcsec, implying little tilt in the *c*-planes. These properties of the (0002) diffraction peak indicate the extreme ordering along the (0001) growth direction of $Zn_{0.9}Mg_{0.1}O$ as a consequence of well controlled layer-by-layer epitaxial growth.

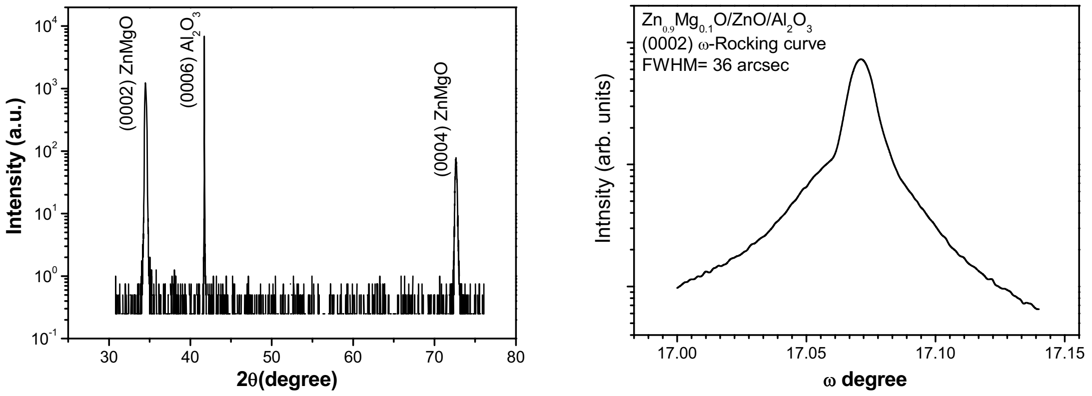

Figure5.2: *a) XDR ω–2θ scan from a $Zn_{0.9}Mg_{0.1}O$ film both the first (0002) and the second (0004) order diffraction peaks are clearly seen*

b) XRD ω–rocking curve of (0002) diffraction from the same sample (FWHM = 36 arcsec)

For the $Zn_xMg_{1-x}O$, the length of the c-axis evaluated from XRD measurements decreases with increasing Mg content (Figure 5.3c). Figure 5.3a shows PL spectra of $Zn_xMg_{1-x}O$ ($0 \leq x \leq 0.22$), taken at 13 K, where single phase thin films could be grown. With increasing Mg composition, the PL peak shifted to higher energy. Although the PL spectrum of ZnO (x=0) is dominated by the neutral donor bound-exciton (D^0X) at 3.355 eV, free excitons X_A can be clearly observed at 3.374 eV. As the Mg content is increased, the intensities of emission positioned at the higher energy side of D_X emission increase [177], concluding that excitons are hardly captured by impurities (figure 5.3b). This might be caused by the localized states since excitons in ZnO are more sensitive to local inhomogeneities due to its small Bohr radius. Thus, $Zn_xMg_{1-x}O$ films can be considered not only as barrier layers for the ZnO active layer, but also as an ultraviolet light emitting material, the luminescence energy of which can be tuned from 3.37(x=0) to 3.9 eV (x=0.3) by adjusting the Mg content.

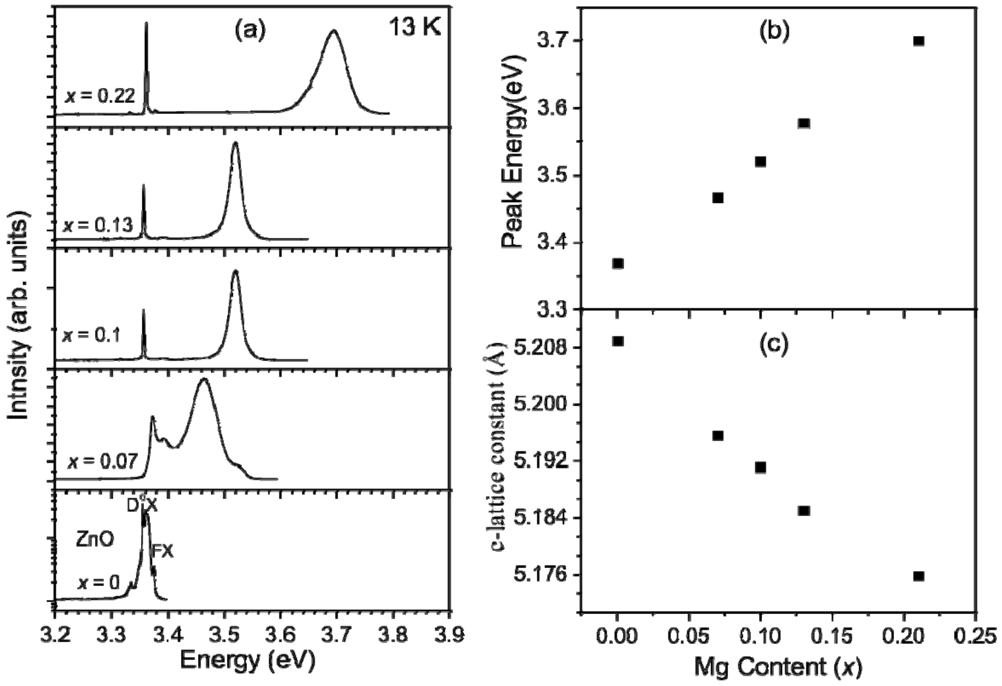

Figure5.3: *(a) PL spectra of ZnO and* $Zn_xMg_{1-x}O$ *(x up to 0.22) measured at 13 K excited by the 325.0 nm line of a HeCd, (b) the band gap evaluated from PL measurements, and (c) c-lattice length constant evaluated from XRD measurements dependence on the Mg content.(PL measurments by M. Al-Suleiman Institute of Semiconductor Technology,Braunschweig)*

The critical point for using ZnO/ZnMgO quantum wells as an active region of a UV laser is the quality of the ZnMgO barriers. To fabricate $ZnO/Zn_xMg_{1-x}O$ quantum well structures and superlattices, it is important to produce a smooth film surface and high interface flatness. By using a 300 nm high quality ZnO wafer, the surface of the ZnMgO alloy becomes as smooth as that the pure ZnO film. This surface roughness is very good for fabricating superlattice and quantum well structures.

5.2. Heterostructures

Heterostructures are formed from multiple heterojunctions, and thus a many of possibilities exist. If a thin layer of a narrower-bandgap material (A) say, is sandwiched between two layers of a wider-bandgap material (B), as illustrated in Figure 5.4 then they form a double heterojunction. If layer (A) is sufficiently thin for quantum properties to be exhibited, then such a band alignment is called a single quantum well. If any charge carriers exist in the system, whether thermally produced intrinsic or extrinsic as the result of doping, they will attempt to lower their energies. Hence in this example, any electrons (solid circles) or holes (open circles) will collect in the quantum well (see Figure 5.4). Additional semiconductor layers can be included in the heterostructure, for example multiple quantum wells or superlattices, as shown in Figure 5.4(right). The difference between the latter is the extent of the interaction between the quantum wells; in particular, a multiple quantum well exhibits the properties of a collection of isolated single quantum wells, whereas in a superlattice the quantum wells do interact.

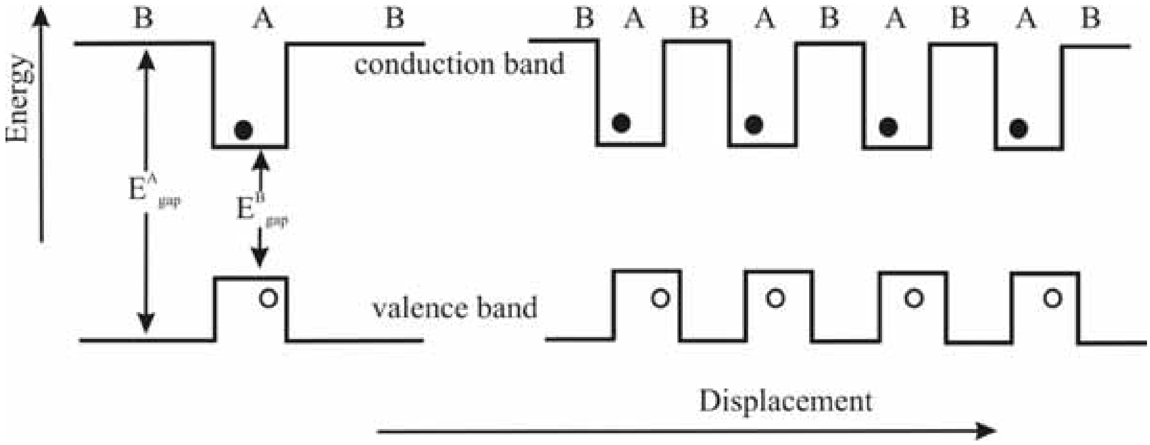

Figure 5.4: *The one-dimensional potentials V(z) in the conduction and valence bands for typical single quantum well(left)and multiple quantum well or superlattices (right). In this work: A≡ ZnO; B≡ ZnMgO*

The motivation behind introducing increasingly complicated structures is an attempt to tailor the electronic and optical properties of these materials for exploitation in devices.

5.3. Quantum confinement in semiconductors

One of the important features of semiconductor nanostructures is the flexibility of controlling and designing the properties of such materials [178][179], [180], including controlling the size [181][182], constructing artificial structures [183], [184] and using various doping [185]or some of the postgrowth techniques, such as intermixing [186]. Such nanostructures exhibit structural, electronic and optical properties that are unique and different from both macroscopic materials and isolated molecules. In nanostructures, normally 1 to 50 nanometers in scale, the dimensions are commensurate with the de Broglie wavelength of the charge carriers; so that quantum confinement effects become important and the properties of the semiconductors are significantly modified. Advanced semiconductor growth techniques, such as MBE and MOCVD, allow fabrication of various semiconductor nanostructures or low dimensional structures. Such low dimensional structures include (i) quantum wells (QWs), where the charge carriers are confined along the growth direction *z* but free to move in the other two directions x and y, (ii) quantum wires, where the charge carriers are confined in two directions and only allow one dimension motion, and (iii) quantum dots (QDs), where the charge carriers are confined in all three directions. Strong inter band transitions are possible in these low dimensional structures because there is a probability of a strong overlap between the wave functions of the electrons and holes. Figure 5.5 compares the density of states as a function of energy in different dimensional materials, bulk, quantum well, quantum wire and quantum dot.

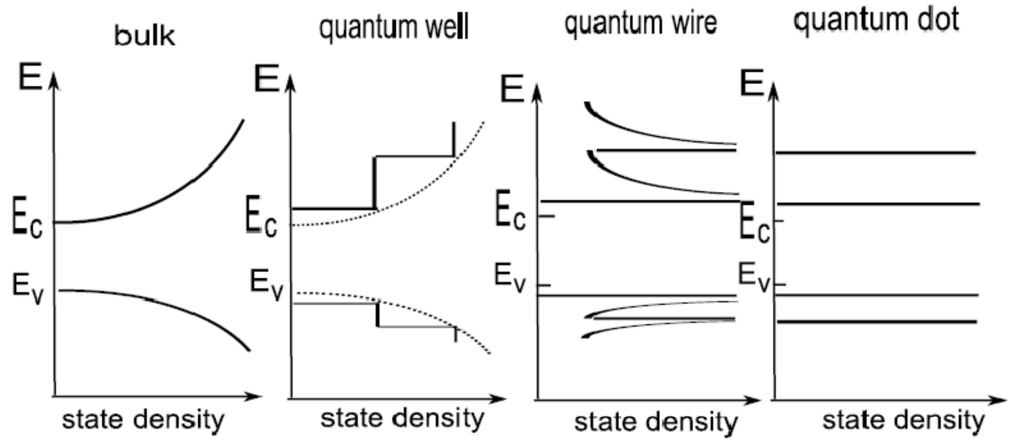

Figure 5.5: *Density of states as a function of energy in bulk, quantum wells, quantum wires and quantum dots.* E_c *and* E_v *indicate the bottom of the conduction band and the top of the valence band, respectively.*

In a quantum well system, due to the one dimensional confinement of electrons, the electron and holes energy levels can be found from the solution of the Schrödinger equation for an infinitely deep potential well, with the forms:

$$E_e = \frac{\hbar^2\pi^2}{2m_e^* L^2} n^2 \quad n = 1, 2, 3 \ldots. \tag{5.1}$$

$$E_h = \frac{\hbar^2\pi^2}{2m_h^* L^2} n^2 \quad n = 1, 2, 3 \ldots. \tag{5.2}$$

Where, m_e^* is the effective mass of the electron; m_h^* is the effective mass of the hole; and the dependence of the energy levels on $\frac{1}{L^2}$ is the quantum size effect.

The concept of a ZnO/ZnMgO quantum well can be explained with the fundamental understanding of a potential well. In this case, ZnO is sandwiched between two $Zn_xMg_{1-x}O$ barriers. The emission energy from such a quantum well can be represented as:

$$E_{\text{well}} = Eg,_{\text{ZnO}} + E_e + E_h + R \tag{5.3}$$

Where, E_e and E_h are given by (5.1) and (5.2). R is the resultant energy due to other effects whose energy contribution is either to be subtracted or added to the emission energy. Without considering such effects like piezoelectric fields that can lead to the Quantum Confined Stark Effect (QCSE), and exciton binding energies due to their low and insignificant magnitude, the first order emitted energy (n=1) from the ZnO/Zn$_x$Mg$_{1-x}$O quantum well can be calculated as:

$$E_{emit} = E_{g.ZnO} + \frac{\hbar^2\pi^2}{2m_e^*L^2} + \frac{\hbar^2\pi^2}{2m_h^*L^2} \tag{5.4}$$

This shows that the quantum well peak should be expected on the right of the ZnO peak on a photoluminescence spectrum and that the emitted energy is inversely proportional to the square of the well width L.

5.4. Fabrication of ZnO/ZnMgO SQWs

5.4.1. ZnO/ZnMgO SQWs on ZnO layers

Employing the good quality of both ZnO and ZnMgO layers achieved. First, a high quality ZnO layer with thickness 300 nm was grown on 2-inch (0001) sapphire substrate. These ZnO layers were then used as wafers for the growth of QWs structure without additional cleaning. One quarter of the 2 inch ZnO wafer is employed for each single QW growth experiment

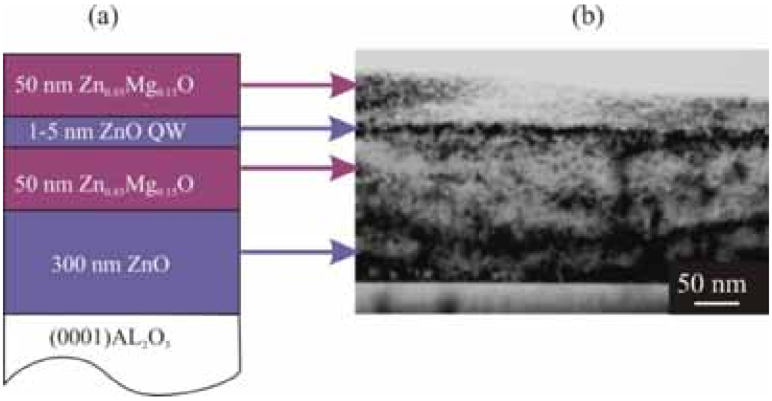

Figure 5.6: *ZnO/ZnMgO Schematic SQW structure (right) and XTEM micrographs from the ZnO/ZnMgO SQW structure (left)*

first Zn$_{0.85}$Mg$_{0.15}$O barrier of 50 nm thickness was grown at 450° C, followed by the ZnO well of width 0−5 nm and terminated with another 50 nm Zn$_{0.85}$Mg$_{0.15}$O barrier (Figure 5.6a). The heterostructure of the ZnO/ZnMgO was also studied by XTEM microscopy. Figure 5.6b shows the XTEM micrograph of 3nm SQW. One can clearly see the ZnO SQWs sandwiched between two $Zn_{0.85}Mg_{0.15}O$ barriers. PL measurements data were prepared by Mohamed Al-Suleiman, Institute of Semiconductor Technology, Technical University Braunschweig.

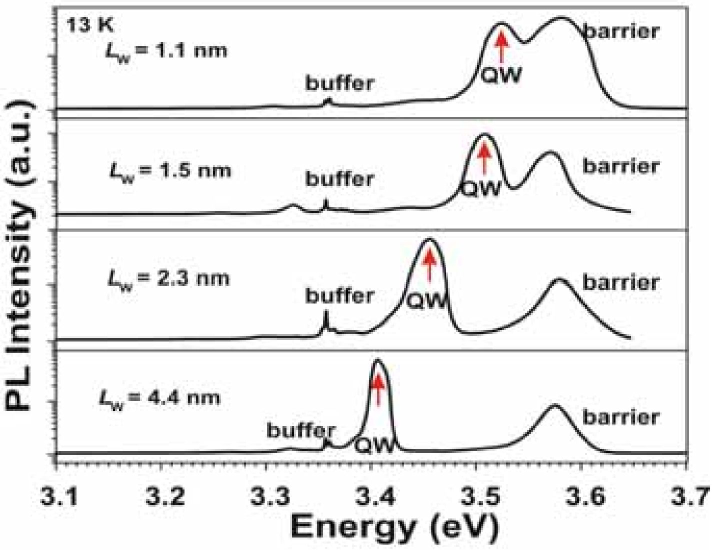

Figure 5.7: *PL spectra of $Zn_{0.85}Mg_{0.15}O/ZnO$ SQWs at 13 K with different well widths (L_W).*

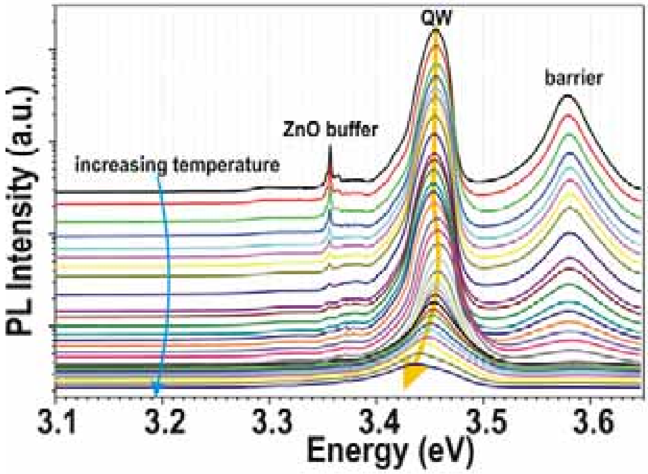

Figure 5.8: *PL spectra of a $Zn_{0.85}Mg_{0.15}O/ZnO/Zn_{0.85}Mg_{0.15}O$ SQW sample with well width of 2.3 nm at various temperatures. The SQW peak energy shows an S-shaped shift with increasing temperature as indicated by the corresponding arrow.*

Figure 5.7 presents the low-temperature PL spectra of $Zn_{0.85}Mg_{0.15}O/ZnO$ SQW with different well width (L_W). These PL spectra include two types of prominent emission peaks. As the thickness of the ZnO SQWs decreases, the corresponding emission peaks (marked by arrows) exhibit a blueshift due to the quantum size effect. For example, a blueshift of 32 meV in a 4.7 nm wide quantum well has been detected, which corroborates pretty well with the theoretical calculations [187]. The second peaks at higher energies remain in the same position and thus are attributed to emission from the $Zn_{0.85}Mg_{0.15}O$ barrier layer. The high quality of the SQWs reflected by the small FWHM of their peaks of down to 12 meV.

Figure 5.8 shows PL spectra of the 2.3 nm SQW as a function of temperature. As the temperature increases the SQW peak energy first shows a redshift relative to the band gap and then it shifts to higher energies, exhibiting a socalled "*S*-shaped" behavior [189],[190]. This behavior can be explained within the model of localized excitons [190]. At the lowest temperatures, excitons are localized even in shallow lateral potential fluctuations, which are due to the roughness of the ZnMgO/ZnO interfaces. When the temperature increased, excitons from shallow lateral potential fluctuations are delocalized, diffusing to regions with larger well widths and hence lower transition energies (redshift). Excitons localized in regions with wider well widths start to dominate at intermediate temperatures. As the temperature increases further (70> T>150) K, carriers have enough thermal energy to reach higher energies of the bandtail states caused by potential fluctuations due to alloy and interface fluctuations (blueshift). At even higher temperatures (T >150 K), the shift of the PL emission is mainly determined by the temperature dependent band gap energy according to the Varshni equation[191].

As is well known, monolayer fluctuations cause a broadening in the PL peak emission[192], [193]. Table 5.1 compares the values of the FWHM of four SQWs PL peaks and the change of the exciton confinement energy (ΔE) caused by assumed 1 ML fluctuation in the well width. The parameters used for this calculation taken from [187]. The FWHM values are comparable to the expected broadening caused by a 1 ML well width fluctuation.

Well width (nm)	4.7	2.3	1.5	1.1
FWHM (meV)	12	16.1	19.2	26.15
ΔE (1 ML) (meV)	10	17.5	21	29.5

Table 5.1: *The change of the exciton confinement energy caused by 1 ML fluctuation in well barrier in comparison with the PL peaks FWHM of the SQWs and.*

5.4.2. ZnO/ZnMgO SQWs on ZnO nanorods

The same technologies used before to fabricate ZnO/ZnMgO SQWs on ZnO layers were employed to fabricate the same heterostructures on nanorods grown with the vapour transport method. The nanorod samples were first thermally treated at 800° C for 40 minutes without oxygen flow to get rid of any surface contaminant. Followed by 30 minutes heating in an oxygen plasma overpressure of 3.1×10^{-5} Torr to create an oxygen-terminated surface that is known to favour ZnO growth. Then the first $Zn_{0.85}Mg_{0.15}O$ barrier of 50 nm thickness was grown at 450° C, followed by the ZnO *well* of width 0−4 nm and terminated with another 50 nm $Zn_{0.85}Mg_{0.15}O$ barrier. The thickness of the ZnO and $Zn_{0.85}Mg_{0.15}O$ structures is deduced from calibration results obtained using a quartz crystal monitor in the reactor. These thicknesses correspond with values calculated from reflection high-energy electron diffraction (RHEED) oscillations obtained during the growth of ZnO layers (chapter 3). The nanorod samples were characterised after MBE growth using SEM and photoluminescence. Figure 5.9 shows a sketch of the quantum well structure and an SEM image of ZnO nanorods on a 6H-SiC substrate after the growth of quantum well structures[188].

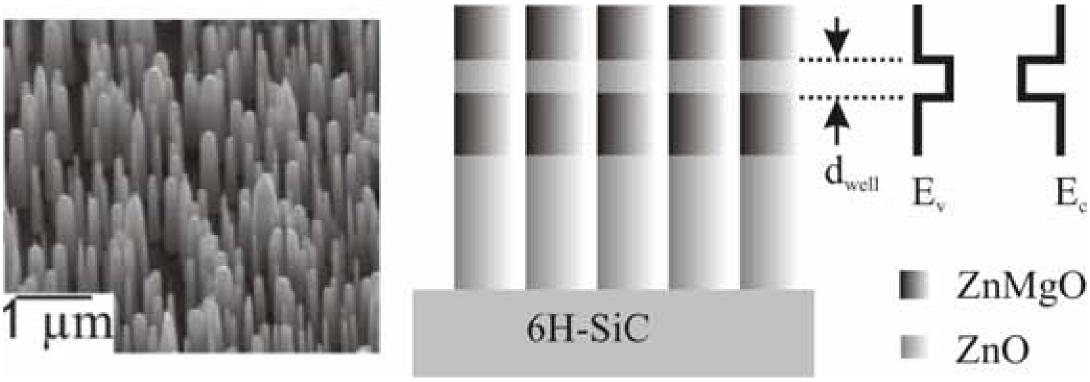

Figure 5.9: *Scanning electron microscopy image of ZnO nanorods after the growth of ZnO/ZnMgO quantum well structure*

Figure 5.10a shows PL spectra taken at 13 K for ZnO nanorods with single quantum wells of 3.5nm width. While donor-bound excitons (D^0X)-related peak around 3.36 eV from the main ZnO nanorods dominates in intensity, the $Zn_{0.85}Mg_{0.15}O$ barriers show a much weaker PL peak at 3.61 eV. Another peak appears between these two peaks. This additional peak at 3.421 eV is correlated with recombination in the 3.5 nm thick quantum well sandwiched between $Zn_{0.85}Mg_{0.15}O$ barriers. Despite the relatively low intensity of this quantum well peak, its FWHM of less than 15 meV is the least value known to have been reported so far in the literature[194].

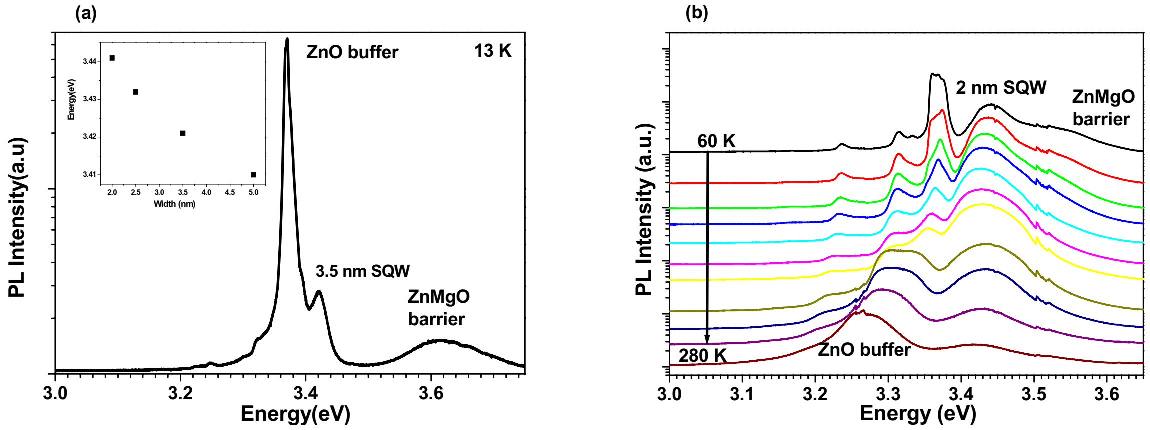

Figure 5.10: *(a) Photoluminescence spectrum obtained from a sample with 3.5 nm quantum well (QW). A very narrow QW peak is noticed at 3.421 eV. The quantum size effect was also notable (see inset). (b) Temperature-resolved PL measurement on a sample with 2 nm quantum well. The QW peak appears at 3.44 eV and exists above 280 K.*

Together with three other samples with quantum well widths of 2, 2.5 and 5 nm, the corresponding emitted energy was noted and plotted as a function of well width in the inset on Figure 5.10a. Taking the effective mass of electron and holes to be $m_e=0.28m_0$ and $m_h=0.59m_0$, respectively, the emitted energies were calculated as in [35] for the same well width. The calculated values were larger than the measured values, with a discrepancy ranging from 1% for the 5 nm quantum well to 10% for the 2 nm quantum well. This effect has been reported for quantum well structures [35]. Temperature-resolved PL measurements between 60 and 280 K show the QW peak around 3.44 eV with very slight red shift for increasing temperature. A relatively slow thermal quenching of the quantum well peak as opposed to the ZnO D^0X peak is additional evidence of quantum structures [195].

In order to check the possibility of quantum confinement emanating from quantum well structures unintentionally grown directly on the 6H-SiC substrate, the post-growth of a 2 nm quantum well structure was carried out on a nanorod sample with a free SiC area, i.e., a section covered with nanorods and the other section is simply the SiC surface. A very thin layer was also observed on the SiC surface after the quantum well growth. This surface was characterised separately using photoluminescence. The absence of a peak which completely rules out the possibility of quantum confinement from structures on the SiC surface. Moreover, starting the growth of $Zn_{0.85}Mg_{0.15}O$ directly on 6H-SiC without accommodating for lattice mismatch would not lead to a $Zn_{0.85}Mg_{0.15}O$ layer of high crystal quality and minimal surface roughness that can hold subsequent layers and guarantee a sharp interface.

Even though good quality ZnO/$Zn_{0.85}Mg_{0.15}O$ heterostructures would not grow on the (11-20) plane of c-axis oriented nanorods, the possibility of a cap-like growth of the quantum well structures on the top end of the ZnO nanorods does not rule out.

5.5. Recombination dynamics in ZnO/ZnMgO SWQs

The recombination dynamics, essential for the lasing, is governed by the carrier transfer toward the active region and the balance between radiative and nonradiative processes, dependent on structural defects. For the wurtzite ZnO QWs, where the defect density may be significant, different decay times of PL have been reported so far, from very fast ~ tens of picoseconds up to hundreds of picoseconds in multiple QW structures3. Thus the intrinsic PL decay time constant in the ZnO QWs is not well established. It is worth mentioning that the decay of the QW PL has been previously considered as a single exponential process [187], while bulk ZnO exhibits a biexponential decay with characteristic decay times of t_1 1 ns and t_2 14 ns for the fast and slow components, respectively [196].

The possibility to achieve room temperature stimulated emission in a ZnO/ZnMgO separate confinement double heterostructure (DHS) having such SQW as an active region and analyze conditions which are necessary for that is to be prove. The study has been performed using a TRPL spectroscopy at 1.8 K, and PLE described before (section 3.00).Lasing properties were investigated using a 266 nm line of the 4th harmonic of a modelocked Nd: yttrium aluminum garnet laser. The optical cavity for lasing was formed by cleaved facets in a similar way for all samples. The laser beam was focused into a stripe on the surface of the 0.8–1.0 mm long samples, while the stimulated emission was detected from the cleaved edge.

Two sets of the SQW samples have been grown on (0001) Al_2O_3 [112]. The first set consists of the simple SQW structures, while the second comprises the DHSs. Both types of structures show full width at half maximum values in a w-scan for the (0002) reflex in the range of 25-36 arcsec. Beginning investigation of the SQWs, which comprise a high temperature MgO nucleation layer providing a two-dimensional growth mode of the following part of the structure, and a 200-nm-thick ZnO buffer capped with a 100-nm-thick ZnxMg1−xO layer with the Mg content of 0.13–0.15. The wells with width varied from 1.0 to 5.0 nm were inserted in the center of the top layer. Selected spectra of the low temperature PL measured in the SQWs are presented in Figure 5.11a.

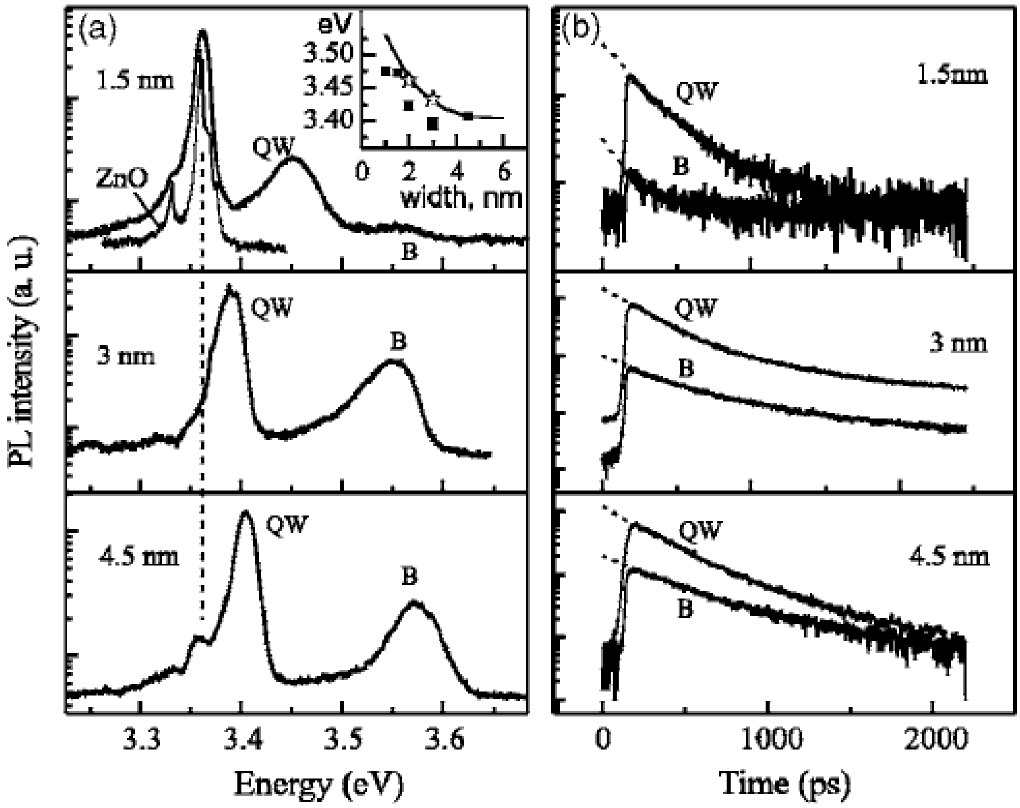

Figure 5.11: *PL spectra measured in SQWs of different widths. "QW," "B,"and "ZnO" denote emission from the well, barrier, and ZnO interface layer, respectively. The Mg content is 15% in the 1.5 and 3 nm QWs and 14% in the 4.5 nm QW. The inset presents a calculated well-width dependence of the exciton energy shown together with experimental PL (squares) and PLE (stars) data. (b) PL decay curves corresponding to the QW and B peaks. Thedotted lines are fits done with the following fast and slow times, t1 / t2 (ns):(1.5 nm) QW (0.2/1.8), B (0.2/3); (3 nm)QW (0.25/ 1.6), B (0.3/1.5); (4.5 nm) QW (0.25/ 0.7), B (0.3/1). (PLE and PL decay measurements by Prof. A. Toropov, Ioffe Institute, St. Petersburg, Russia)*

These structures are thin; therefore, the PL in the ZnO buffer can be excited when the carrier capture in the QW is inefficient, like in the narrow 1.0–1.5 nm QWs. The energy of the SQW PL bands exhibits a gradual lower-energy shift with the increase in the QW width. By compare the experimental data with the exciton energies calculated within the envelope wave-function approximation, using a variational approach with a single-parameter variational function for a quasi-two-dimensional exciton in a rectangular QW.

The ratio of the conduction- and valence-band discontinuities is taken as 0.65:0.35; other material parameters are taken as in Ref. [197]. One can see that the calculated dependence is generally consistent with the experimental points (Figure 5.11a, inset). The agreement is quite good for the exciton peaks in absorption, which are reproduced by the PLE spectra. Some dispersion in the data is related to certain inaccuracy in the determination of the well width and Mg content in the ZnMgO barrier as well as strain, which was not taken into account.

Figure 5.11b presents the characteristic decay curves monitored within either QW or barrier emission peaks. The PL decay is obviously not exponential. Here a fit done using two exponents is presented, like it has been done previously for the bulk material,4 with the slow characteristic time t_2 also being in the nanosecond range. In the thinnest wells (1–1.5 nm) the main part of the QW emission rapidly decays with the fast time t_1=100–200 ps. In the wider wells (2–3 nm), t_1 is as long as 250–350 ps. This value, being among the longest reported[187], evidences the improved material quality. With the further increase of the well width up to 4.5 nm, the decay again starts to be faster, presumably due to strain-induced deterioration of the structural quality. The highest ratio of the QW-to-barrier emission intensities has been observed simultaneously with the fastest decay of the barrier emission, which is suggestive of the efficient carrier transfer to the well (see, e.g., the 1.5 nm QW). However, the PL intensity is maximum with the well width of 2–3 nm, which corresponds approximately to the maximum exciton binding energy.6 These findings permit us to conclude that such 2–3 nm width is the best choice for the SQW DHSs lasers. The structures have been designed for optical pumping. They comprise a 15-nm-thick ZnO buffer layer followed by a 120–290 nm-thick Zn0.82Mg0.18O cladding layer and a 105-nm-thick Zn0.91Mg0.09O waveguide layer. The 2 or 3 nm wide SQW were inserted into this top layer at a distance of 60–65 nm from the surface. The low-temperature (20 K) PLE spectra of these structures clearly demonstrate a pronounced excitonic peak, which confirms their high quality Figure 5.12a. The stimulated emission has been recorded at room temperature at a threshold excitation power density of about 650 kW/cm^2. The small volume of the single QW is responsible for the relatively high threshold. In the case of multiple QWs of similar structural quality, it can be significantly lowered. The stimulated emission appears at ~3.20 eV, while the excitonic feature in the room-temperature PLE spectrum is near 3.38 eV (Figure 5.12). Such an energy separation is higher than anticipated for any reported mechanism [198]. Note that the lasing in the ZnO buffer layer is excluded due to its small thickness (15 nm) in DHSs. Presumably, the lasing recombination process involves the localized states in the QW.

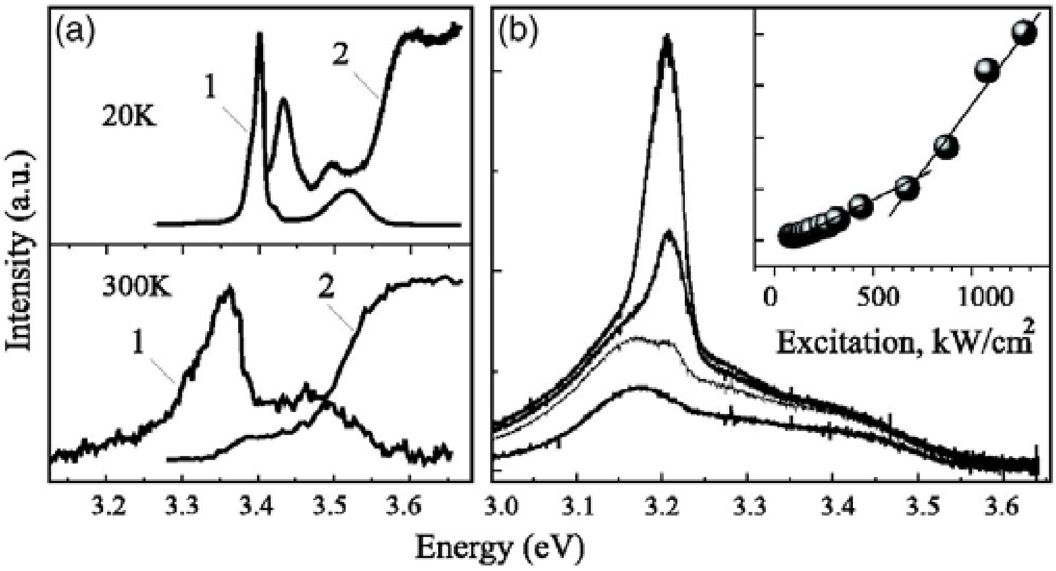

Figure 5.12: (*a) PL (1) and PLE (2) spectra measured in a 3 nm SQW DHS. The room temperature PLE spectrum is monitored from the "green" PL peak (2.393 eV) for the sake of better resolution. (b) RT spectra of stimulated emission measured at the excitation power density (from bottom to top): 436, 674, 872, and 1079 kW/cm2. The inset presents the PL intensity dependence on the excitation power.(Pl, and PLE measurements by Prof. A. Toropov, Ioffe Institute, St. Petersburg, Russia)*

The lasing is achieved in the 3 nm QW DHS, but not achieved in the 2 nm one. The TRPL images registered in the time domain of 2.2 ns (Figure 5.13) exhibit the basic reason for that. In the 2 nm QW sample, the PL bands from both barrier and well are broadened and partly overlap. The overlapping distribution of the densities of states in the QW and barrier permits not only the capture of carriers from the barrier to the QW but also the reverse process-tunneling of carriers from the QW to the barrier states. At room temperature the thermal escape of carriers from the deeper states makes the situation dramatically worse. A preliminary TEM study reveals in this 2 nm QW DHS numerous inversion domains, with a density an order of magnitude higher than that in the 3 nm structure. Respectively, the intensity of the x-ray diffraction peak decreases twice in both θ-2θ, and ω-scans with insignificant broadening, which indicates structural deterioration induced by the inversion domains. It has been previously demonstrated [199], that the intersection of inversion domains with QWs produces specific carrier localization sites, since the growth rate and, consequently, the well widths are different for the materials of opposite polarity. This results in a fluctuating potential profile, because even one monolayer width variation can shift the exciton energy up to 30 meV in the 2 nm QW.

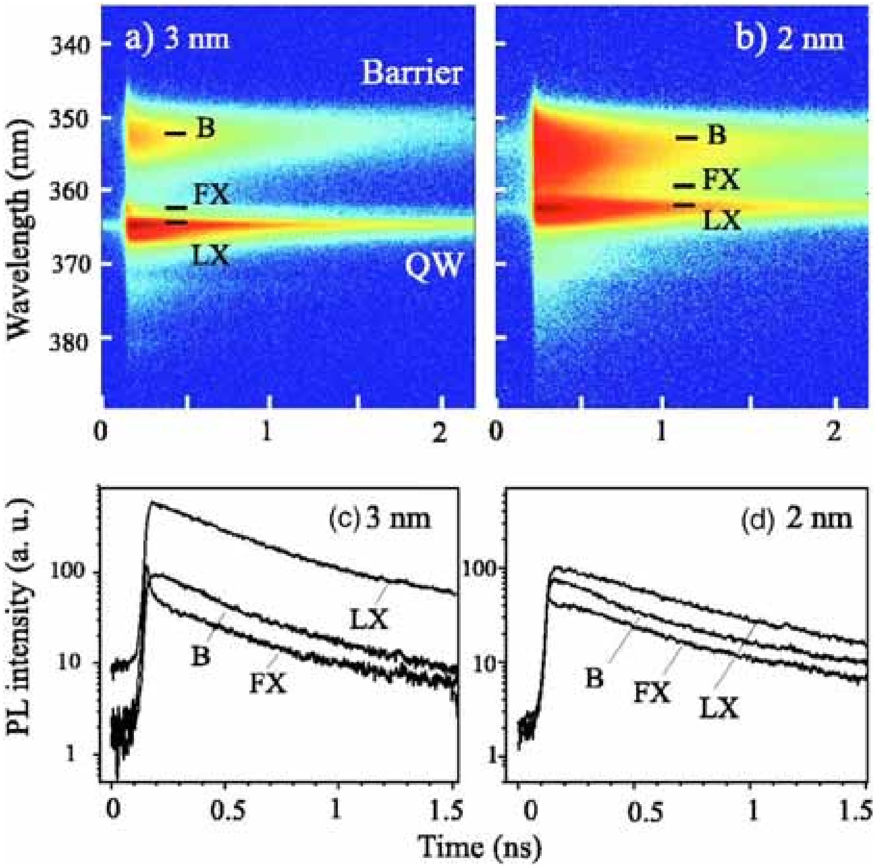

Figure 5.13: *TRPL images (a) and (b) and selected decay curves (c) and (d) ecorded in the 3 and 2 nm SQW DHSs at the wavelengths marked as B, FX, and LX in the images. For the 3(2) nm well they correspond to: B [3.514 (3.497) eV], FX 3.420(3.457) eV], and LX [3.400(3.424) eV]. (TRPL and PL decay measurements by Prof. A. Toropov, Ioffe Institute, St. Petersburg, Russia)*

Strongly different recombination dynamics in these two DHSs had observed. Figures 5.13c and 5.13d show the decay of the emission in the barriers (B) and QWs at the energies corresponding to free (FX) and localized (LX) excitons. These exciton states were identified by temperature dependent PL measurements, as it was previously reported[200]. The temporal evolution of the emission in the 3nm QW satisfies the scenario of an efficient carrier transport toward the LX states. Namely, the FX intensity drops significantly in the time domain of ~50 ps, while the LX intensity rises during this time. The barrier emission intensity is an order of magnitude lower than that in the well. This indicates that the excited excitons are captured by the QW rather than recombine within the barrier. On the contrary, in the 2 nm QW structure, the respective PL intensities differ only by a factor of 2, and the decay curves at the selected energies are almost similar, presumably, due to the overlapped distributions of the localized states in the QWs and barriers. In our experiments with the 1.0–4.5 nm SQWs, Features characteristic for the strong quantumconfined Stark effect has not observed, such as the QW

PL lines below the bulk ZnO band[201] and a spectral shift of the PL maximum in the TRPL images due to the screening of the fields by photoexcited carriers.

It has been demonstrated previously that in the case of low Mg composition the intrinsic electric fields are weak [202]. Indeed, the maximal shift of the exciton energy induced by the intrinsic electric fields can hardly exceed 10 meV for 3 nm wide QW with 12% Mg in the barrier. It is worth noting that with the weak fields much larger optical gain can be realized to promote lasing. In summary, the recombination dynamics in the SQWs which are wider than the exciton Bohr radius resembles that in the bulk material. A small energy dispersion of radiative states, low defect density, and efficient carrier transfer toward an active region are the key prerequisites to obtain stimulated emission at room temperature in the ZnO/ZnMgO SQW DHS with low Mg content in barriers.

6. Summary

In semiconductor research a reliable epitaxial growth technique for growing high quality thin films and heterostructures is necessary. In the case of ZnO one of the main difficulties is the absence of suitable substrate material for ZnO epitaxial growth. Although special oxide material (for example $ScAlMgO_4$) and ZnO bulk crystal can serve as lattice matched substrates, the quality of the substrates themselves, the size of the available wafer, and the expense do not encourage to use these lattice matched substrates for ZnO epitaxial growth. In the current research, a widely used low cost commercial substrate sapphire was employed to develop a reliable epitaxial growth technique and growth process for ZnO. The versatile epitaxial growth technique, molecular beam epitaxy (MBE) equipped with a rf-plasma source was developed for growth and various characterizations methods were conducted to obtain a fundamental understanding in both the epitaxial processes and material properties of ZnO thin films and heterostructures.

Employing a thin HT MgO buffer layer prior to ZnO growth is the key to overcome the very large mismatches between c-Al_2O_3 substrate. Wetting the surface of Al_2O_3 substrate with a few MgO monolayers, lowed the surface energy, so that the lateral growth of ZnO is promoted at the initial growth stage. MgO can be grown in the same chamber as ZnO without any contamination problem. These advantages make the growth procedure of a HT MgO buffer fast and easy. The growth temperature and the growth rate of MgO buffer are found to be important to improve the ZnO heteroepitaxy. An intermediate spinel layer in epitaxial relation with the sapphire substrate as well as with the HT MgO buffer layer is formed in the early stage of growth during the deposition of the MgO at 700°C. It was found that the combination of these two layers is useful for the progressive reduction of the ZnO overgrown with the sapphire substrate.Annealing experiments reveal that as soon as the spinel layer is formed at about 700°C, it remains stable at least up to 1000°C, and even it is extended in thickness.

By recording and analyzing RHEED intensity oscillations, the growth kinetics has been investigated. Flat surface morphology and layer-by-layer growth has been achieved. The stoichiometry has been deduced by analyzing the growth rate as a function of Zn and O fluxes for various growth temperatures. It is found that the sticking coefficient of oxygen radicals is less dependent on the substrate temperature than that of Zn. The stoichiometric condition shifts to larger Zn flux at higher growth temperature. The kink r_{ZnO} values determine the activated O-flux supplied by the RF plasma source at T_{S}=500°C, 400W and a given O_2-flow rate. It equals 0.5±0.05 Ås^{-1} per sccm. Absolute α_{Zn} values versus T_S, defined as $\alpha_{Zn}=r_{ZnO}(T)/r_{ZnO}(max)$, where $r_{ZnO}(max)$ is recalculated from the Zn flux measured by a quartz monitor, using Zn/ZnO molar mass and density ratios.

Ex-situ characterization of the grown ZnO layers indicate that the surface morphology and crystal quality of the ZnO films grown on sapphire by MBE using either oxygen plasma cell or H_2O_2 as an oxidant can be extensively improved by using an HT MgO buffer.

ZnO layers reveal strong variation of surface morphology versus the O/Zn flux ratio. The most flat surface morphology of ZnO is obtained when the ratio is within the 0.7-1 range. The growth under O-rich conditions leads to formation of hexagonal pyramids and at higher O/Zn ratios to a 3D growth with the top layer formed by perfectly c-oriented columnar structures of 50-100 nm in a diameter. It was also possible to recover the initial 3D growth mode to the 2D one by employing the Zn-rich growth conditions at O/Zn=0.4-0.6.

Structural characterizations by high resolution X-ray diffraction (HR-XRD) and transmission electron microscopy (TEM) indicate a dramatic reduction in defect density in the ZnO epilayers grown with an HT MgO buffer. By using TEM, it was found that the dominant extending defects are edge, screw and mixed-type dislocations along c-axis. The main defects were threading dislocations. This is resulted from the well controlled layer-by-layer growth, since only the edge-type dislocation is able to accommodate the lattice mismatch, while the screw type dislocation forms much related to the initial nucleation environment.The microstructure of ZnO epilayers has been studied by HR-XRD. The full width at half maximum of the (0002) reflection, 0.007 degree, is much smaller than that of the (10-10) reflection, 0.27 degree revealing the micro-twist dominates the mosaicity, while micro-tilt is much less important.This pronounced difference of the rocking curve widths between the (0002) and (1010) reflections strongly indicates that the density of pure edge threading dislocations is greater than that of pure screw dislocations.

Optical characterizations reveal that exciton plays an important role in ZnO. At room temperature free exciton recombinations dominate the photoluminescence. The ZnO epilayers reveal well resolved low temperature PL excitonic spectra with a dominant bound exciton $D_2^0X_A$ line (3.355 eV) possessing a ~2 meV half-width and a peak of free A exciton at 3.374 eV. The low-energy tail extending from the excitonic emission peaks due to the lattice deformation is significantly reduced, which allows the observation of two electron satellites and LO-phonons replicas of free and bound excitons. Variation of growth stoichiometry from O-rich to Zn-rich results in the pronounced quench of the acceptor-bound part of the excitonic band, as well as the strong intensity redistribution of donor-bound lines which seems to be attributed to a change in the point defect density. Temperature dependence of PL spectra between 6K and room temperature every 30 K under the same excitation conditions was performed. Slowly decreases coming at 300K to about one third of the intensity at 6K. This corresponds to the activation of non-radiative channels in the capturing and recombination processes. This result was confirm by decay time measurements. PL mapping of 2 inch ZnO epilayer shows high lateral homogeneity from PL intensity distribution and PL FWHM distribution.

Hall-effect measurements and Electrochemical profiling (ECV) were used to characterize the electrical properties of ZnO samples. Hall-effect measurements indicated n-type behavior with carrier concentration of 2.0x10^{16} cm^{-3} and mobility of approximately 96 cm^{2}/Vs. ECV profile versus depth measured for the top 2.5 μm thick sample gives surface carrier concentration is 2.0x10^{16} cm^{-3} increasing to a maximum value of 1.0x10^{18} cm^{-3} the semiconductor/substrate interface.

P-n heterojuntions and mesa structures comprising MBE n-ZnO layers and CVD p-4H-SiC laser were manufactured and investigated. Electrical properties of the mesa diodes have been studied with Hall measurements, and current-voltage measurements (I-V). I-V measurements of the device show good rectifying behavior, from which a turn-on voltage of about 2 V was obtained.

With the excitation of O and N gas mixture in a single plasma cell, followed by the sample annealing procedure. P-type ZnO:N layers with a net hole concentration 3x10^{17} cm^{-3} using was measured. The combination of low growth temperature, slightly O-rich conditions and post-growth annealing is shown to be effective way to obtain p-doping. Further efforts are necessary to improve structural quality of the low-temperature p-type ZnO:N films.

Optical properties of ZnO based II-VI heterostructures and quantum structures have also been studied. The surface roughness of ZnxMg$_{1-x}$O was as low as 0.7 nm. The optical band gap and photoluminescence peak can be turned to larger energy with the same high crystallinity and without significant change in the lattice constant. The prominent PL peaks related to the SQW show a systematic blueshift with decreasing well width, which is consistent with the quantum size effect. The SQW-related emission peaks exhibit an *S*-shaped (redshift-blueshift-redshift) behaviour with increasing temperature, which is in contrast with that ascribed to band gap shrinkage (redshift). The observed behavior is discussed in terms of localization at lateral interface potential fluctuations. For T >70 K the integrated PL intensity is thermally activated with activation energies much less than the band offsets. It is argued that the dominant mechanism leading to the quenching of the ZnO SQW-related PL is due to the thermionic emission of excitons out of the lateral potential minima caused by potential fluctuations, such as interface fluctuations by 1 ML. Stimulated emission has been achieved at room temperature in a separate confinement double heterostructure having a 3 nm wide SQW as an active region. It has been found that a critical parameter for the lasing is the inhomogeneous broadening of both QW and barrier emission bands.

MBE process for ZnO has been developed where high quality ZnO epilayers and heterostructures can be grown by molecular beam epitaxy on sapphire substrate. For nitrogen doping of ZnO, Oxygen and nitrogen were activated in the single plasma cell. No reproducible and reliable experimental results on the achievement of p-type conductivity achieved. Stimulated emission has been achieved at room temperature.

7. List of references

[1] Anderson Janotti and Chris G. Van de Walle: Absolute deformation potentials and band alignment of wurtzite ZnO, MgO, and CdO; Phys. Rev. B, **75**, 121201(R)(2007).

[2] L. Gerward and J. S. Olsen: The High-Pressure Phase of Zincite, J. Synchrotron Radiat. **2**, 233 (1995).

[3] H. Karzel et al: Lattice dynamics and hyperfine interactions in ZnO and ZnSe at high external pressures, Phys. Rev. B **53**, 11425(1996).

[4] R. R. Reeber: Lattice parameters of ZnO from 4.2 to 296 K; J. Appl. Phys. **41**, 5063 (1970).

[5] S. Desgreniers: High-density phases of ZnO: Structural and compressive parameters; Phys. Rev. B **58**, 14 102 (1998).

[6] M. Catti, Y. Noel, and R. Dovesi: Full piezoelectric tensors of wurtzite and zinc blende ZnO and ZnS by first-principles calculations; J. Phys. Chem. Solids **64**, 2183 (2003).

[7] C. G Van de Walle: Defect analysis and engineering in ZnO; Physica B **308-310**, 899 (2001).

[8] Anderson Janotti and Chris G. Van de Walle: Native point defects in ZnO; Phys. Rev. B 76, 165202 (2007)

[9] A. Janotti and C. G. Van de Walle: Oxygen vacancies in ZnO; Appl. Phys. Lett. **87**, 122102 (2005).

[10] J. G. Lu, Y. Z. Zhang, Z. Z. Ye, Y. J. Zeng, H. P. He, L. P. Zhu, J. Y. Huang, L. Wang, J. Yuan, B. H. Zhao, and X. H. Li: Control of p- and n-type conductivities in Li-doped ZnO thin films; Appl. Phys. Lett. **89**, 112113 (2006).

[11] A. Valentini, F. Quaranta, M. Rossi, and G. Battaglin: preparation and characterization of Li doped ZnO films; J. Vac. Sci. Technol. A **9**, 286 (1991).

[12] Z.Q. Ma, W.G. Zhao and Y. Wang: Electrical properties of Na/Mg co-doped ZnO thin films; Thin Solid Films; **515**, 8611 (2007).

[13] T. Kryshtab, V. S. Khomchenko, V. B. Khachatryan, N. N. Roshchina, J. A. Andraca-Adame,O. S. Lytvyn, V. I. KushnirenkoEffect of doping on properties of Zno:Cu and Zno: Ag thin films; J Mater Sci; Mater Electron **18**,1115 (2007).

[14] C. H. Park, S. B. Zhang, and S. H. Wie: Origin of p-type doping difficulty in ZnO: The impurity perspective, Phys. Rev. B 66, 073202 (2002).

[15] F. X. Xiu, Z. Yang, L. J. Mandalapu, J. L. Liu, and W. P. Beyermann: p-type ZnO films with solid-source phosphorus doping by molecular-beam epitaxy; Appl. Phys. Lett. **88**, 052106 (2006).

[16] Y. R. Ryu, S. Zhu, D. C. Look, J. M. Wrobel, H. M. Jeong, and H. W.White: Synthesis of p-type ZnO films; J. Cryst. Growth, **216**, 330 (2000).

[17] F. X. Xiu, Z. Yang, L. J. Mandalapu, D. T. Zhao, and J. L. Liu, and W. P. Beyermann: High-mobility Sb-doped p-type ZnO by molecular-beam epitaxy; Phys. Lett. **87**, 152101 (2005).

[18] R.M. Park, M.B. Troffer, and C. M. Rouleau: p-type ZnSe by nitrogen atom beam doping during molecular beam epitaxial growth; Appl. Phys. Lett., 57, 2127 (1990).

[19] J. E. Jaffe, J. A. Snyder, Z. Lin and A. C. Hess: LDA and GGA calculations for highpressure phase transitions in ZnO and MgO; Phys. Rev. B **62**, 1660(2000).

[20] J. R. Chelikowsky: An oxygen pseudopotential: Application to the electronic structure of ZnO; Sol. Stat. Comm. **22**, 351 (1977).

[21] S. Bloom and I. Ortenburger: Pseudopotential band structure of ZnO; Phys. Stat. Sol. (b) **58**, 561 (1973).

[22] M. Usuda, N. Hamada, T. Kotani and M. van Schilfgaarde: All-electron GW calculation based on the LAPWmethod: Application to wurtzite ZnO; Phys. Rev. B **66**, 125101 (2002).

[23] B. K. Meyer, H. Alves, D. M. Hofmann, W. Kriegseis, D. Forster, F. Bertram, J. Christen, A. Hoffmann, M. Straburg, M. Dworzak, U. Haboeck and A. V. Rodina: Bound exciton and donor-acceptor pair recombination in ZnO; Phys. Stat. Sol. (b) **241**, 231 (2004).

[24] H. Yoshikawa and S. Adachi: Optical constants of ZnO; Jpn. J. Appl. Phys. **36**, 6237 (1997).

[25] N. Ashkenov, Mbenkum B, M, C. Bundesmann, V. Riede, M. Lorenz, D. Spemann, E. M. Kaidashev, A. Kasic, M. Schubert, M. Grundmann, G. Wanger, H. Neumann, V. Darakchieva, H. Arwin and B. Monemar: Infrared dielectric functions and phonon modes of high-quality ZnO films; J. Appl. Phys. **93**, 126 (2003).

[26] X. W. Sun and H. S. Kwok: Optical properties of epitaxially grown zinc oxide films on sapphire by pulsed laser deposition; J. Appl. Phys. **86**, 408 (1999).

[27] S. J. Pearton, D. P. Norton, K. Ip, Y. W. Heo and T. Steiner: Recent progress in processing and properties of ZnO; Prog. in Mater. Sci. **50**, 293 (2005).

[28] C.F. Klingshirn: Semiconductor Optics, Springer-Verlag, (1997).

[29] Mang, K. Reimann and St. Riibenacke: Solid State Commun., **94**, 251 (1 995)

[30] D. G. Thomas: The exciton spectrum of zinc oxide; J. Phys. Chem. Solids **15**, 86 (1960).

[31] F. Z. Wang, H. P. He, Z. Z. Ye, and L. P. Zhu: Photoluminescence properties of quasialigned ZnCdO nanorods; J. Appl. Phys., **98**, 084301(2005).

[32] L. Vaillant, O. Vigil, G. Contreras-Puente, and C. Mejia-Garcia: Optical and morphological characterization of $(ZnO)_{(x)}(CdO)_{(1-x)}$ thin films; Modern Physics Letters B, **15**, 663 (2001).

[33] B. S. Zou, V. V. Volkov, and Z. L. Wang: Optical properties of amorphous ZnO, CdO, and PbO nanoclusters in solution; Chemistry of Materials, **11**, 3037(1999).

[34] S. E. Paje, J. Llopis, M. E. Zayas, E. Rivera, A. Clark, and J. M. Rincon: Photoluminescence in ZnO-CdO-SiO2 Glasses; Applied Physics A - Materials Science & Processing, **54**, 239 (1992).

[35] T. Gruber, C. Kirchner, R. Kling, F. Reuss, and A. Waag: ZnMgO epilayers and ZnO-ZnMgO quantum wells for optoelectronic applications in the blue and UV spectral region; Appl. Phys. Lett., **84**, 5359 (2004).

[36] M. Fujita, R. Suzuki, M. Sasajima, T. Kosaka, Y. Deesirapipat, and Y. Horikoshi: Molecular beam epitaxial growth of ZnMgO/ZnO/ZnMgO single quantum well structure on Si (111) substrate; Journal of Vacuum Science & Technology B, **24**, 1668 (2006).

[37] C. W. Sun, P. Xin, Z. W. Liu, and Q. Y. Zhang: Room-temperature photoluminescence of ZnO/MgO multiple quantum wells on Si (001) substrates; Appl. Phys. Lett., **88**, 221914 (2006).

[38] V. A. Coleman, M. Buda, H. H. Tan, C. Jagadish, M. R. Phillips, K. Koike, S. Sasa, M. Inoue, and M. Yano: Observation of blue shifts in ZnO/ZnMgO multiple quantum well structures by ion-implantation induced intermixing; Semiconductor Science and Technology, **21**, L25 (2006).

[39] S. H. Park, K. J. Kim, S. N. Yi, D. Ahn, and S. J. Lee: Optical gain in wurtzite ZnO/ZnMgO quantum well lasers; Jap. J. Appl. Phys. Part 2- Letters & Express Letters, **44**, L1403 (2005).

[40] T. Makino, K. Tamura, C. H. Chia, Y. Segawa, M. Kawasaki, A. Ohtomo, and H. Koinuma: Photoluminescence properties of ZnO epitaxial layers grown on lattice-matched ScAlMgO4 substrates; J. Appl. Phys., **92**, 7157 (2002).

[41] H. D. Sun, T. Makino, N. T. Tuan, Y. Segawa, Z. K. Tang, G. K. L. Wong, M. Kawasaki, A. Ohtomo, K. Tamura, and H. Koinuma: Stimulated emission induced by exciton-exciton scattering in ZnO/ZnMgO multiquantum wells up to room temperature; Appl. Phy. Lett. , **77,** 4250 (2000).

[42] T. Makino, C. H. Chia, N. T. Tuan, H. D. Sun, Y. Segawa, M. Kawasaki, A. Ohtomo, K. Tamura, and H. Koinuma: Room-temperature luminescence of excitons in ZnO/(Mg, Zn)O multiple quantum wells on lattice-matched substrates; Appl. Phys. Lett. **77**, 975 (2000).

[43] A. Ohtomo, M. Kawasaki, I. Ohkubo, H. Koinuma, T. Yasuda, and Y. Segawa: Structure and optical properties of ZnO/Mg0.2Zn0.8O superlattices; Appl. Phys. Lett., **75**,980 (1999).

[44] K. Koike, K. Hama, I. Nakashima, S. Sasa, M. Inoue, and M. Yano: Molecular beam epitaxial growth of Al-doped ZnMgO alloy films for modulation-doped ZnO/ZnMgO heterostructures; Japanese Journal of Applied Physics Part 1 - Regular Papers Short Notes & Review Papers, **44**, 3822 (2005).

[45] T. Makino, Y. Segawa, M. Kawasaki, A. Ohtomo, R. Shiroki, K. Tamura,T. Yasuda, and H. Koinuma: Band gap engineering based on MgxZn1−xO and $Cd_yZn_{1-y}O$ ternary alloy films; Appl. Phys. Lett., **78**, 1237 (2001).

[46] S.von Molnar and D.Read: New materials for semiconductor spin-electronics, Proc.IEEE, **91**, 715 (2003).

[47] T. Dietl, H. Ohno, F. Matsukura, J.Cibert and D. Ferrand: Electrical Manipulation of Magnetization Reversal in a Ferromagnetic Semiconductor; Science **287**, 1019 (2000).

[48] T. Dietl: Ferromagnetic semiconductors; Semicond. Sci. Technol., **17**, 377 (2002).

[49] S. J. Pearton, C. R. Abernathy, M. E. Overberg, G. T. Thaler, D. P. Norton, N. Theodoropoulou, A. F. Hebard, Y. D. Park, F. Ren, J. Kim and L. A. Boatner: Wide band gap ferromagnetic semiconductors and oxides; J. Appl. Phys. **93**, 1(2003).

[50] K. Sato and H. Katayama-Yoshida: First principles materials design for semiconductor spintronics; Semicond.Sci.Technol.**17**, 367 (2002).

[51] Y. Matsumoto, M. Murakami, T. Shono, T. Hasegawa, T. Fukumura, M. Kawasaki, P. Ahmet, T. Chikyow, S. Koshihara, and H. Koinuma: Room-Temperature Ferromagnetism in Transparent Transition Metal-Doped Titanium Dioxide; Science, **291**, 854 (2001).

[52] H.Saeki, H.Tabata, and T.Kawai: Magnetic and electric properties of vanadium doped ZnO films; Solid-State Commun. **120**, 439 (2001).

[53] A. Che Mofor, A. El-Shaer, A. Bakin, and A. Waag, H. Ahlers, U. Siegner, S. Sievers, and M. Albrecht, W. Schoch, N. Izyumskaya, and V. Avrutin, S. Sorokin and S. Ivanov, J. Stoimenos: Magnetic property investigations on Mn-doped ZnO Layers on sapphire; Appl. Phys. Lett. **87**, 062501 (2005).

[54] D. C. Look, B. Claflin, Y. I. Alivov and S. J. Park: The future of ZnO light emitters; Phys. Stat. Sol. (a) **201**, 2203 (2004).

[55] V. A. Coleman, J. E. Bradby, C. Jagadish, P.Munroe, Y.W. Heo, S. J. Pearton, D. P. Norton, M. Inoue and M. Yano: Mechanical properties of ZnO epitaxial layers grown on a- and caxis sapphire; Appl. Phys. Lett. **86**, 203 105 (2005).

[56] A. Dal Corso, M. Posternak, R. Resta and A. Baldereschi: Ab initio study of piezoelectricity and spontaneous polarization in ZnO; Phys. Rev. B **50**, 10 715 (1994).

[57] M. Catti, Y. Noel and R. Dovesi: Full piezoelectric tensors of wurtzite and zincblende ZnO and ZnS by first-principles calculations; J. Phys. Chem. Sol. **64**, 2183 (2003).

[58] A. R. Hutson: Piezoelectricity and conductivity of ZnO and CdS; Phys. Rev. Lett. **4**, 505 (1960).

[59] Y. Noel, M. Llunell, R. Orlando, P. D Arco and R. Dovesi: Performance of various Hamiltonians in the study of the piezoelectric properties of crystalline compounds: The case for BeO and ZnO, Phys. Rev. B **66**, 214107 (2002).

[60] R.R. Reeber: Lattice parameters of ZnO from 4.2° to 296°K; J. Appl. Phys., **41**, 5063 (1970).

[61] L. Liao, J. C. Li, D. F. Wang, C. Liu, C. S. Liu, Q. Fu and L. X. Fan: Field emission property improvement of ZnO nanowires coated with amorphous carbon and carbon nitride films; Nanotech. **16**, 985 (2005).

[62] Y. Xia, P. Yang, Y. Sun, Y. Wu, B. Mayers, B. Gates, Y. Yin, F. Kim and H. Yan: Onedimensional nanostructures: Synthesis, characterization, and applications; Adv. Mat. **15**, 353 (2003).

[63] Z. L. Wang: Zinc oxide nanostructures: growth, properties and applications; J. Phys. Cond. Mat. **16**, R829 (2004).

[64] D. J. Sirbuly, M. Law, H. Q. Yan and P. D. Yang:Semiconductor nanowires for subwavelength photonics integration; J. Phys. Chem. B **109**, 15 190 (2005).

[65] J. G. E. Gardeniers, Z. M. Rittersma and G. J. Burger: Preferred orientation and piezoelectricity in sputtered ZnO films; J. Appl. Phys. **83**, 7844 (1998).

[66] D. P. Norton, S. J. Pearton, A. F. Hebard, N. Theodoropoulou, L. A. Boatner and R. G. Wilson: Ferromagnetism in Mg-implanted ZnO:Sn single crystals; Appl. Phys. Lett. **82**, 239 (2003).

[67] H. Hartnagel, A. L. Dawar, A. K. Jain and C. Jagadish, Semiconducting transparent thin films, Institute of Physics Publishing, Bristol and Philadelphia, (1995).

[68] C. Coskun, D. C. Look, G. C. Farlow and J. R. Sizelove: Radiation hardness of ZnO at low temperatures; Semicond. Sci. Technol. **19**, 752 (2004).

[69] M. A. Herman: Physical problems concerning effusion processes of semiconductors in molecular beam epitaxy; vacuum, **32**, 555 (1982).

[70] A. Madhukar: Far from equilibrium vapour phase growth of lattice matched III–V compound semiconductor interfaces: Some basic concepts and monte-carlo computer simulations; Surf. Sci. **132**, 344 (1983).

[71] M. A. Herman, H. Sitter: Molecular Beam Epitaxy, fundamental and current status; Springer-Verlag Berlin Heidelberg (1989).

[72] King-Ning Tu, James W. Mayer, and Leonard C. Feldman: Electronic Thin Film Science for Electrical Engineers and Materials Scientists; Macmillan, New York, (1992).

[73] J. A. Venables: Introduction to surface and thin film processes; Cambridge University Press (2000).

[74] J. H. Neave, P. J. Dobson, B. A. Joyce, and J. Zhang: Reflection high-energy electron diffraction oscillations for vicinal surface – a new approach to surface diffusion measurements; Appl. Phys. Lett. **47**, 100 (1985).

[75] T. Shitara, D. D. Vvdensky, M. R. Wilby, J. Zhang, J. H. Neave, and B. A. Joyce: Step-density variations and reflection high-energy electron-diffraction intensity oscillations during epitaxial growth on vicinal GaAs (001); Phys. Rev. B **46**, 6815 (1992).

[76] B. Voigtländer, T. Weber, P. Smilauer, and D. E. Wolf: Transition from island growth to step-flow growth for Si/Si(100) epitaxy; Phys. Rev. Lett. **78**, 2164 (1997).

[77] R.A. Swalin: Thermodynamics of solids. New York, John Wiley & Sons (1972).

[78] J.F. O'Hanlon: A User's Guide to Vacuum Technology. New York, John Wiley & Sons, (1989).

[79] A. Cho: Film Deposition by Molecular-Beam Techniques; J. Vac. Sci. Technol., **8**, S31 (1971).

[80] Y. Cho and J. R. Arthur: Molecular beam epitaxy. Progress in Solid State Chemistry, **10**, 157 (1975).

[81] K. Motzfeldt: The thermal decomposition of sodium carbonate by the effusion method; J. Phys. Chem., **59**, 139 (1955).

[82] D.R. Lide (Ed.), CRC Handbook of Chemistry and Physics, 79th Edition. CRC Press, Boca Raton, FL, (1998–1999).

[83] K. Nakahara, T. Tanabe, H. Takasu, P. Fons, K. Iwata, A. Yamada, K. Matsubara, R. Hunger, S. Niki: Growth of Undoped ZnO Films with Improved Electrical Properties by Radical Source Molecular Beam Epitaxy; Jpn. J. Appl. Phys. **40**, 250 (2000).

[84] K. Sakurai, D. Iwata, Sz. Fujita, Sg. Fujita: Growth of ZnO by Molecular Beam Epitaxy Using NO2 as Oxygen Source; Jpn. J. Appl. Phys. **38**, 2606 (1999).

[85] M. Fujita, N. Kawamoto, T. Tatsumi, K. Yamagishi, Y. Horikoshi: Molecular Beam Epitaxial Growth of ZnO on Si Substrate Using Ozone as an Oxygen Source; Jpn. J. Appl. Phys. **42**, 67 (2003).

[86] A.B.M.A. Ashrafi, I. Suemune, H. Kumano, and K. Uesugi: Growth Activation of ZnO Layers with H_2O Vapor on a-Face of Sapphire Substrate by Metalorganic Molecular-Beam Epitaxy; phys. stat. sol. (a) **192**, 224 (2002).

[87] W. Braun, “Applied RHEED,” Springer-Verlag (1999).

[88] K. Britze and G. Meyer-Ehmsen: High energy electron diffraction at Si(001) surfaces; Surf. Sci. **77**, 131 (1978).

[89] M. Itoh: Relation between surface reconstructions and RHEED intensity oscillations; Phys. Rev. B **58**, 6716 (1998).

[90] X. Zeng, B. Lin, I. El-Kholy, and H. Elsayed-Ali: Time resolved structural study of the Ge(111) high-temperature phase transition; Surf. Sci. **439**, 95 (1999).

[91] J. Y. Lee, J. Y. Juang, J. H. Ou, Y. F. Chen, K. H. Wu, T. M. Uen, and Y. S. Gou: RHEED intensity oscillations in homoepitaxial growth of SrTiO3 films; Physica B, **284-288**, 2099 (2000).

[92] K. Inumaru, T. Ohara, S. Yamanaka: Pulsed laser deposition of epitaxial titanium nitide on MgO(001) monitored by RHEED oscillation; Appl. Surf. Sci. **158**, 375 (2000).

[93] Z. Mitura and J. L. Beeby: Theoretical studies on the quantitative interpretation of RHEED data; J. Phys. Condens. Matter **8**, 8717 (1996).

[94] J. E. Mahan, K. M. Geib, G. Y. Robinson, and R. G. Long: A review of the geometrical fundamentals of reflection high-energy electron diffraction with application to silicon surfaces; J. Vac. Sci. Technol. A, **8**, 3692 (1990).

[95] J. H. Neave, B. A. Joyce, P. J. Dobson and N. Norton: Dynamics of film growth of GaAs by MBE from Rheed observations; Appl. Phys. A, **31**, 1 (1983).

[96] J. M. Van Hove, C. S. Lent, P. R. Pukite and P. I. Cohen: Damped oscillations in reflection high energy electron diffraction during GaAs MBE; J. Vac. Sci. & Technol. B, **1**, 741 (1983).

[97] T. Shitara, J. Zhang, J. H. Neave, B. A. Joyce: Ga adatom incorporation kinetics at steps on vicinal GaAs (001) surfaces during growth of GaAs by molecular beam epitaxy; J. Appl. Phys. **71**, 4299 (1992).

[98] G. Binning, C. Quate, C. Gerber: Atomic Force Microscope; Physical Review Letters, **56**, 930 (1986).

[99] G. Binnig, Ch. Gerber, E. Stoll, T. R. Albrecht and C. F. Quate: Atomic Resolution with Atomic Force Microscope; Europhysics. Lett. **3**, 1281 (1987).

[100] Dawn Bonnell: Scanning Probe Microscopy and Spectroscopy: Theory, Techniques, and the Applications; Wiley-VCH, (2001).

[101] M. Knoll: Aufladepotentiel und Sekundäremission elektronenbestrahlter Körper; Z tech. Phys. 16, 467 (1935).

[102] P. F. Fewster: High-resolution diffraction-space mapping and topography; Appl. Phys. A **58**, 121 (1994).

[103] V. Holy, U. Pietsch, and T. Baumbach: High-Resolution X-Ray Scattering from ThinFilms and Multilayers; Springer Tracks in Modern Physics, Springer-Verlag Berlin Heidelberg (1999).

[104] Williams D.B., Carter C.B: Transmission Electron Microscopy; Plenum Press, New York, (1996).

[105] Born M., Wolf E: Principles of optics; Cambridge University Press, 7 edition (1999).

[106] T. Ambridge and M.M. Faktor: An automatic carrier concentration profile plotter using an electrochemical technique; J. Appl. Electrochem. **5**, 319(1975).

[107] A. Tsukazaki, M. Kubota, A. Ohtomo, T. Onuma, K. Ohtani, H. Ohno, S. F. Chichibu, and M. Kawasaki: Blue light-emitting diode based on ZnO; Jap. J. Appl. Phys. **44**, L643 (2005)

[108] N. Izyumskaya, V. Avrutin, W. Schoch, A. El-Shaer, F. Reuß,Th. Gruber, A. Waag, Molecular beam epitaxy of high-quality ZnO using hydrogen peroxide as an oxidant, Journal of Crystal Growth **269**, 356 (2004).

[109] A. El-Shaer, A. Che Mofor, A. Bakin, M. Kreye, A. Waag. High-Quality ZnO Layers Grown by MBE on Sapphire , Superlattices and Microstructures, Elsevier, **38**, 265 (2005).

[110] A. El-Shaer, A. Bakin, A. Che Mofor, M. Kreye, A. Waag, M. Heuken, J. Bläsing, A. Krost, J. Stoimenos H_2O_2-Molecular Beam Epitaxy of high quality ZnO , Applied Physics A: Materials Science & Processing **88**, 57 (2007).

[111] A. El-Shaer, A. Bakin, A. Che Mofor, J. Bläsing, A. Krost, J. Stoimenos, B. Pécz, M. Kreye, M. Heuken, and A. Waag CBE Growth of High-Quality ZnO Epitaxial Layers, phys. stat. sol. (b) **243**, 768 (2006).

[112] A. Bakin, A. El-Shaer, A. Che Mofor, M. Kreye, A. Waag, F. Bertram, J. Christen, J. Stoimenos. MBE growth of ZnO layers on sapphire employing hydrogen peroxide as an oxidant , J. Crystal Growth **287**, 7 (2006).

[113] A. El-Shaer, A. Bakin, M. Al-Suleiman, S. Ivanov, A. Che Mofor and A. Waag: Layer by layer growth of ZnO on (0001) sapphire substrates by radical-source molecular beam epitaxy, Superlattices and Microstructures, Elsevier **42**, 158 (2007).

[114] S.V. Ivanov, A. El-Shaer, T.V. Shubina, S.B. Listoshin, A. Bakin, and A. Waag Growth kinetics and properties of ZnO/ZnMgO heterostruc-tures grown by radical-source molecular beam epitaxy; phys. stat. sol. (c) **4**, 154 (2007).

[115] Y. Chen, H.-J. Ko, S.-K. Hong, T. Yao, Y. Segawa: Two-dimensional growth of ZnO films on sapphire (0001) with buffer layers; J. Crystal Growth **214/215**, 87 (2000).

[116] Agus Setiawan , Hang Ju Ko , Soon Ku Hong , Yefan Chen , Takafumi Yao: Study on MgO buffer in ZnO layers grown by plasma-assisted molecular beam epitaxy on Al_2O_3(0001); Thin Solid Films **445**, 213 (2003).

[117] H. Kato, K. Miyamoto, M. Sano, T. Yao: Polarity control of ZnO on sapphire by varying the MgO buffer layer thickness; Appl. Phys. Lett. **84**, 4562 (2004).

[118] S. Sadofev, S. Blumstengel, J. Cui, J. Puls, S. Rogaschewski, P. Schäfer, Yu. G. Sadofyev, and F. Henneberger, Appl. Phys. Lett. **87**, 091903 (2005).

[119] Z.Q. Zeng, Y.Z. Liu, H.T. Yuan, Z.X. Mei, X.L. Du, J.F. Jia, Q.K. Xue, Z. Zhang: Surface modification of MgAl2O4 (111) for growth of high-quality ZnO epitaxial films;Appl. Phys. Lett. **90**, 081911 (2007).

[120] J.W. Matthews and A.E. Blakeslee: Defects in epitaxial multilayers: I. Misfit dislocations; J. Cryst. Growth **27**, 118 (1974).

[121] H. Heinke, V. Kirchner, S. Einfeldt, and D. Hommel: Analysis of the Defect Structure of Epitaxial GaN; Phys. Status Solidi A **176**, 391 (1999).

[122] S.V. Ivanov, S.V. Sorokin, P.S. Kop'ev, J.R. Kim, H.D. Jung, H.S. Park: Composition, stoichiometry and growth rate control in molecular beam epitaxy of ZnSe based ternary and quaternary alloys; J.Cryst. Growth **159**, 16 (1996).

[123] H.-J. Ko, T. Yao, Y. Chen, S.-K. Hong: Investigation of ZnO epilayers grown under various Zn/O ratios by plasma-assisted molecular-beam epitaxy; J. Appl. Phys. **92**, 4354 (2002).

[124] S. Ivanov, S. Sorokin, I. Krestnikov, N. Faleev, B. Ber, I. Sedova, Yu. Kudryavtsev, P. Kop'ev: Interplay of kinetics and thermodynamics in molecular beam epitaxy of (Mg,Zn,Cd)(S,Se); J. Cryst. Growth **184/185**, 70 (1998).

[125] B. Pécz, A. El-Shaer, A. Bakin, A. C. Mofor,A. Waag, J. Stoemenos: characterization of ZnO films grown by molecular beam epitaxy on sapphire with MgO buffer, J. Appl. Phys. **100**, 103506 (2006).

[126] B. Heying, X. H. W, S. Keller, Y. Li, D. Kapolnek, B. P. Keller, S. P. DenBaars, & J. S. Speck: Role of threading dislocation structure on the x-ray diffraction peak widths in epitaxial GaN films; Appl. Phys. Lett. **68**, 643 (1996).

[127] W. Mattews and A. E. Blakeslee: Defects in epitaxial multilayers: I. Misfit dislocations; J. Cryst. Growth **27**, 118 (1974).

[128] A. Fischer, H Kühne, and H. Richter: New Approach in Equilibrium Theory for Strained Layer Relaxation; Phys. Rev. Lett. **73**, 2712 (1994).

[129] A. Ohtomo, M. Kawasaki, T. Koida, K. Masubuchi, and H. Koinuma, Y. Sakurai and Y. Yoshida, T. Yasuda and Y. Segawa: $Mg_xZn_{1-x}O$ as a II–VI widegap semiconductor alloy; Appl. Phys. Lett. **72**, 2466 (1998).

[130] A. Ohtomo, R. ShirokiI, I. Ohkubo, H. Koinuma, and M. Kawasaki: Thermal stability of supersaturated $Mg_xZn_{1-x}O$ alloy films and $Mg_xZn_{1-x}O$/ZnO heterointerfaces; Appl.Phys. Lett. **75**, 4088 (1999).

[131] A. Bakin, J. Kioseoglou. Pecz, A. El-Shaer, A.-C. Mofor, J. Stoemenos and A. Waag. Misfit reduction by a spinel layer formed during the epitaxial growth of ZnO on sapphire using a MgO buffer layer , J. Crystal Growth, **308** , 314 (2007).

[132] P.B. Hirsch, A. Howie, R.B. Nicholson, D.W. Pashley, Electron Microscopy of Thin Crystals, Butterworths, London, (1965).

[133] P.A. Stadelmann: EMS - a software package for electron diffraction analysis and HREM image simulation in materials science; Ultramicroscopy **21**, 131(1987).

[134] J.J. Comer, N.C. Tombes, J.F. Fitzgerald: Growth of Single-Crystal and Polycrystalline Thin Films of $MgAl_2O_4$ and $MgFe_2O_4$; J. Am. Ceram. Soc. **49**, 237 (1966).

[135] L. Navias: Preparation and Properties of Spinel Made by Vapor Transport and Diffusion in the System $MgO-Al_2O_3$; J. Am. Ceram. Soc. **44**, 434 (1961).

[136] R.C. Rossi, R.M. Fulrath: Oxygen Diffusion in Magnesium Aluminate Spinel; J. Am. Ceram. Soc. **64**, 368 (1981).

[137] R.E. Carter: Mechanism of Solid-state Reaction Between Magnesium Oxide and Aluminum Oxide and Between Magnesium Oxide and Ferric Oxide; J. Am. Ceram. Soc. **44**, 116 (1961).

[138] H. Sieber, D. Hesse, X. Panb, S. Senz, J. Heydenreich, Z. Anorg. Allg. Chem. 622, 1658 (1996).

[139] D.C. Reynolds, D.C. Look, B. Jogai, C.W. Litton, T.C. Collins, W. Harsch, G. Cantwell: Neutral-donor–bound-exciton complexes in ZnO crystals; Phys. Rev. B, **57**, 12151 (1998).

[140] .K. Thonke, Th. Gruber, N. Teofilov, R. Schonfelder, A. Waag, R. Sauer: Donor–acceptor pair transitions in ZnO substrate material; Physica B, 308-310, 945 (2001).

[141] S. B. Zhang, S. H. Wei, and Alex Zunger: Intrinsic n-type versus p-type doping asymmetry and the defect physics of ZnO; Physical Review B, **63**, 075205 (2001).

[142] D.C. Look, R.J. Molnar: Degenerate layer at GaN/sapphire interface: Influence on Hall-effect measurements; Apll. Phys. Lett. 70, 3377(1997).

[143] Y. Marfain, A. Lusson: Doping engineering of p-type ZnO; Superlat. & Microstr. **38**, 385 (2005).

[144] X. D. Chen, C. C. Ling, S. Fung, C. D. Beling, Y. F. Mei, Ricky K. Y. Fu, G. G. Siu, and Paul. K. Chu: Current transport studies of ZnO/p-Si heterostructures grown by plasma immersion ion implantation and deposition; Appl. Phys. Lett. **88**, 132104 (2006).

[145] QIN Qi, GUO Li-Wei, ZHOU Zhong, CHEN Hong, DU Xiao-long, MEL Zeng-Xia, JIA Jin-Feng, XUE Qi-Kum, and ZHOU JunMing Chin. Phys. Lett. **22**, 2298 (2005).

[146] Ya. Alivov, E. V. Kalinina, A. E. Cherenkov, D. C. Look, B.M. Ataev, A. K. Omaev, M. V. Chukichev, and D. M. Bagnall: Fabrication and characterization of n-ZnO/p-

AlGaN heterojunction light-emitting diodes on 6H-SiC substrates; Appl. Phys. Lett. **83**, 4719 (2003).

[147] Ya. Alivov, J. E. Van Nostrand, D. C. Look, M. V. Chukichev, and B. M. Ataev: Observation of 430 nm electroluminescence from ZnO/GaN heterojunction light-emitting diodes; Appl. Phys. Lett. 83, 2943(2003).

[148] Julio A. Aranovich, Dolores Golmyo, Alan L. Fahrebruch, and Richard H. Bube: Photovoltaic properties of ZnO/CdTe heterojunctions prepared by spray pyrolysis; J. Appl. Phys., **51**, 4260 (1980).

[149] Cheng-Xin Wang, Guo-Wei-Yang, Hong-Wu Liu, Yong-Hao Han, Ji-Feng Luo, Chun-Xiao Gao, and Guang-Tian Zou : Experimental analysis and theoretical model for anomalously high ideality factors in ZnO/diamond p-n junction diode; Appl. Phys. Lett. **84**, 2427 (2004).

[150] Clement Yuen, S. F. Yu, S. P. Lau, Rusli, and T. P. Chen: Fabrication of n-ZnO: Al/p-SiC (4H) heterojunction light-emitting diodes by filtered cathodic vacuum arc technique; Appl. Phys. Lett. **86**, 241111 (2005).

[151] Ya. I. Alivov, Ü. Özgür, S. Dogan, D. Johnstone, V. Avrutin, N. Onojima, C. Liu, J. Xie, Q. Fan, and H. Morkoc : Photoresponse of n-ZnO/p-SiC heterojunction diodes grown by plasma-assisted molecular-beam epitaxy; Appl. Phys. Lett. **86**, 241108 (2005).

[152] R. L. Anderson: Experiments on Ge-GaAs heterojunctions; Solid-state Electronics **5**, 341 (1962).

[153] G. Wagner, K. Irmscher: Influence of the Growth Conditions on the Layer Parameters of 4H-SiC Epilayers Grown in a Hot-Wall Reactor; Mater. Sci. Forum **353-356**, 95 (2001).

[154] A. B. M. Almamun Ashrafi, Bao-ping Zhang, Naguyen Thanh Binh, Kazuki Wakatsuki and Yusaburo Segawa : High-Quality ZnO Layers Grown on 6H-SiC Substrates by Metalorganic Chemical Vapor Deposition ; Jap. J. Appl. Phys. **43**, 1114 (2004).

[155] S. J. Pearton, D. P. Norton, K. Ip, Y. W. Heo, and T. Steiner: Recent advances in processing of ZnO; J. Vac. Sci. Technol. B **22**, 932 (2004).

[156] K. Lorenz, M. Gonsalves, W. Kim, V. Narayanan, and S. Mahajan: Bistable output from a coupled-resonator vertical-cavity laser diode; Appl. Phys. Lett. **77**, 3391(2000).

[157] N. Y. Garces, L. Wang, N. C. Giles, L. E. Halliburton, G. Cantwell, and D. B. Eason: Molecular nitrogen ($N\bar{2}$) acceptors and isolated nitrogen (N^-) acceptors in ZnO crystals J. Appl. Phys. **94**, 519 (2003).

[158] D. C. Look, D. C. Reynolds, C. W. Litton, R. L. Jones, D. B. Eason, and G. Cantwell: Characterization of homoepitaxial p-type ZnO grown by molecular beam epitaxy; Appl. Phys. Lett. **81**, 1830(2002).

[159] Weizhong Xu, Zhizhen Ye, Ting Zhou, Binghui Zhao, Liping Zhu, Jingyun Huang: Low-pressure MOCVD growth of p-type ZnO thin films by using NO as the dopant source; J. Cryst. Growth **265**, 133 (2004).

[160] W. Z. Xu, Z. Z. Ye, Y. J. Zeng, L. P. Zhu, B. H. Zhao, L. Jiang, J. G. Lu, and H. P. He and S. B. Zhang: ZnO light-emitting diode grown by plasma-assisted metal organic chemical vapor deposition; Appl. Phys. Lett. **88**, 173506 (2006).

[161] Y. Yan, S. B. Zhang, and S. T. Pantelides: Control of Doping by Impurity Chemical Potentials: Predictions for p-Type ZnO; Phys. Rev. Lett., **86**, 5723 (2001).

[162] S. V. Ivanov, A. El-Shaer, T. V. Shubina, S. B. Listoshin, A. Bakin, A. Waag: Growth kinetics and properties of ZnO/ZnMgO hetero- structures grown by radical-source molecular beam epitaxy; phys. stat. sol. (c), **4**, 154 (2007).

[163] V.V. Ratnikov, R.N. Kyutt, T.V. Shubina, T Paskova, and B Monemar: Determination of microdistortion components and their application to structural characterization of HVPE GaN epitaxial layers J. Phys. D: Appl. Phys. **34**, A30 (2001).

[164] J.W. Sun, Y.M. Lu, Y.C. Liu, D.Z. Shen, Z.Z. Zhang, B.H. Li, J.Y. Zhang, B. Yao, D.X. Zhao, X.W. Fan : The activation energy of the nitrogen acceptor in p-type ZnO film grown by plasma-assisted molecular beam epitaxy; Solid State Communications **140**, 345 (2006).

[165] S.J. Jiao, Y.M. Lu, D.Z. Shen, Z.Z. Zhang, B.H. Li, Zh.H. Zheng, B. Yao, J.Y. Zhang, D.X. Zhao and X.W. Fan :Donor–acceptor pair luminescence of nitrogen doping p-type ZnO by plasma-assisted molecular beam epitaxy ; J. of Luminescence **122-123**, 368 (2007).

[166] Ü. Özgür, Ya. I. Alivov, C. Liu, A. Teke, M. A. Reshchikov, S. Doğan, V. Avrutin, S.-J. Cho, and H. Morkoc: A comprehensive review of ZnO materials and devices; J. Appl. Phys., **98**, 041301 (2005).

[167] H. W. Liang, Y. M. Lu, D. Z. Shen, Y. C. Liu, J. F. Yan, C. X. Shan, B. H. Li, Z. Z. Zhang, J. Y. Zhang, X. W. Fan: P-type ZnO thin films prepared by plasma molecular beam epitaxy using radical NO; phys. stat. sol. (a) **202**, 6, 1060 (2005).

[168] S. Limpijumnong, X. Li, S.-H. Wei, and S. B. Zhang : Substitutional diatomic molecules NO, NC, CO, N2, and O2: Their vibrational frequencies and effects on p doping of ZnO; Appl. Phys. Lett. **86**, 211910 (2005).

[169] H. D. Sun, Y. Segawa, M. Kawasaki, A. Ohtomo, K. Tamura, and H. Koinuma: Phonon replicas in ZnO/ZnMgO multiquantum wells; Journal of Applied Physics, **91**, 6457 (2002).

[170] H. D. Sun, T. Makino, Y. Segawa, M. Kawasaki, A. Ohtomo, K. Tamura, and H. Koinuma: Enhancement of exciton binding energies in ZnO/ZnMgO multiquantum wells; Journal of Applied Physics, **91**, 1993 (2002).

[171] T. Makino, Y. Segawa, M. Kawasaki, and H. Koinuma: Optical properties of excitons in ZnO-based quantum well heterostructures; Semiconductor Science and Technology, **20**, S78 (2005).

[172] F. Kreller, J. Puls, and F. Henneberger: Temperature-dependent study of optical gain in (Zn,Cd)Se/ZnSe multiple-quantum-well structures; Applied Physics Letters, **69**, 2406 (1996).

[173] F. Y. Jen, Y. C. Lu, C. Y. Chen, H. C. Wang, C. C. Yang, B. P. Zhang, and Y. Segawa: Ultrafast biexciton dynamics in a ZnO thin film; Applied Physics Letters, **87**, 072103 (2005).

[174] S. Adachi:Polarization and wave-vector-dependent measurements by four-wave mixing in ZnO: valence-band ordering and biexcitons; Journal of Luminescence, **112**, 34 (2005)

[175] K. Hazu, T. Sota, K. Suzuki, S. Adachi, S. F. Chichibu, G. Cantwell, D. B. Eason, D. C Reynolds, and C. W. Litton: Strong biexcitonic effects and exciton-exciton correlations in ZnO; Physical Review B, **68**, 033205 (2003).

[176] J. A. Davis, L. Van Dao, X. M. Wen, P. Hannaford, V. A. Coleman, H. H. Tan, C. Jagadish, K. Koike, S. Sasa, M. Inoue, and M. Yano: Observation of coherent biexcitons in ZnO/ZnMgO multiple quantum wells at room temperature; Applied Physics Letters, **89**, 182109 (2006).

[177] K. Ogata, K. Koike, T. Tanite, T. Komuro, F. Yan, S. Sasa, M. Inoue, M. Yano: ZnO and ZnMgO growth on *a*-plane sapphire by molecular beam epitaxy; J. Crystal Growth **251**, 623 (2003).

[178] P. Y. Yu and M. Cardona: Fundamentals of Semiconductors-physics and Materials properties, third ed. Berlin: Springer-Verlag, (2005).

[179] B. D. Yacobi: Semiconductor Materials-An Introduction to Basic Principles. New York: Kluwer Academic /Plenum Publishers, (2003).

[180] O. Manasreh: Semiconductor Heterojunctions and Nanostructures. New York: McGraw Hill (2005).

[181] J. A. Wang, U. A. Griesinger, F. Adler, H. Schweizer, V. Harle, and F. Scholz: Size effect upon emission dynamics of 1.5 μm quasi-quantum wire distributed feedback semiconductor lasers; Applied Physics Letters, **69**, 287 (1996).

[182] R. Heitz, O. Stier, I. Mukhametzhanov, A. Madhukar, and D. Bimberg: Quantum size effect in self-organized InAs/GaAs quantum dots; Physical Review B, **62**, 11017 (2000).

[183] M. V. Maximov, A. F. Tsatsul'nikov, B. V. Volovik, D. A. Bedarev, Y. M. Shernyakov, I. N. Kaiander, E. Y. Kondrat'eva, A. E. Zhukov, A. R. Kovsh, N. A. Maleev, S. S. Mikhrin, V. M. Ustinov, Y. G. Musikhin, P. S. Kop'ev, Z. I. Alferov, R. Heitz, N. N. Ledentsov, and D. Bimberg: Optical properties of quantum dots formed by activated spinodal decomposition for GaAs-based lasers emitting at similar to 1.3μm; Microelectronic Engineering,**51**, 61 (2000).

[184] T. Winzell, I. Maximov, L. Landin, Y. Zhang, A. Gustafsson, L. Samuelson, and H. J. Whitlow: Bandgap modification in GaInAs/InP quantum well structures using switched ion channelling lithography; Semiconductor Science and Technology, **16**, 889 (2001).

[185] C. Jagadish, G. Li, M. B. Johnston, and M. Gal: Si and C delta-doping of GaAs grown by metal organic vapour phase epitaxy for fabrication of nipi doping superlattices; Materials Science and Engineering B - Solid State Materials for Advanced Technology, **51**,103 (1998).

[186] L. Fu, R. W. van den Heijden, H. H. Tan, C. Jagadish, L. V. Dao, and M. Gal: Study of intermixing in a GaAs/AlGaAs quantum-well structure using doped spin-on silica layers; Applied Physics Letters, **80**, 1171 (2002).

[187] B. P. Zhang, N. T. Bihn, K. Wakatsuki, C. Y. Liu, Y. Segawa, and N. Usami: Growth of ZnO/MgZnO quantum wells on sapphire substrates and observation of the two-dimensional confinement effect; Appl. Phys. Lett. **86**, 032105 (2005).

[188] Augustine Che Mofor: Fabrication and Characterisation of Device Quality ZnO Nanostructures , PhD thesis (2007)

[189] Y.-H. Cho, G. H. Gainer, A. J. Fisher, J. J. Song, S. Keller, U. K. Mishra, and S. P. Den Baars: "S-shaped" temperature-dependent emission shift and carrier dynamics in InGaN/GaN multiple quantum wells; Appl. Phys. Lett. **73**, 1370 (1998).

[190] Semiconductor Optics, 2nd ed. C. Klingshirn, Springer-Verlag Berlin (2005).

[191] Y. P. Varshni: Temperature dependence of the energy gap in semiconductors; Physica (Utrecht) **34**, 149 (1967).

[192] P. Zhou, H. X. Jian, R. Bannwart, S. A. Solin, and G. Bai: Excitonic transitions in GaAs-AlxGa1-xAs multiple quantum wells affected by interface roughness; Phys. Rev. B **40**, 11862 (1989).

[193] A. Waag, S. Schmeusser, R. N. Bicknell-Tassius, D. R. Yakovlev, W. Ossau, G. Landwehr, and I. N. Uraltsev: Molecular beam epitaxial growth of ultrathin CdTe–CdMnTe quantum wells and their characterization; Appl. Phys. Lett. **59**, 2995 (1991).

[194] A. C. Mofor, A. El-Shaer, M. Suleiman, A. Bakin, A. Waag: A two-step obtainment of quantum confinement in ZnO nanorods; Nanotechnology **17**, 4859 (2006)

[195] T. Yatsuia, J. Lim and M. Ohtsub), S. J. An, and G.-C. Yi: Evaluation of the discrete energy levels of individual ZnO nanorod single-quantum-well structures using near-field ultraviolet photoluminescence spectroscopy; Appl. Phys. Lett. **85**, 727 (2004)

[196] S. F. Chichibu, A. Uedono, A. Tsukazaki, T. Onuma, M. Zamfirescu, A. Ohtomo, A. Kavokin, G. Cantwell, C. W. Litton, T. Sota, and M. Kawasaki: Exciton-polariton spectra and limiting factors for the room-temperature photoluminescence efficiency in ZnO; Semicond. Sci. Technol. **20**, S67 (2005).

[197] G. Coli and K. K. Bajaj: Excitonic transitions in ZnO/MgZnO quantum well heterostructures; Appl. Phys. Lett. **78**, 2861 (2001).

[198] C. Klingshirn, R. Hauschild, J. Fallert, and H. Kalt: Room-temperature stimulated emission of ZnO: Alternatives to excitonic lasing; Phys. Rev. B **75**, 115203 (2007).

[199] T. V. Shubina, A. A. Toropov, V. N. Jmerik, M. G. Tkachman, A. V. Lebedev, V. V. Ratnikov, A. A. Sitnikova, V. A. Vekshin, S. V. Ivanov, P. S. Kop’ev, P. Bigenwald, J. P. Bergman, P. O. Holtz, and B. Monemar: Intrinsic electric fields in N-polarity GaN/AlxGa1-xN quantum wells with inversion domains; Phys. Rev. B **67**, 195310 (2003).

[200] T. Makino, N. T. Tuan, H. D. Sun, C. H. Chia, Y. Segawa, M. Kawasaki, A. Ohtomo, K. Tamura, T. Suemoto, H. Akiyama, M. Baba, S. Saito, T. Tomita, and H. Koinuma: Temperature dependence of near ultraviolet photoluminescence in ZnO/(Mg, Zn)O multiple quantum wells; Appl. Phys. Lett. **78**, 1979 (2001).

[201] C. Morhain, T. Bretagnon, P. Lefebvre, X. Tang, P. Valvin, T. Guillet, B. Gil, T. Taliercio, M. Teisseire-Doninelli, B. Vinter, and C. Deparis: Internal electric field in wurtzite $ZnO/Zn_{0.78}Mg_{0.22}O$ quantum wells; Phys. Rev. B **72**, 241305R (2005).

[202] S.-H. Park and D. Ahn: Spontaneous and piezoelectric polarization effects in wurtzite ZnO/MgZnO quantum well lasers; Appl. Phys. Lett. **87**, 253509 (2005).

8. Publications and conference contributions

Publications as main author

1. A. El-Shaer, A. Bakin, M. Al-Suleiman, S. Ivanov, A. Che Mofor and A. Waag: Growth of wide band gap wurtzite ZnMgO epilayers on (0001)Al_2O_3 by radical-source molecular beam epitaxy, Superlattices and Microstructures, Elsevier Volume 42, Issues 1-6, Pages 129-133 (2007).

2. A. El-Shaer, A. Bakin, M. Al-Suleiman, S. Ivanov, A. Che Mofor and A. Waag: Improvement of radical-source molecular beam epitaxial growth of ZnO on (0001) sapphire employing RHEED intensity oscillations, Superlattices and Microstructures, Elsevier Volume 42, Issues 1-6, Pages 158-164 (2007).

3. A. El-Shaer, A. Bakin, E. Schlenker, A. C. Mofor, G. Wagner, S. Reshanov and A. Waag Fabrication and characterization of n-ZnO on p-SiC heterojunction diodes on 4H-SiC substrates, Superlattices and Microstructures, Elsevier Volume 42, Issues 1-6, Pages 387-391 (2007).

4. A. El-Shaer, A. Bakin, A. Che Mofor, M. Kreye, A. Waag, M. Heuken, J. Bläsing, A. Krost, J. Stoimenos H_2O_2-Molecular Beam Epitaxy of high quality ZnO , Applied Physics A: Materials Science & Processing 88, 57(2007).

5. A. El-Shaer, A. Bakin, A. Che Mofor, J. Bläsing, A. Krost, J. Stoimenos, B. Pécz, M. Kreye, M. Heuken, and A. Waag CBE Growth of High-Quality ZnO Epitaxial Layers, phys. stat. sol. (b) 243, No. 4, 768–772 (2006).

6. A. El-Shaer, A. Che Mofor, A. Bakin, M. Kreye, A. Waag. High-Quality ZnO Layers Grown by MBE on Sapphire , Superlattices and Microstructures, Elsevier, 38, n. 4-6, pp. 265-271 (2005).

Publications as co-author

1. T. V. Shubina, A. A. Toropov, O. G. Lublinskaya, P. S. Kop'ev, and S. V. Ivanov, A. El-Shaer, M. Al-Suleiman, A. Bakin, and A. Waag, A. Voinilovich, E. V. Lutsenko, and G. P. Yablonskii, J. P. Bergman, G. Pozina, and B. Monemar. Recombination dynamics and lasing in ZnO/ZnMgO single quantum well structures. Appl. Phys. Lett. 91, 201104 (2007).

2. A. Bakin, J. Kioseoglou. Pecz, A. El-Shaer, A.-C. Mofor, J. Stoemenos and A. Waag. Misfit reduction by a spinel layer formed during the epitaxial growth of ZnO on sapphire using a MgO buffer layer , J. Crystal Growth, 308 , 314 (2007)

3. Daniel Hofstetter, Yargo Bonetti, Fabrizio R. Giorgetta, Abdel-Hamid El-Shaer, Andrey Bakin, Andreas Waag, Rüdiger Schmidt-Grund, Mathias Schubert, and Marius Grundmann: Demonstration of an ultraviolet ZnO-based optically pumped 3rd order distributed feedback laser, Appl. Phys. Lett. **91**, 111108 (2007).

4. M. Al-Suleiman, A. El-Shaer, A. Bakin, H.-H.Wehmann and A.Waag ; Optical investigations and exciton localization in high quality Zn1-xMgxO–ZnO single quantum wells, Appl. Phys. Lett. **91**, 081911 (2007).

5. A.Bakin, A. El-Shaer, A.C.Mofor, M. Al-Suleiman, E. Schlenker, B. Postels, M. Kreye, A.Waag: ZnMgO-ZnO Quantum Wells embedded into ZnO Nanopillars: towards realisation of Nano-LEDs, phys. stat. sol. (c) 4, No. 1, 158–161 (2007).

6. V. Petukhov, A.Bakin, A. El-Shaer, A.C.Mofor, and A.Waag; Etch-Pit Density Investigation on Both Polar Faces of ZnO Substrates, Electrochem. Solid-State Lett., Volume 10, Issue 12, pp. H357-H361 (2007)

7. S.V. Ivanov, A. El-Shaer, T.V. Shubina, S.B. Listoshin, A. Bakin, and A. Waag Growth kinetics and properties of ZnO/ZnMgO heterostruc-tures grown by radical-source molecular beam epitaxy , phys. stat. sol. (c) 4, No. 1, 154–157 (2007).

8. A. C. Mofor, A. S. Bakin, A. El-Shaer, D. Fuhrmann, F. Bertram, A. Hangleiter, J. Christen and A. Waag: Vapour Transport Growth of ZnO Nanorods; *Appl. Phys. A*, DOI: 10.1007/s00339-007-3961-5 (2007)

9. A.C. Mofor, F. Reuß, A. El-Shaer, A. Bakin, H. Ahlers, U. Siegner, S. Sievers, M. Albrecht, W. Schoch, N. Izyumskaya, V. Avrutin, J. Stoimenos., and A. Waag: Magnetism in Mn-/V-doped ZnO layers; *Appl. Phys. A* **88** 161-166 (2007)

7. A. C. Mofor, A. Bakin, U. Chejarla, E. Schlenker, A. El-Shaer, G. Wagner, N. Boukos, A. Travlos, and A. Waag: Fabrication of ZnO Nanorod-based *p-n* Heterojunction on SiC Substrate, Superlattices and Microstructures, Elsevier Volume 42, Issues 1-6, *Pages 415-420* (2007).

8. A. Bakin, A. Che Mofor, A. El-Shaer, and A. Waag: Vapour Phase Transport Growth of ZnO Layers and Nanostructures, Superlattices and Microstructures, Elsevier Volume 42, Issues 1-6, Pages 33-39 (2007).

9. A. Bakin, A. El-Shaer, A. Che Mofor, M. Kreye, A. Waag, F. Bertram, J. Christen, J. Stoimenos. MBE growth of ZnO layers on sapphire employing hydrogen peroxide as an oxidant , J. Crystal Growth 287, n. 1, 2006, pp. 7-11.(2006)

10. B. Pécz, A. El-Shaer, A. Bakin, A. C. Mofor,A. Waag, J. Stoemenos: characterization of ZnO films grown by molecular beam epitaxy on sapphire with MgO buffer, J. Appl. Phys. 100, 103506 (2006).

11. A. C. Mofor , A. S. Bakin, A. El-Shaer, D. Fuhrmann, F. Bertram, A. Hangleiter, J. Christen and A. Waag Catalyst-free Vapor-phase transport growth of vertically aligned ZnO nanorods on 6H-SiC and (11-20) Al_2O_3 , *phys. stat. sol.* (c) **3**, pp. 1046 (2006)

12. A. C. Mofor, A. El-Shaer, M. Suleiman, A. Bakin, A. Waag: A two-step obtainment of quantum confinement in ZnO nanorods; *Nanotechnology* **17**, pp. 4859 (2006)

13. M. Al- Suleiman, A. Che Mofor, A. El-Shaer, A.Bakin, H.-H.Wehmann and A.Waag ; Photoluminescence properties: catalyst-free ZnO nanorods and layers versus bulk ZnO Appl. Phys. Lett. 89, 231911 (2006).

14. A.C. Mofor, F. Reuss, A. El-Shaer, H. Ahlers, U. Siegner, A. Bakin, W. Limmer, J. Eisenmenger, Th. Mueller, P. Ziemann, and A. Waag: A Study of ZnMnO as a Material for Magneto- and Spin-electronics; *phys. stat. sol.* (c) **3**, pp. 1104 (2006)

15. A. Che Mofor, A. El-Shaer , A. Bakin, H.-H. Wehmann, A. Waag, H. Ahlers, U. Siegner, S. Sievers, M. Albrecht, W. Schoch, N. Izyumskaya, V. Avrutin, J. Stoimenos. Magnetic Property Investigation on ZnMnO; *Superlatt. Microstruct.* **39**, pp. 381 (2006)

16. B. Piechal, J. Yoo, A. El-Shaer, A. C. Mofor, G.-C. Yi, A. Bakin, A. Waag, F. Donatini, D. Le Si: Cathodoluminescence study of wide band gap ZnO nanorod heterostructures, European Material Research Society Fall meeting, Warsaw Poland 4-8 September (2006).

17. A. C. Mofor , A. S. Bakin, A. El-Shaer, D. Fuhrmann, F. Bertram, A. Hangleiter, J. Christen and A. Waag Catalyst-free Vapor-phase transport growth of vertically aligned ZnO nanorods on 6H-SiC and (11-20) Al_2O_3 , phys. stat. sol. (c) **3**, pp. 1046 (2006).

18. A.C. Mofor, F. Reuss, A. El-Shaer, H. Ahlers, U. Siegner, A. Bakin, W. Limmer, J. Eisenmenger, Th. Mueller, P. Ziemann, and A. Waag: A Study of ZnMnO as a Material for Magneto- and Spin-electronics; phys. stat. sol. (c) **3**, pp. 1104 (2006).

19. V. Avrutin, Ü. Özgür, H. Lee, S. Chevtchenko, and H. Morkoc, M. Callahan, A. El-Shaer, A. Che Mofor, A. Bakin, and A. Waag, N. Izyumskaya, W. Schoch, S. Sorokin and S. Ivanov: Optical studies of ZnO doped with transition metals, Proceedings of SPIE Vol. 6122 (2006).

20. V. Avrutin, N. Izyumskaya, Ü. Özgür, A. El-Shaer, H. Lee, W. Schoch, F. Reuss, V.G. Beshenkov, A.N. Pustovit, A. Che Mofor, A. Bakin, H. Morkoç and A. Waag Optical and electrical properties of ZnMnO layers grown by peroxide MBE , J. Superlattices and Microstructures, Elsevier, V. 39, Iss. 1-4, , pp. 291-29 (2006).

21. A. C Mofor, A. El-Shaer, A. Bakin, and A. Waag, H. Ahlers, U. Siegner, S. Sievers, and M. Albrecht, W. Schoch, N. Izyumskaya, and V. Avrutin, S. Sorokin and S. Ivanov, J. Stoimenos: Magnetic property investigations on Mn-doped ZnO Layers on sapphire; Appl. Phys. Lett. **87**, pp. 062501 (2005).

22. N. Izyumskaya, V. Avrutin, W. Schoch, A. El-Shaer, F. Reuß,Th. Gruber, A. Waag, Molecular beam epitaxy of high-quality ZnO using hydrogen peroxide as an oxidant, Journal of Crystal Growth 269 356–361(2004).

23. B. El-Baradie, R. Ghazy, A. El-Shaer, F. El-Mekawey: Optical selection of the preferred solvent of a standard polymer for laser light scattering phenomena investigations Physica B 292 208-212 (2000)

24. R. Ghazy, B. El-Baradie, A. El-Shaer, F. El-Mekawey: Static light scattering (SLLS) investigations of the scattering parameters of a synthetic polymer, Optics & laser technology 31 447-453 (1999)

25. R. Ghazy, B. El-Baradie, A. El-Shaer, F. El-Mekawey: Measurements of refractive indices and refractive index increment of a synthetic PMMA solutions at 488 nm, Optics & laser technology 31 335-340(1999)

Conference contributions

1. Abdel-Hamid El-Shaer, Vladimir Petukhov, Andrey Bakin, and Andreas Waag; Radical Source Molecular Beam Epitaxy of ZnO Homoepitaxial Layers, The 13th International Conference on II-VI Compounds Jeju, Korea, September 10-14, (2007).

2. T.V. Shubina, A.A. Toropov, O.G. Lublinskaya, S.B. Listoshin, A.A. Sitnikova, A. El-Shaer, M. Al-Suleiman, A. Bakin, A. Waag, A. Voinilovich. Exciton recombination dynamics and lasing in ZnMgO/ZnO single quantum well structures. The 13th International Conference on II-VI Compounds Jeju, Korea, September 10-14, (2007).

3. A. Waag, A. El-Shaer, A. C. Mofor, M. Suleimann, B. Postels, E. Schlenker, H. Wehmann, A. Bakin: MBE-grown ZnMgO-ZnO quantum wells embedded into ZnO nanopillers, Material Research Society (MRS) Conference, Boston, Massachussetts, USA, 27.11−1.12.(2006).

4. A. Che Mofor, A. Bakin, A. El-Shaer, M. Al-Suleiman, N. Boukos , A. Travlos, and A. Waag: VPT Growth of ZnO: From Nanostructures to Layers 4th International Workshop on ZnO and Related Materials, Gießen (2006)

5. A.C. Mofor, A. El-Shaer, M. Suleiman, A. Bakin, A. Waag: Fabrication of ZnO Nanorod-based Single Quantum Well Structures, European Material Research Society Fall meeting, Warsaw Poland 4−8 September (2006).

6. A.Bakin, A. El-Shaer, A.C.Mofor, M. Al-Suleiman, E. Schlenker, B. Postels, M. Kreye, A.Waag: ZnMgO-ZnO Quantum Wells embedded into ZnO Nanopillars: towards realisation of Nano-LEDs, The International Symposium on Blue Laser and Light Emitting Diodes, Montpellier, France, May 15-19 (2006).

7. A. C. Mofor, A. Bakin, A. El-Shaer, E. Schlenker, M. Suleiman, and A. Waag: Growth of ZnO Nanorods for Optoelectronic and Spintroic Applications, German Physics Society Conference, Dresden, March (2006).

8. A. Che Mofor, A. Bakin, A. El-Shaer, M. Al-Suleiman, N. Boukos , A. Travlos, and A. Waag: VPT Growth of ZnO: From Nanostructures to Layers 4th International Workshop on ZnO and Related Materials, Gießen (2006).

9. A.C. Mofor, A. El-Shaer, M. Suleiman, A. Bakin, A. Waag: Fabrication of ZnO Nanorod-based Single Quantum Well Structures, European Material Research Society Fall meeting, Warsaw Poland 4−8 September (2006).

10. A.Bakin, A. El-Shaer, A.C.Mofor, M. Al-Suleiman, E. Schlenker, B. Postels, M. Kreye, A.Waag: ZnMgO-ZnO Quantum Wells embedded into ZnO Nanopillars: towards realisation of Nano-LEDs, The International Symposium on Blue Laser and Light Emitting Diodes, Montpellier, France, May 15-19 (2006).

11. A. Bakin, A. El-Shaer, A. Che Mofor, M. Kreye, A. Waag, F. Bertram, J. Christen, J. Stoimenos: Recent advancements in ZnO layers growth on sapphire; ICMAT 2005, Symposium N, ZnO and Related Materials, Singapore , July 3−9 (2005).

12. A. El-Shaer, A. Bakin, A. C. Mofor, and A. Waag: Molecular-beam epitaxy growth of ZnO on sapphire substrate, 20th Workshop of DGKK- (German Society of Crystal Growth) Group: Duisburg, 8−9. December (2005)

13. A. C. Mofor, A. Bakin, A. El-Shaer, B. Postels, D. Fuhrmann, F.Bertram, A. Hangleiter, J. Christen, and A. Waag: Vapour Phase Transport Growth of ZnO for Nano- and Flexible Electronics, 20th Workshop of DGKK- (German Society of Crystal Growth) Group: Duisburg, 8−9. December (2005).

14. A. Che Mofor, A. El-Shaer , A. Bakin, A. Waag, H. Ahlers, U. Siegner, W. Schoch, N. Izyumskaya, V. Avrutin, S.Sorokin, S.Ivanov J. Stoimenos: Magnetic Property Investigations on MBE-grown ZnMnO layers, EMC Santa-Barbara, (2005).

15. A. El-Shaer, A. Che Mofor, A. Bakin, M. Kreye, A. Waag,_F. Bertram, J. Christen and J. Stoimenos: MBE growth of high quality ZnO layers on sapphire, EMC Santa-Barbara, (2005).

16. A. C. Mofor, A. El-Shaer, A. Bakin, A. Waag, H. Ahlers, U. Siegner, S. Sievers, M. Albrecht, W. Schoch, N. Izyumskaya,V. Avrutin3, and J. Stoimenos. Magnetic Property Investigations On ZnMnO Grown On Sapphire, 12TH INTERNATIONAL CONFERENCE ON II–VI COMPOUNDS, Warsaw, Poland September 12 – 16, 2005

17. F. Bertram, S. Giemsch, J. Christen, A. El-Shaer , A. Bakin, A. Waag. Direct Visualization of the Bound Exciton Distribution of Self-organized Grown ZnO Pyramids by Cathodoluminescence Microscopy , E-MRS 2005, Spring Meeting, Symposium G, ZnO and Related Materials, Strasbourg, May 31-June 3, (2005).

18. A. El-Shaer, A. Che Mofor, A. Bakin, N. Izyumskaya, V. Avrutin, W. Schoch, F. Reuß, A. Waag, H. Ahlers, U. Siegner. Novel Oxidant for ZnO Molecular Beam Epitaxy , Soxess Workshop on ZnO and Related Materials, October 27−30, Caernarfon, United Kingdom, (2004).

19. A. Bakin, A. El-Shaer, N. Izyumskaya, V. Avrutin, W. Schoch, A. Che Mofor, F. Reuß, A. Waag: New approach to molecular beam epitaxy of high-quality ZnO , The 3rd International Workshop on ZnO and Related Materials, October 5−8, Sendai , Japan , (2004).

20. A. El-Shaer, A. Che Mofor, A. Bakin, W. Schoch, F. Reuß, A. Waag: MBE growth of ZnO using H_2O_2 as oxidant; German MBE Workshop 2004 at Physikalisch-Technische Bundesanstalt Braunschweig, 11 - 12 October (2004).

21. A. Bakin, A. El-Shaer, A. Che Mofor, W. Schoch, A. Waag: Growth of High quality ZnO with H_2O_2 as oxidant; 3rd International Workshop on ZnO and Related Materials Sendai, Japan, October 6−8, (2004).

Acknowledgement

I would like to extend deep thanks to my advisor, Prof. Dr. rer. nat. habil. Andreas Waag for accepting me as a PhD student and for showing confidence in my capabilities. He is an exceptional advisor who helped me go through all the difficulties that I encountered in my research.

Special thanks Priv. Doz. Dr. Andrey Bakin. He was always near me at any time to help not only during every stage of this work but also in life. I have appreciated his comments and ideas and his ability to identify the critical questions in this work.

I also thank Prof. Dr.-Ing. Wolfgang Kowalsky of the Institute of High Frequency Engineering for accepting to co-evaluate this thesis.

This work could be obtained only through the assistance of my colleagues in the Institute of Semiconductor Technology, Technical University Braunschweig, Germany where this work was done. Thanks once more to all of them for helping in measurements or for sharing their ideas, specially to Manfred Karsten , Karl-Heinz Lachmund and Doris Rümmler for their technical assistance.

Several materials characteristics were carried out in several laboratories inside and outside Germany through the assistance of many colleagues in the ZnO community. Many thanks go to the collaborators of these laboratories especially my colleagues of the following establishments: Physics Department of Aristotle University of Thessaloniki, Greece, Ioffe Physico-Technical Institute, St. Petersburg, Russia, Hungarian Academy of Sciences, National Centre for Scientific Research (CNRS) Université Joseph Fourier Grenoble France, AIXTRON AG, Aachen, Institute of High-Frequency Engineering and Institute of Applied Physics Technical University Braunschweig, Department of Experimental Physics University of Magdeburg, and Department of Semiconductor Physics, Ulm University.

I am also grateful to the high education ministry in Egypt for giving me a chance to do my PhD in Germany.

The work presented in this thesis was supported by the German Research Community (DFG).

At last, but the most important I would like to thank my wife and my daughters for creating nice family atmosphere that helps me greatly during this work.

Biography

First name: Abdelhamid
Surname: Elshaer
Date of birth: 18.04.1968
Place of birth: Gharbiya, Egypt

10.1975 – 10.1983:	Primary School, Egypt.
10.1983 – 10.1987:	Secondary School, Egypt.
10.1987 – 10.1993:	Obtained Bachelor of Science (B.Sc.) Department of Physics, Tanta University, Egypt
10.1993 – 11.1994	Militarism: Egyption Army
11/1994- 10-1995	-Prepatory courses for M.Sc. degree in physics (Department of Physics, Tanta University, Egypt) -Assistant lecturer in Department of Physics, Faculty of Education, Tanta University, Egypt.
10/1995-12/1998	Obtained Master of Science (M.Sc.) (Department of Physics, Tanta University, Egypt)
09 .2001– 09.2002	-German course; Goethe-institut, Cairo, Egypt; obtained the German language proficiency certificate (ZMP) -Assistant lecturer in Department of Physics Faculty of Education, Tanta University, Egypt
09/2002- 04/2003	Assistant lecturer in Department of Physics Faculty of Education, Tanta University, Egypt.
04/2003-04/2004	Scientific worker in department of Semiconductor Ulm University, Germany
04/2004- present	Scientific worker in Institute of Semiconductor Technology, Technical University Braunschweig, Germany. Ending with PhD (Dr.-Ing).